

VU Research Portal

Putting two and two together

Zandvoort, Coen Sebastiaan

2022

document version

Publisher's PDF, also known as Version of record

[Link to publication in VU Research Portal](#)

citation for published version (APA)

Zandvoort, C. S. (2022). *Putting two and two together: Cortico-synergy analysis for posture and gait*. [PhD-Thesis - Research and graduation internal, Vrije Universiteit Amsterdam].

General rights

Copyright and moral rights for the publications made accessible in the public portal are retained by the authors and/or other copyright owners and it is a condition of accessing publications that users recognise and abide by the legal requirements associated with these rights.

- Users may download and print one copy of any publication from the public portal for the purpose of private study or research.
- You may not further distribute the material or use it for any profit-making activity or commercial gain
- You may freely distribute the URL identifying the publication in the public portal ?

Take down policy

If you believe that this document breaches copyright please contact us providing details, and we will remove access to the work immediately and investigate your claim.

E-mail address:

vuresearchportal.ub@vu.nl

Putting two and two together

Cortico-synergy analysis for posture and gait

Coen S. Zandvoort

This PhD thesis was embedded within and supported by Amsterdam Movement Sciences Research Institute and Institute Brain and Behavior Amsterdam, at the Department of Human Movement Sciences, Vrije Universiteit Amsterdam, The Netherlands. The research was funded by the Netherlands Organisation for Scientific Research (NWO Vidi Grant FirSTeps #016.156.346) and the European Research Council (ERC Starting Grant Learn2Walk #715945).

© Coen Zandvoort, 2022

ISBN: 978-94-6458-530-8

Cover design and layout:

Coen Zandvoort

Sheet music at cover:

Erik Satie – Gnossienne No.1

Printing:

Ridderprint, www.ridderprint.nl

Financial support for printing this thesis was kindly provided by ANT Neuro, Cometa Srl and TMSi.



VRIJE UNIVERSITEIT

**PUTTING TWO AND TWO TOGETHER
CORTICO-SYNERGY ANALYSIS FOR POSTURE AND GAIT**

ACADEMISCH PROEFSCHRIFT

ter verkrijging van de graad Doctor aan
de Vrije Universiteit Amsterdam,
op gezag van de rector magnificus
prof.dr. J.J.G. Geurts,
in het openbaar te verdedigen
ter overstaan van de promotiecommissie
van de Faculteit der Gedrags- en Bewegingswetenschappen
op donderdag 24 november 2022 om 9.45 uur
in een bijeenkomst van de universiteit,
De Boelelaan 1105

door

Coen Sebastiaan Zandvoort

geboren te Amsterdam

promotor: prof.dr. A. Daffertshofer

copromotor: dr. N. Dominici

promotiecommissie: prof.dr. V.G.M. Weerdesteyn
prof.dr.ir. N.M. Maurits
prof.dr. M.J. Brookes
dr. T.W. Boonstra
prof.dr. J.B.J. Smeets

Voor m'n oma's...

TABLE OF CONTENTS

1	Introduction	9
2	The human sensorimotor cortex fosters muscle synergies through cortico-synergy coherence	25
3	Differential sets of cortical muscle synergy signatures during adult locomotion	57
4	Cortical contributions to locomotor primitives in toddlers and adults	69
5	Defining the filter parameters for phase-amplitude coupling from a bispectral point of view	111
6	Epilogue	143
	Bibliography	155
	Summary	169
	Samenvatting	173
	Acknowledgements	177
	List of publications	183

CHAPTER 1

Introduction

The generation and maintenance of locomotion, posture, and balance require the orchestrated activations of a plenitude of (skeletal) muscles. The neural activity that accompanies these activations involves the central nervous system, i.e., the brain from cortex and cerebellum to the brainstem and the spinal cord, as well as the peripheral nervous system. A long-standing aim of motor control research is to identify the mechanisms that underlie the tuning of muscle group activations which let us perform movements with seeming ease. Pinpointing such mechanisms comes with conceptual challenges. An arguably naive idea is that the nervous system directly recruits and controls individual motor units. Their sheer number, however, will make this a combinatorial contest that is hard to settle, even for the tremendous computation power of a human brain. One must realise that our musculoskeletal system contains a plethora of redundant degrees of freedom: The same behavioural goal might be achieved by a variety of muscle combinations (Bernstein, 1967), rendering individual motor unit control ambiguous. It seems more likely that our nervous system ‘simplifies’ motor control by steering multiple muscles in unison. Controlling groups of muscles rather than individual motor units yields a tremendous reduction of the degrees of freedom and thus allows for efficient motor control (Giszter et al., 1993; Grillner, 2011; Sherrington, 1952; Tresch et al., 1999).

The idea of controlling multiple muscles in unison is not new. In the 19th century, propriospinal reflexes were considered essential for the generation of muscular activation patterns. Already then several neurophysiological experiments revealed that mammals can generate alternating and/or cyclic flexor-extensor movements even when their spinal cord is transected, i.e., in the absence of descending input from brain and brainstem (Freusberg, 1874; Goltz, 1869). Put differently, muscle activations can be performed via mere propriospinal circuitries. It was also shown that spinal reflexes can establish cyclic and sequential performances, and are even specific for distinct parts of a cycle like stance and swing phases in walking (Freusberg, 1874).

In the early 20th century, the view of “spinal reflexes” received further experimental support. In a set of experiments Thomas Brown (Brown, 1911, 1914) cut the sensory nerve roots close to the proximity of the spinal cord and showed that spinal guinea pigs and cats can generate rhythmic locomotor movements without supra-spinal and sensory influences. He concluded that the spinal cord must contain an “autonomous factor” that is able to operate without supra-spinal and sensory input. Interestingly, Brown’s findings disagreed with those



of his mentor, Charles Sherrington. In 1910, Sherrington suggested that locomotor behaviour may only be maintained in the presence of sensory feedback, especially the proprioceptive reflex. Brown's conceptual advance appears very similar to what Wilson & Wyman (1965) later coined central pattern generators (CPGs).

In the second half of last century, a large body of research examined the existence and functioning of motor CPGs in vertebrates and invertebrates. The (by now) traditional CPG model considers two separated half centres that reciprocally produce flexor and extensor movements of a limb (Jankowska et al., 1967a, 1967b). In the 1970s and 1980s, Sten Grillner took this concept several steps further in a set of seminal experiments that shed light on the neural architecture of the spinal networks in cats, lampreys, and dogfishes (Grillner, 1974, 1985). His study on decerebrated cats showed their capacity to generate well-coordinated locomotor patterns (Grillner & Zangger, 1979). While earlier ideas were mainly based on behavioural observations – e.g., the cinematographic recordings (Brown, 1914) – this time neuromuscular patterns were registered using electromyography (EMG) (Grillner & Zangger, 1979). EMG may be considered as a proxy of α -motoneuron activity at the spinal level.

Nowadays, it is generally accepted that mammal CPGs govern rhythmic movement activity at the spinal cord (Grillner, 2006; Guertin, 2009). This includes extensions of the two separated half centres CPGs to multi-layered versions that incorporate sensory pathways and multiple spinal layers comprising premotor interneurons and α -motoneurons (McCrea & Rybak, 2008). Pinpointing this in primates remains challenging but conceptual, technological and methodological advances such as computational modelling or via genetic, behavioural, neuropharmacological, neuroanatomical and electrophysiological studies do allow for addressing CPGs even in humans (d'Avella et al., 2003; Dominici et al., 2011; Hart & Giszter, 2010; Kutch & Valero-Cuevas, 2012; Lemay & Grill, 2004; Mussa-Ivaldi et al., 1994; Pinto & Golubitsky, 2006; Saltiel et al., 2001). While most of the findings in invertebrate and lower vertebrate studies suggest that the motor cortex does not have to be involved in the generation and maintenance of locomotion, posture, and balance, this is different in humans (Capaday, 2002; Nielsen, 2003). In fact, the motor cortex appears to be an essential neural structure in humans (Yang & Gorassini, 2006). In the absence of an adequate neural interplay between cortical motor networks, other supra-spinal areas and the spinal cord most, if not all, motor tasks will not be completed appropriately; spinal cord

injury patients clearly demonstrate this (Wagner et al., 2018). Even with spinal cord stimulations, muscular covariances in spinal cord injury patients differ from those in healthy controls (Cheng et al., 2019).

Humans accomplish cyclic movements by integrating supra-spinal structures including the motor cortex (Grillner & El Manira, 2020; Kiehn, 2006). In line with Bernstein's (1967) ideas, the motor cortex is unlikely to have a one-to-one projection to spinal motoneurons and muscles (Cheney & Fetz, 1985; Graziano, 2006). The reduction of redundancy calls for 'clever' solutions. One may speculate that the motor cortex itself utilises modular principles similar to spinal circuitries (Overduin et al., 2015; Overduin et al., 2012). However, the motor control related organisation of the motor cortex is still not fully understood. State of the art is to study neural 'coupling' at the two sides of the cortico-spinal tract by comparing signals recorded from the cortex and from the muscle(s). Most of the studies build on covariance analysis and address either ongoing and/or voluntary activity or responses to peripheral and/or transcranial stimulation (Petersen et al., 2001; Petersen et al., 2012; Roeder et al., 2018). In particular, coherence, as the frequency-based counterpart of correlation, has provided many insights into the functioning of cortico-muscular pathways (Conway et al., 1995). However, the vast majority of experimental paradigms have been limited to (1) single muscle assessments and (2) voluntary dexterous tasks (van Wijk et al., 2012b). With my thesis, I sought to shed light on the potentially modular organisation of the motor cortex and spinal cord in more complicated motor tasks. There, cortico-spinal connectivity assessments must be extended to the multivariate domain (Pirondini et al., 2017; Reyes et al., 2017; Yokoyama et al., 2019). As I will show in the chapters to come this, and other extensions, enabled me to examine cortical contributions to multiple muscles, eventually specifying the coupling between the motor cortex and muscle synergies.

The neurophysiology of the electro-encephalography and electromyography

Electro-encephalography (EEG) and EMG allow for recording neurophysiological activity in the cerebral cortex and in motoneuron pools, respectively (Figure 1.1).

Signals recorded by EEG primarily reflect electric potentials of populations of post-synaptic neurons in superficial layers of the cortex. Neurons communicate with each other by transmitting action potentials through synapses. When an action potential of a pre-



synaptic neuron arrives at the synapse that is connected to a post-synaptic neuron, neurotransmitters are released towards the latter. If sufficient action potentials arrive within a finite time span, an action potential may be elicited at the post-synaptic neuron. Action potentials themselves are biphasic, and they are present only for a fairly short period that does not exceed more than a few milliseconds, rendering them difficult to record from a distance. However, neurotransmitters at the cell membrane of the post-synaptic neuron cause monophasic current flows that change the potential of the post-synaptic neuron's soma over a relatively long time (Hodgkin, 1951). If these post-synaptic potentials add up over many populations, EEG can pick up their sum (Baillet et al., 2001). As said, EEG is sensitive to electric potential changes in superficial layers. This is not only because the corresponding neurons are the closest to the EEG electrodes. Layers IV and V contain long dendritic trees and especially those of pyramidal cells are spatially aligned towards the surface of the cortex. That is, EEG is particularly sensitive to neural activity of populations of pyramidal cells in cortical gyri (Figure 1.1).

The brain activity measured with EEG is characterised by oscillatory components. They are the result of recurrent discharges of neuronal populations (Pfurtscheller & Da Silva, 1999). Brain rhythms are considered functionally relevant because they may facilitate neural communication. Both frequency and spatial origin/extent of the rhythms are function specific (Fell & Axmacher, 2011; Fries, 2005). Throughout this thesis, I focused on beta- (13-30 Hz) and Piper-rhythms (~40 Hz). Oscillations at these frequencies are known to be prevalent in the motor system and are associated with stable motor outflow and multi-sensory binding, respectively (Fries, 2005; van Wijk et al., 2012b). Phase locking between cortico-muscular beta oscillations generally emerges during steady-state force tasks (e.g., pinch-grip) that require a weak muscle contraction (Van Wijk et al., 2012a). The beta rhythm disappears when either the movement is initiated or the muscular contraction becomes stronger and phase locking between oscillations appears at higher frequencies instead, such as the Piper band (Brown et al., 1998).

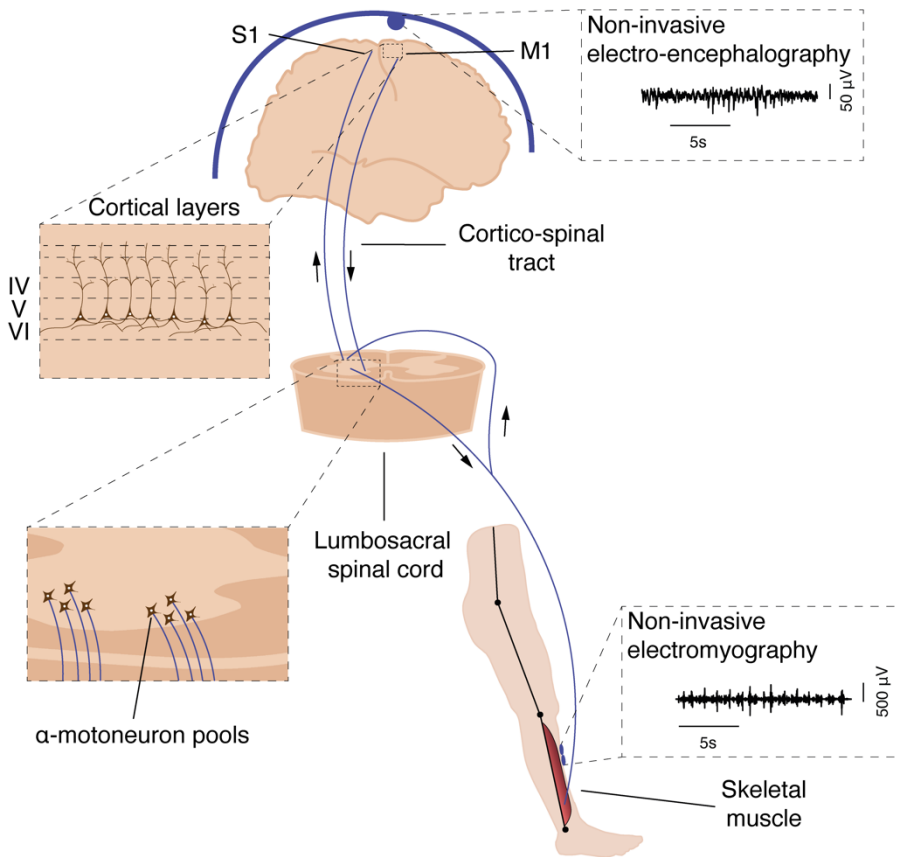


Figure 1.1 – Neurophysiological principles of non-invasive electro-encephalographic (EEG) and electromyographic (EMG) recordings. The primary motor cortex (M1) projects down to the (lumbosacral) spinal cord along the internal capsule, medulla and cortico-spinal tract (the first two structures are not depicted). Population of pyramidal cells are spatially aligned in cortical layers IV and V. Activity generated by neural ensembles within these layers is mostly picked up outside the scalp during EEG recordings. In the spinal cord, populations of α -motoneurons project to skeletal muscles. Action potentials arrive at the skeletal muscle and spread to the cutaneous EMG electrodes. Sensory pathways project back to the dorsal part of the spinal cord and primary sensory cortex (S1).

In the studies summarised in this thesis, I employed surface EMG extensively. In a nutshell, a muscle is innervated by hundreds of α -motoneurons that are located at the ventral horn of the spinal cord (Figure 1.1). Their axons project and transport the action potentials from the spinal cord to neuromuscular junctions. These action potentials yield muscle fibre contractions resulting in muscular force. Like EEG, surface EMG is also recorded from a distance, i.e., on the skin. Hence, it picks up the electric potential changes of many motor units that are active simultaneously.



Analysis techniques

EEG and EMG recordings form a solid base to estimate links between the motor cortex and muscle synergies. In my thesis, I quantified these links by combining two well-established approaches: muscle synergy and cortico-muscular coherence analyses. I will briefly outline both of them in the following paragraphs.

Muscle synergies. Thus far, I introduced spinal modularity in terms of CPGs that are classically considered as small-scale neural circuitries. Alternatively, one may approach spinal modularity from the perspective of the end-effectors, whereby the (co-)activated muscles are grouped into (functionally relevant) muscle synergies. Before continuing with the latter, I would like to add a statement of warning: while CPGs and muscle synergies share conceptual similarities and are potentially complementary, the concepts and terms should not be used interchangeably (Bizzi et al., 2008; Grillner, 1985). One reason for this is that CPGs are usually referred to as units that can function without external input (Rybak et al., 2006), whereas muscle synergies do rely on supra-spinal and sensory input.

Muscle synergies describe low-dimensional entities that are accommodated in the spinal cord (Bizzi & Cheung, 2013; d'Avella et al., 2003). A muscle synergy is typically viewed as a spatial module that specifies a group of simultaneously active muscles that display a common temporal activation pattern. Once muscle synergies are recruited, they orchestrate the activity of muscle groups through the corresponding α -motoneurons. In monkeys, the linear combination of muscle synergies has been shown to be an adequate model of the generative capacity of the premotor inter-neuronal populations (Takei et al., 2017; Takei & Seki, 2010). In turn, when using EMG, linear decompositions via statistical analyses may serve to disentangle muscle synergies. In my studies, I mostly used the low-frequency envelopes (<10 Hz) of several EMG profiles and combined them in a multivariate signal. This signal was decomposed into a few sets of weights, each representing a synergy and specifying the strengths with which the individual muscles participate in the synergy, together with the corresponding temporal activation patterns (Figure 1.2). I accomplished this via non-negative matrix factorization (NNMF) to estimate the muscle synergies (Lee & Seung, 1999), which is formally defined as:

$$EMG(t) = \sum_{s=1}^N P_s(t) \cdot W_s + \epsilon \approx \sum_{s=1}^N P_s(t) \cdot W_s \quad (1.1)$$

with EMG (dimensions: time \times muscles) being the multivariate set of EMG envelopes and P_s (time \times synergies) and W_s (synergies \times muscles) the temporal activation and the set weights of synergy s , respectively, and an residual error, ϵ (Cheung & Tresch, 2006). This linear decomposition $EMG \mapsto P_s W_s$ includes the constraint that both P_s and W_s are positive semi-definite, and P_s and W_s have rank S . Conventional NMF approaches solve the minimisation of the Frobenius norm $\|EMG - P_s W_s\|_F$.

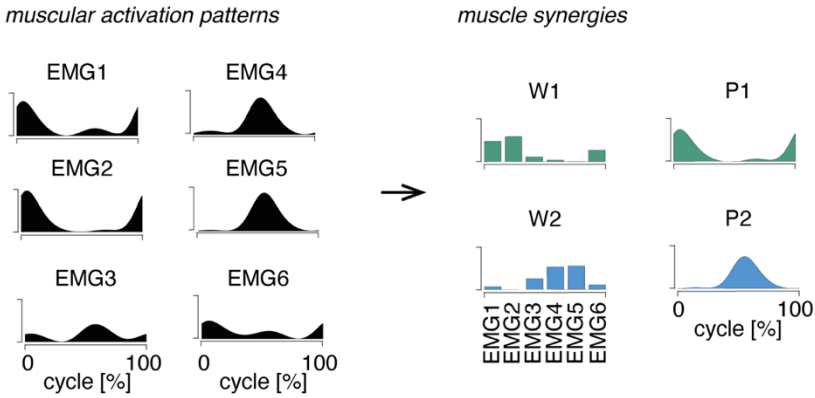


Figure 1.2 – Overview of the muscle synergy computation from the muscular activation patterns. Muscular activation patterns of muscles EMG1-EMG6 (black waveforms) represent envelope EMGs as a function of the gait cycle. Through multivariate analysis techniques, here represented by the horizontal arrow, the patterns of EMG1-EMG6 are decomposed into muscle weights ($W1$ - $W2$) and basic activation patterns ($P1$ - $P2$).

Over the last two decades, muscle synergy analysis has been widely employed to assess spinal modularity during various motor control tasks (d'Avella et al., 2003; Dominici et al., 2011; Ivanenko et al., 2004; Kutch & Valero-Cuevas, 2012; Overduin et al., 2015; Saltiel et al., 2001; Sylos-Labini et al., 2020; Takei et al., 2017). These and many other studies allowed for inferences of spinal cord functioning based on relatively ‘simple’ experimental assessments, namely conventional albeit multivariate EMG. One has to keep in mind, though, that both conceptual (e.g., synergy’s existence, encodement, activation, organisation) and computational (linearity, factorisation methods, error distribution, and other model assumptions) aspects of this analysis are still under debate (Cheung & Seki, 2021).

Important for my thesis is that muscle synergy analysis alone falls short in pinpointing the neural origin of synergy formation. This is certainly true when allowing the cortex with (all) its brain rhythms to participate in this formation. In my thesis, I focused on the beta- and Piper-rhythm for which I had to ensure that the estimated synergy activation patterns cover these frequency ranges rather than being limited to low-frequency envelope dynamics. For this, I estimated synergies via the traditional envelope approach and used the resulting weights together with the original EMG signals (including their high-frequency components) to define “virtual activation patterns”.

Cortico-muscular coupling by means of coherence. As indicated above, I employed coherence as a functional connectivity measure between EEG and EMG (Figure 1.3A-B). Coherence is a measure of phase locking as a function of frequency. Put differently, it quantifies the consistency of the relative phase between two time series. It yields values between 0 and 1, where 1 implies a perfect linear association. More formally, it reads

$$C_{xy}(\omega) = \frac{|\langle |S_x(\omega)S_y(\omega)|e^{i(\phi_x(\omega)-\phi_y(\omega))} \rangle|^2}{\langle |S_x(\omega)|^2 \rangle \langle |S_y(\omega)|^2 \rangle} \quad (1.2)$$

where C_{xy} denotes the magnitude-squared coherence between signal x and y , S_x and S_y are the Fourier transforms at frequency ω , ϕ_x and ϕ_y are the corresponding Fourier phases, and $\langle \cdot \rangle$ represents the expectation value which can be estimated over consecutive recordings, trials and/or epochs. If one randomises the phases of one of the signals, coherence disappears, even though the power is identical to the non-randomised version (Figure 1.3B-C).

Coherence analysis can facilitate inferences on the fast-pyramidal monosynaptic pathways from the motor cortex to the spinal cord (Ibanez et al., 2021). Yet, this phase-locking estimate does not encompass all neural interactions in the central nervous system as it subsumes that both signals/activities are compared for their phases at a single frequency ω , while locking between phases at different frequencies remains opaque. As a matter of fact, many recent studies indicated the relevance of cross-frequency coupling (Aru et al., 2015; Canolty et al., 2006; Jensen & Colgin, 2007). Therefore, I also devoted a study to

advance the method of coherence to quantify cross-frequency interactions. The so-called bicoherence allows for the estimation of the relationships between the 20- and 40-Hz frequencies of the beta- and Piper-rhythms. I will return to this prospective application in the Epilogue of my thesis.

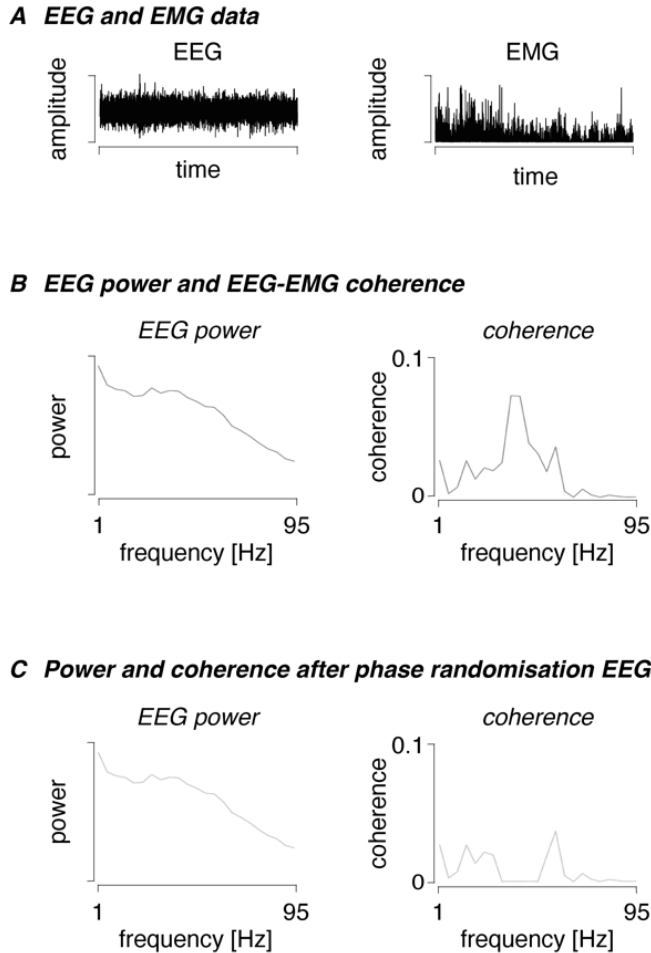


Figure 1.3 – Overview of coherence estimation. (A) Time series of example EEG and EMG data. Both time series were transformed to the frequency domain using fast Fourier transforms and a windowed segmentation approach. (B) Coherence can be computed after estimating the cross and power spectra. The coherence spectrum between the EEG and EMG data reveals a clear 40-Hz component. (C) This coherence at 40 Hz disappears after randomising the phases of the EEG signal between 30 and 50 Hz, showing that coherence captures the consistency of the relative phase. EEG power is unaffected by this phase randomisation.

Inverse and forward modelling. Since EEG measures brain activity outside the scalp, it suffers from the inverse problem (Figure 1.4A): one cannot assign a unique set of sources in the volume given a recording at the surface. Source reconstruction methods are meant to provide approximate solutions for this, first and foremost by imposing biophysical constraints combined with statistical ‘constraints’ and subsequent hypothesis testing.

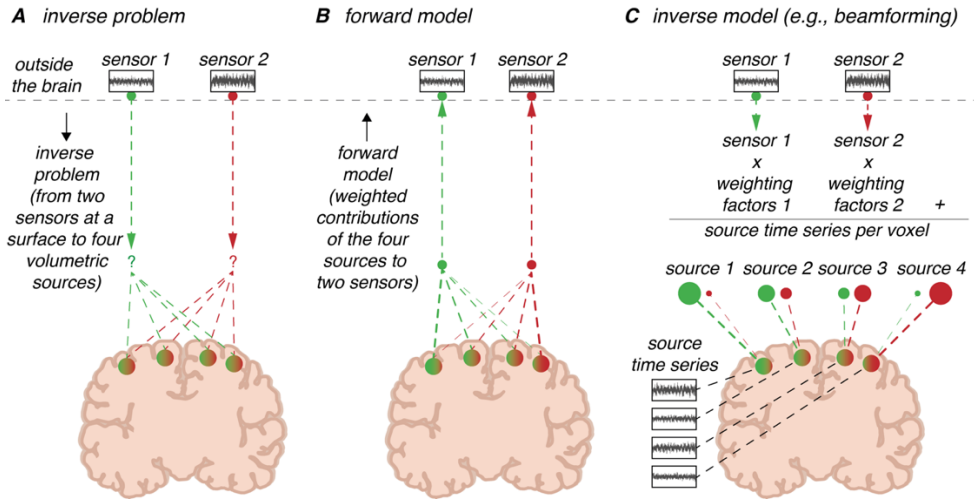


Figure 1.4 – Brain researchers conducting non-invasive electrophysiological recordings face the inverse problem (i.e., measuring EEG signals outside the scalp without knowing the origin in the brain). (A) In this illustrative example, the activity is measured outside the scalp by means of two sensors. This surface-based neural activity can originate from the four sources within the brain without knowing if and how each of these sources contributes to the two sensors. (B) To solve this, one must estimate a forward model, describing how potential neural activity at one of the sources spreads to the sensors. By applying this forward model, one can find a solution to the inverse problem and pinpoint the neural origin of the sensor-level activity. This solution is unique; however, one has to make several assumptions on biophysical and geometrical properties. (C) This is achieved by multiplying the sensor-level time series with a set of spatial weights using the inverse of the forward model. After a statistically significant source has been identified, source-level time series can be reconstructed.

The starting point for this is a forward model (cf. Figure 1.4B) which – given the recording from a distance – can be simplified by defining a lead field, i.e., a linear mapping from possible neural sources to the recording points. The spatial extent of the corresponding lead-field matrix is given by anatomical constraints and its entries by biophysical properties like tissue conductivity (Vorwerk et al., 2018). Defining the lead field can be laborious but is greatly facilitated by open-source software toolboxes like SPM, FieldTrip, FreeSurfer, FSL, etc.). In my thesis, I segmented structural MRIs into five tissue types, namely, the skin (scalp) and bone (skull) as well as grey and white matter and the cerebrospinal fluid

(Vorwerk et al., 2014) via finite element modelling. The entries of the lead field were defined accordingly and subsequently inverted by means of Penrose’s pseudo-inverse (the rank of the lead-field matrix is bounded by the number of EEG electrodes whilst its dimension may be as high as the number of voxels in the brain volume of the structural MRI).

There are two statistical ‘constraints’ to consider. First, I used Dynamic Imaging of Coherent Sources (DICS) beamforming (Gross et al., 2001) to define what is often referred to as spatial filters (Figure 1.4C). Formally, these spatial filter weights W can be computed as follows:

$$W(r, \omega) = (L^T(r)C(\omega)^{-1}L(r))^{-1}L^T(r)C(\omega)^{-1} \quad (1.3)$$

with $C(\omega)$ being the cross-spectral density matrix at frequency ω , which has dimensions equal to the number of EEG channels. $L(r)$ denotes the lead-field matrix at location r in three dimensions. This vector notation can be changed to a scalar case by finding the largest singular value. DICS beamforming then is a mere singular value decomposition assuming every possible source at locations of the lead field to comprise a unit dipole. It is expressed in the frequency domain, which renders it particularly efficient when concentrating on distinct frequency bands (in my case the beta- and Piper-rhythms). The resulting singular values provide an estimate of the power or likelihood of every possible source location to contribute to the observed EEG. When combined with the aforementioned lead-field matrix inversion, one can estimate the activity at the source. With my focus on cortico-synergy coherence, I optimised the coherence between the EEG and the “virtual activation patterns” of the muscle synergies via the DICS approach. Second, the power/likelihood of a source can be further pinpointed by estimating its statistical significance using contrasts between groups, conditions, or time windows of performance as outlined below.

Hypothesis testing. The statistical assessment of source activities comes with two major challenges. (1) Activity distributions can – in general – not be assumed to be Gaussian and (2) the number of potential sources is large causing a multiple comparison problem. I therefore employed cluster-based permutation testing (Maris & Oostenveld, 2007). In brief,

one first clusters the sources via the covariance using a Monte-Carlo approach (i.e., via random drawing given the large number of voxels encountered) and then estimates a bootstrap distribution of the activities where surrogates are built via random permutations of the clusters.

Employing permutation tests is particularly useful when seeking for statistical effects between several conditions (e.g., a contrast of baseline and active conditions). Example data of two conditions are given in Figure 1.5A-C. There, the null hypothesis that both datasets are drawn from the same probability distribution can be falsified via a certain test statistic (e.g., t - or F -values, Figure 1.5D). As said, data are subjected to random clustering or partitioning, which assigns all data samples (subjects or conditions) to one of the available conditions at random. The test statistic is computed from these shuffled data yielding a permutation distribution (a special form of a bootstrap distribution). After sufficiently many partitions, statistical inferences can be made based on whether p -values surpass a given significance threshold. This threshold is defined based on clusters (Figure 1.5E-F).

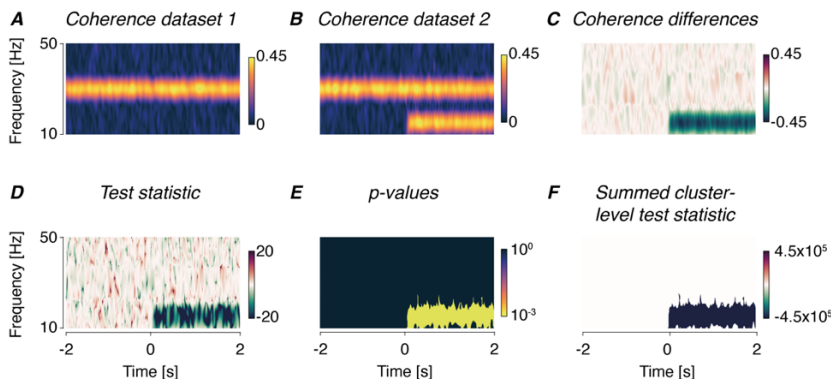


Figure 1.5 – An illustrative example of cluster-based permutation testing. (A-C) Two datasets exhibiting coherence are simulated. Both datasets show significant coherence around 30 Hz and dataset 2 also contains coherence at 15 Hz in the time window of 0-2 seconds. This also appears in the coherence differences. (D-F) Cluster-based permutation testing using an independent t -test reveals negative t -values at this window. These data samples get clustered into one negative cluster, which turns out to be significant. The summed test statistic of this negative cluster exceeds the critical cluster threshold as determined from the permutation distribution that corresponds to the predefined α -level of 0.025. This allows us to reject the null hypothesis that coherence datasets 1 and 2 are drawn from the same probability distribution.

Research questions

It should now be clear that deciphering the neural basis of fundamental spinal patterns and muscle synergies is not trivial. I tackled this by correlating (estimated) activities in the cortex with (estimated) activities of synergies. My overarching research question was:

How does the motor cortex interact with muscle synergies?

This question appears quite broad. Hence, I used a set of distinct motor control experiments to provide an answer to it that is not limited to a single paradigm. That is, I used a variety of electrophysiological data obtained in different experiments to investigate the functional connectivity along cortico-synergy pathways in different motor tasks. All of the settings came with their own, more specific, research questions:

- Q1. How does the motor cortex contribute to muscle synergies during the generation and maintenance of locomotion, posture, and balance?*
- Q2. How do the locomotor muscle synergies and their interaction with the motor cortex develop? Specifically, does the interaction differ between toddlers and adults?*
- Q3. How can we assess the functional connectivity across different frequencies?*

Outline of the thesis

In the study summarised in **Chapter 2**, I introduced an analysis method coined cortico-synergy coherence. As will be shown, this method allowed for estimating long-distance phase synchronisation between cortical oscillations and lumbosacral activity that contributes to balance control in a unipedal stance task. I recorded EEG and EMG in healthy adults to answer *Q1*, for which I expected that the cortical oscillations at the movement-related beta- and Piper-bands are manifest in the virtual activation patterns of the muscle synergies.

Building on the capacity of cortico-synergy coherence to identify phase-locked patterns between cortical areas and muscle synergies, I investigated the coupling between



the motor cortex and muscle synergies during locomotion. This study is summarised in **Chapter 3** and provides an answer to *Q1*. Walking is ‘more dynamic’ than quiet stance, which is reflected in the temporal amplitude modulations of both muscular and synergy patterns throughout the gait cycle. I hence expected cortico-synergy coupling to only occur at specific phases during the gait cycle. Being specific for the type of cycle phase and cortical representation of the concomitant synergy this study provided new insights into the location and timing of balance and gait control alike.

The study underlying Chapter 3 revealed two synergies that exhibit significant coherence. They appeared similar to those that emerge in the course of walking development. For the report in **Chapter 4**, I dug deeper into this resemblance via a cross-sectional study involving independently walking toddlers and adults. Together with the findings of Chapter 3 this study served to answer *Q2*.

For **Chapter 5**, I went beyond the linear cross-spectrum and examined the relationship between univariate bicoherence (i.e., coherence between three frequencies) and coherence-based phase-amplitude coupling; see *Q3*. The latter defines the coupling between the phase at low frequencies and amplitude at higher ones. While the corresponding study should primarily be seen as a methodological advance, it comes with great potentials in specifying the interaction between gait and balance control that seemingly relies on distinct frequency components, oscillatory activity in the beta-frequency band (~20 Hz) vis-à-vis the Piper rhythm (~40 Hz).

In **Chapter 6**, I reflect on all the findings and how they answer my specific and overarching research questions. I also outline the future questions that should be addressed to better understand the interaction between cortical areas and muscle synergies. I present preliminary results on a longitudinal study into the early cortical development of the muscle synergies addressing the emergence of the two synergies and their cortical representations highlighted in Chapters 3 and 4. I also follow up on Chapter 5 by illustrating how bicoherence can be integrated into the study of cortico-synergy coherence.



The human sensorimotor cortex fosters muscle synergies through cortico-synergy coherence

In neuromotor control, the dimensionality of complex muscular activation patterns is effectively reduced through the emergence of muscle synergies. Muscle synergies are tailored to task-specific biomechanical needs. Traditionally, they are considered as low-dimensional neural output of the spinal cord and as such their coherent cortico-muscular pathways have remained underexplored in humans. We investigated whether muscle synergies have a higher-order origin, especially, whether they are manifest in the cortical motor network. We focused on cortical muscle synergy representations involved in balance control and examined changes in cortico-synergy coherence accompanying short-term balance training. We acquired electromyography and electro-encephalography and reconstructed cortical source activity using adaptive spatial filters. The latter were based on three muscle synergies decomposed from the activity of nine unilateral leg muscles using non-negative matrix factorization. The corresponding cortico-synergy coherence displayed phase-locked activity at the Piper rhythm, i.e., cortico-spinal synchronisation around 40 Hz. Our study revealed the presence of muscle synergies in the motor cortex, in particular, in the paracentral lobule, known for the representation of lower extremities. We conclude that neural oscillations synchronise between the motor cortex and spinal motor neuron pools signifying muscle synergies. The corresponding cortico-synergy coherence around the Piper rhythm decreases with training-induced balance improvement.

Adapted from: C.S. Zandvoort, J.H. van Dieën, N. Dominici, & A. Daffertshofer (2019). *The human sensorimotor cortex fosters muscle synergies through cortico-synergy coherence*. Neuroimage, **199**, 30-37. [10.1016/j.neuroimage.2019.05.041](https://doi.org/10.1016/j.neuroimage.2019.05.041)

Introduction

Human motor control comes with daunting challenges as even seemingly simple movements require well-timed orchestration of a plenitude of muscles. The motor system has abundant degrees of freedom (Bernstein, 1967). It is commonly accepted that controlling them involves task-specific combinations of muscle activity, which are coined muscle synergies (d'Avella et al., 2003; Dominici et al., 2011). Synergies sometimes manifest in small-scale neural circuitries in the spinal cord (Lemay & Grill, 2004; Saltiel et al., 2001), although, in general, their underlying neural mechanisms remain unclear (Tresch & Jarc, 2009). While there are some recent conjectures about muscle synergy representations in the motor cortex (Aumann & Prut, 2015; Bizzi & Cheung, 2013; Pirondini et al., 2017), as of yet a thorough empirical proof of their existence in humans is still lacking. Signatures of cortical muscle synergy representations were shown in the primate brain (Overduin et al., 2015). With the current study, we provide support by focusing on coherence between motor cortex oscillations and muscle synergies at specific frequency bands.

Phase locking of neural populations facilitates information transfer between them and is apparent in the motor system at various levels. Within the motor network intra- and interhemispheric phase locking is especially present in the beta-frequency band (15-30 Hz) (Rueda-Delgado et al., 2014; van Wijk et al., 2012b). Long-distance phase locking is also visible as cortico-muscular coherence (Baker, 2007; Boonstra et al., 2009). Phase locking is believed to reflect entrainment of spinal motoneurons with the cortical motor nuclei (Mima & Hallett, 1999b). Coherent discharges, emerging from the summated activity of pyramidal neural populations at superficial cortical layers, propagate along the cortico-spinal tract (Baker et al., 1999; Witham et al., 2011).

Muscles within a single muscle synergy may receive coherent neural input. From a binding perspective, one may expect that this multi-muscular drive is also reflected in cortico-muscular coherence involving multiple muscles. A multi-muscular binding hypothesis of the cortico-spinal drive has been investigated earlier (de Vries et al., 2016; Reyes et al., 2017), but experimental assessments have been limited to oscillatory behaviour of cortico-spinal projections directed to pairs of muscles. Arguably, supra-spinal regions send common neural input to multiple muscles belonging to a single muscle synergy (Bizzi & Cheung, 2013). In other words, neural pathways project to muscle synergies (Aumann &

Prut, 2015), imposing temporal and spatial features of the muscle synergy represented in the motor cortex on motor outflow.

Cortico-spinal entrainment is typically concentrated in the beta- and lower-gamma-frequency bands. The latter 30-60 Hz band has been labelled the Piper rhythm (Brown, 2000), to which dynamical tasks like locomotion (Petersen et al., 2012) and manual tasks (Mehrkanoon et al., 2014; Omlor et al., 2007) seem instantiated. Its functional role for sensorimotor behaviour remains to be elucidated, but this rhythm seems to serve for correcting prediction errors (Mehrkanoon et al., 2014). One may hypothesise that practising a novel sensorimotor task can modulate neural oscillations along cortico-muscular pathways in the Piper rhythm. Motor practice or training may, hence, involve adaptation of cortico-muscular signalling loops conveying Piper-rhythm oscillations.

We investigated functional cortico-synergy connectivity and its plasticity in short-term postural training. We expected Piper-rhythm coherence between motor cortex and muscle synergies to be modulated as a function of practice, reflecting its band- and synergy-specific role in motor control.

Methods

Participants and experimental paradigm

Fifteen healthy young adults (11 males and 4 females; mean \pm SD, age: 24.7 \pm 3.1 years; weight: 71.1 \pm 11.2 kg; height: 179.5 \pm 9.5 cm) were recruited by word of mouth. Participants were included when between 18 and 35 years old and right legged. Exclusion criteria were: (I) injuries in the previous 6 months, (II) self-reported pain or discomfort or any range of motion limitation during activities of daily living and exercises, (III) a self-reported history of neurological disorders, or (IV) a history of participation in postural practising sports (e.g., ballet, yoga, or gymnastics). Participants signed an informed consent prior to performing the experiment. The experimental design was approved by the ethical committee of the Faculty of Behavioural and Movement Sciences of the Vrije Universiteit Amsterdam (#VCWE-2016-200). The experiment was conducted in accordance with the Declaration of Helsinki for experiments on humans.



The study was longitudinal including intra-individual pre-post comparisons between two timepoints (Figure 2.1). A single experiment consisted of a total of 20 trials: 10 pre- and 10 post- postural training. Participants stood unipedally on their preferred right leg at the centre of a robotic-controlled balance board, which imposed rotational mechanical perturbations. Pre- and post-timepoints were interspersed by a postural training session, in which participants practised their unipedal postural control on unstable boards for 30 minutes.

Participants were instructed to react adequately to the rotational mechanical perturbations by stabilising their centre-of-mass to the pre-perturbation equilibrium. Arms were placed along the body; however, participants were allowed to use them if needed to maintain balance. Participants did not wear shoes. A trial was considered as invalid when the participant stepped off the foot plate of the balance board or grabbed one of the handrails next to them to prevent falling. To minimise EEG artefacts, they were asked to fixate their gaze at a white cross of 10x10 cm at eye level on a wall at five meters.

Rotational mechanical perturbations were imposed and controlled externally on the axis of the footplate using a HapticMaster (MOOG-FCS B.V., Nieuw-Vennep, The Netherlands). We used position-controlled perturbations to manipulate the axis beneath the robot-controlled board. The axis had one degree of freedom and only allowed rotation in the frontal plane. Perturbations had a sinusoidal time course of either $+3^\circ$ or -3° and were imposed at a rate of ± 0.8 Hz, equalling an averaged angular velocity of $+6^\circ/\text{s}$ or $-6^\circ/\text{s}$. A single trial contained 30-40 mechanical perturbations, over a trial duration of 40-55s. Consecutive perturbations yielded an inter-perturbation duration variability of 0-250ms. Participants had a break of 60s between consecutive trials to prevent fatigue. Prior to the first trial, participants performed one familiarisation trial on the balance board.

In the postural training, participants practised unipedal balancing on two so-called wobble boards. These boards varied in height to ensure that the postural task became more challenging. While practising on different boards is recommended, standardisation of the intensity, duration, and volume of the postural training programs is currently lacking except for general guidelines (Lesinski et al., 2015). Conform these guidelines, participants performed five unipedal trials of 30s with 30s rest between trials on every wobble board. Between the two boards, participants got a rest of 5 minutes to avoid fatigue.

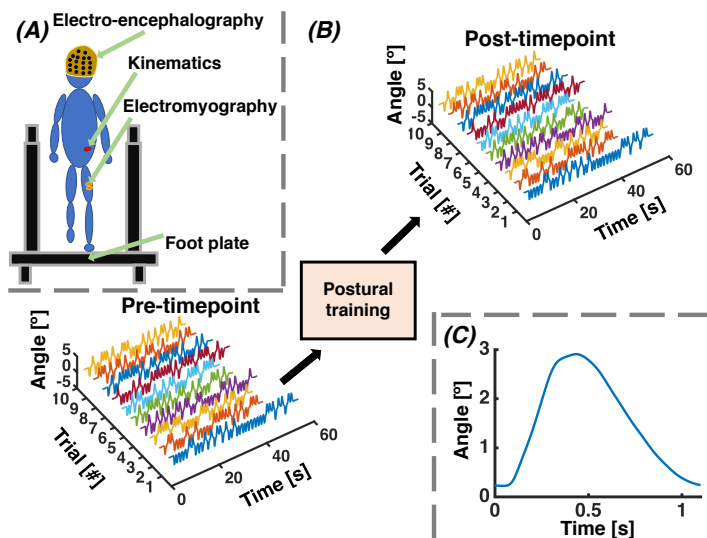


Figure 2.1 – Schematic representation of the experimental setup and paradigm. (A) Schematic experimental setup from the posterior view. Participants stood on their right leg on the foot plate of the robotic-controlled platform which imposed rotational mechanical perturbations. (B) Both ‘Pre-timepoint’ and ‘Post-timepoint’ consisted of ten trials on the platform. Single trials contained a pre-determined number of mechanical perturbations ranging between 30-40. A total of 330 perturbations was imposed at both timepoints. ‘Pre-timepoint’ and ‘Post-timepoint’ plots show board angle modulation as a function of time and trial number. Coloured graphs in these representations indicate different trials. The two timepoints were intermitted by a postural training session. Training effects were investigated by comparing the average of ten trials and all participants per timepoint. (C) Grand average rectified time-locked angle of the robotic-controlled balance platform pooled over perturbations, trials, timepoints, and participants. Time 0s indicates the perturbation onset.

Data acquisition

Electro-encephalography (EEG), multivariate electromyography (EMG), and kinematics data were acquired at pre- and post-training timepoints. Sampling of EEG, EMG, and kinematic signals was synchronised.

Participants wore a 64-electrode EEG cap (TMSi, Twente, The Netherlands). The EEG cap was placed according to the international 10-20 standard. Impedance gel (SonoGel, Bad Camberg, Germany) was injected to keep impedances between the skin and electrodes below 10 k Ω . Every channel was recorded and 24-bits analogue-to-digital converted at a rate of 2,048 Hz by a TMSi Refa 128-channel amplifier (TMSi, Twente, The Netherlands).

Ag/AgCl surface electrode pairs (Medicotest, Ambu® Blue Sensor®, type: N-00-S/25) were anatomically placed according to the SENIAM conventions (Hermens et al., 2000). The inter-electrode distance was set at 20 mm. Surface EMG of the right tibialis anterior (TA), peroneus longus (PN), gastrocnemius medialis (GM), soleus (SO), rectus femoris (RF), vastus lateralis (VL), biceps femoris (BF), adductor longus (AL), and gluteus medius (GL) was measured at a rate of 2,048 Hz. EMG was measured using driven-shielded wires, which minimise the potential effects of movements (e.g., cable sways). To reduce the residual effects of cable sways, cables were attached to the skin with adhesive tape. As EEG and EMG were acquired with the same 128-channel amplifier (64-channel EEG and remaining channels EMG), the ground channel of the EEG was used as a reference for the unipolar EMG instead of placing reference electrodes. We used an average common reference of all EEG- and EMG-channels.

Kinematics was assessed via a 3D motion capture system (Optotrak, Northern Digital, Waterloo, ON, Canada). Three-dimensional positional data of four single LED markers were recorded of the hips (posterior superior iliac spine) and shoulders (posterior part acromion) bilaterally. Kinematic data were acquired using one camera at a rate of 150 Hz. Here, these data served to confirm improvements in postural control across the training session.

Data analysis

Pre-processing and artefact removal. All analyses were performed with custom-made functions involving the open-source FieldTrip toolbox for MATLAB (Mathworks Inc., Natick, USA) (Oostenveld et al., 2011). From the average common reference of the EEG and EMG, the EEG was re-referenced to an average common reference and one bipolar EMG time series was derived from two monopolar EMG time series.

EEG and EMG time series were mean centred and band-pass filtered (bidirectional second-order Butterworth filter between 5 and 250 Hz). Line noise and its higher harmonics were removed using a bidirectional second-order Butterworth band stop filter around 50, 100, 150, and 200 Hz using a bandwidth of 0.5 Hz). EEG time series were temporarily re-referenced to channel F7 to detect bad channels. Individual channels were qualified as ‘bad’ in case the channel contained a flat line or an excessive mean or standard deviation in terms

of amplitude. Exclusion based on amplitude yielded that the single-channel variance exceeded 3 times the standard deviation or 10 times the maximum of all channels. On average, 0.7 channels (range: 0-5 channels) were removed per trial. ‘Bad’ EEG channels were spherically interpolated using spline interpolation as a function of the activity and electrode position of the neighbouring channels. After checking bad channels, EEG time series were re-referenced to an average common reference.



Additional artefact detection and removal were performed with independent component analysis (ICA). ICA was applied on the EEG time series using FieldTrip toolbox functions including an extended fastICA-algorithm with online bias adjustment. Single IC-modes were excluded if their median frequency was lower than 1 Hz (i.e., movement artefacts) or higher than 60 Hz (muscular activity), or if the prefrontal channels were topologically dominant (eye movements). Sensor-level EEG was reconstructed after the set of artefact-containing IC-modes was discarded. The number of components removed at pre- and post-timepoint were 12.51 ± 5.34 and 12.46 ± 5.23 (mean \pm SD), respectively. Rectified EMG signals were obtained from the modulus of the Hilbert transform, since rectifying the EMG is believed to provide an accurate representation of the overall oscillatory activity of the motor units (Boonstra & Breakspear, 2012).

Muscle synergies. We extracted muscle synergies using non-negative matrix factorization (NNMF) of the rectified EMG time series of nine stance leg muscles (TA, PN, GM, SO, RF, VL, BF, AL, and GL) (Lee & Seung, 2001). The rectified EMGs of consecutive trials and participants were concatenated and normalised to the standard deviation of individual muscles. We note that the rectified EMG was not low-pass filtered. Consequently, the resulting temporal activation patterns contained higher spectral content. These high-frequency temporal activation patterns served as input for the subsequent cortico-synergy coherence estimates. However, we do provide results on muscle synergies using more conventional low-pass filtered EMG as *Supplementary material Chapter 2*. In brief, findings based on low-pass filtered EMG as NNMF-input corroborated the findings obtained with the non-filtered EMG (Figures S2.3-S2.6).

A set of 1-9 muscle synergies was iteratively extracted with NNMF. NNMF was constrained to have 50 replicates with 1,000 iterations each and a termination tolerance of

10^{-6} and 10^{-4} for the change in temporal activation patterns and muscle weightings size and residual size, respectively. A-priori criteria to determine the number of required muscle synergies were based on the reconstruction accuracy (RA) of the low-pass filtered EMG. RA was assessed by the quotient of the Frobenius norm of the error and the Frobenius norm of the rectified EMG, where the error was defined as the difference between the rectified EMG and the product of the muscle weightings and temporal activation patterns. Overall and muscle-specific RA were required to surpass a threshold of 90% (Clark et al., 2009). These criteria led to the extraction of three synergies (Figures S2.3 & S2.10). Iterative computation of three muscle synergies results in temporal activation patterns that are close to identical (correlation coefficient: 0.996 ± 0.006).

Cortical source localisation and reconstruction. Cortical source localisation and reconstruction of the muscle synergies were conducted using inverse modelling on the z-transformed sensor-level EEG using DICS-beamformers (Gross et al., 2001). DICS-beamformers allow for the anatomically meaningful localisation of cortico-synergy coherence between the sensor-level EEG and muscle synergies by considering the cross-spectral density matrix. We first built a forward model, which was based on a five-layer volume conduction model computed from the magnetic resonance imaging template of the FieldTrip toolbox (Oostenveld et al., 2011) that was segmented and hexahedrally meshed into binary representations of white matter, grey matter, cerebro-spinal fluid (CSF), skull tissue, and scalp tissue with a default hexahedron shift parameter of 0.3. Finite element modelling using the SIMBIO-software was applied on these geometrical volumes to construct the realistically shaped five-shell volume conduction model (Vorwerk et al., 2018). For the preparation of the volume conduction model, we used the following conductivity values: 0.33 (grey matter), 0.14 (white matter), 1.79 (CSF), 0.01 (skull), and 0.43 (scalp) (Biro et al., 2014). The source model consisted of a 3D-dipole grid with 2 mm^3 resolution, which was geometrically aligned with the brain volume (i.e., CSF, white, and grey matter shell) of the volume conduction model. The source model was shifted 15 mm outwards of the brain tissue. EEG electrode positions were geometrically aligned to the volume conduction model. A lead-field matrix was constructed based on the volume conduction model, source model, and 3D-sensor positions. To prevent power bias to the centre of the head, the lead field was normalised voxel-by-voxel by the overall power. The cross-spectral

density matrix was estimated between the 64 Fourier-transformed EEG and temporal activation patterns using multi-taper Slepian sequences with 1s windows. This matrix was determined in the frequency range of 1-80 Hz with 40.5 Hz as centre frequency and was pooled over consecutive windows within the EEG and EMG signals of every individual trial. To localise coherent cortical sources of the muscle synergies, we averaged coherence between the sensor-level EEG and muscle synergies over frequency and time. Coherence of these cortical sources likely differs from the time-locked cortico-synergy coherence between the source-reconstructed cortical activity and muscle synergies reported as a function of time and frequency.



Common spatial filters were estimated comprising sensor-level data of all timepoints and participants, excluding that cortico-synergy coherence modulation could be assigned to spatial filter variability. Common spatial filters were constrained to being real-valued and the regularisation parameter of the cross-spectral density matrix was set at 5%. Spatial filters were parcellated to the automated anatomical labelling atlas (Tzourio-Mazoyer et al., 2002). Given the results of coherence estimates and their corresponding pre-post training modulation, the left paracentral lobule was selected as region of interest. For this region of interest, source time series were reconstructed by multiplying the spatial filters with the sensor-level EEG. To exclude source-localised cortico-synergy coherence to be the result of a single voxel including excessive coherence, we averaged over a sphere with a 10mm radius. For the left paracentral lobule, the corresponding source time courses were decomposed by singular value decomposition and the most prominent mode served as EEG time series for the cortico-synergy coherence.

Connectivity analysis. EEG and EMG time series containing the 30-40 movement-related potentials were time-locked into epochs from -400 to 600ms relative to perturbation onset. Coherence was estimated between the source-reconstructed activity and temporal activation patterns, establishing cortico-synergy coherence. The temporal activation patterns were the direct output of the NNMF. We applied multi-taper frequency convolutions with Slepian sequences. We note that wavelet transformations yielded comparable cortico-synergy connectivity estimates as the multi-taper frequency convolution (results not shown). Epochs were pooled over perturbations, trials, and participants for both timepoints.

Kinematics. To verify that postural training effects had taken place, the behavioural performance was evaluated by estimating time-to-recovery after the mechanical perturbation. Mediolateral sway of the bilateral hip and shoulder markers was time-locked to mechanical perturbation onset. Principal components were extracted by decomposing the time-locked sway using conventional principal component analysis. To evaluate relaxation time, i.e., anticipatory response after mechanical perturbation onset, we determined the auto-covariance as a function of time lag of the principal component that captured most mediolateral excursion. The first auto-covariance decay around time 0s can be used as a measure of how quick participants responded to the mechanical perturbation. Here, a steeper decay indicates a quicker relaxation to the equilibrium. In line with linear response theory, relaxation times were estimated by fitting a first-order exponential function to this most central exponential decay of the auto-covariance. The time constants of the exponential decay were expected to decrease due to postural training, indicating faster postural recovery after the mechanical perturbation.

Statistical analysis

Cortico-synergy coherence estimates were pooled over perturbations for individual trials, equalling 150 representations per timepoint (10 trials \times 15 participants). Cortico-synergy time-frequency coherence representations were compared using cluster-based permutation tests with a dependent t-test as test statistic and *Timepoint* as factor. We applied cluster-based permutation tests for two reasons: a cluster-based permutation test does not require a-priori assumptions about the probability distribution; these statistical tests are suitable to solve the multiple comparisons problem occurring in the statistical comparison of the voxels of the time-frequency-representations (Maris & Oostenveld, 2007).

The permuted distribution was estimated by partitioning the time-frequency representations into two data sets containing random samples of the original two time-frequency-representations. A test statistic was obtained from the permuted distribution after every partition. These two steps were repeated for 1,000 partitions. The Monte-Carlo distribution of the test statistics was thresholded with a predefined α -level searching for

significant spatial clusters. Probability distributions were thresholded for statistically significant clusters using a cluster α -level of 0.001 and α -level of 0.025 for the t-test.

Results

Muscle synergies

The activity of the nine muscles could be decomposed into three correlative temporal activation patterns. Synergy 1 comprised temporal activation patterns of the gastrocnemius medialis, soleus, and rectus femoris, synergy 2 of the tibialis anterior, peroneus, gastrocnemius medialis, adductor longus, and gluteus medius, and synergy 3 of the vastus lateralis, biceps femoris, adductor longus, and gluteus medius (Figure 2.2A). After the mechanical perturbation, onset at $t = 0$ s, a sequential activation of synergy 2 and synergy 3 occurred (Figure 2.2B). Synergy 2 was of special interest as it comprised most pronounced amplitude modulation following the mechanical perturbation. Synergy 1 was constantly active without considerable amplitude modulation. Sequential activation of synergies 2 and 3 was confirmed by the pairwise cross-covariance, which displayed maxima between the temporal activation patterns of synergy 2 and 3 at 44 and 37ms pre- and post-training, respectively (Figure S2.1). The three muscle synergies covered 87.1 and 87.2% of EMG variation pre- and post-training, respectively (Figure 2.2C). Increasing the number of extracted muscle synergies to 4 did add 4.1 and 4.0% of the EMG variation (Figure 2.2D). The temporal activation patterns, muscle weightings, and EMG variation were similar pre- and post-training. This implies that any modulation of cortico-synergy coherence cannot be assigned to the extraction of non-similar muscle synergies at these timepoints.



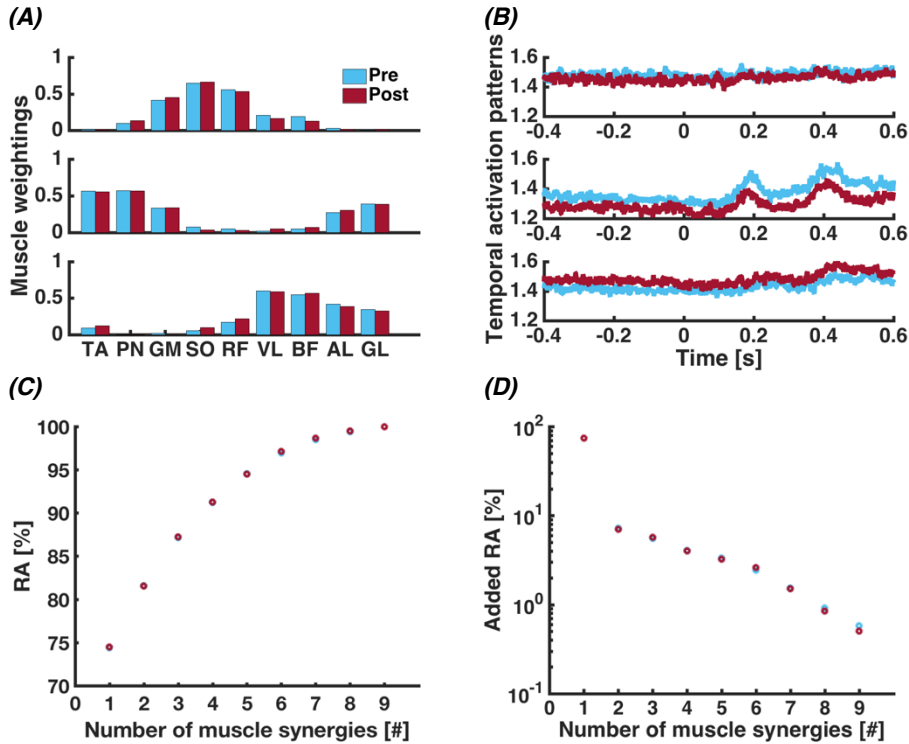


Figure 2.2 – Muscle synergies after non-negative matrix factorization of the electromyographic activity of the nine stance leg muscles. Grand average (A) muscle weighting coefficients, (B) temporal activation patterns, (C) reconstruction accuracy, (D) added reconstruction accuracy. (A) Muscle weighting coefficients of the nine stance leg muscles for three muscle synergies. The nine stance leg muscles were tibialis anterior (TA), peroneus longus (PN), gastrocnemius medialis (GM), soleus (SO), rectus femoris (RF), vastus lateralis (VL), biceps femoris (BF), adductor longus (AL), and gluteus medius (GL). (B) Temporal activation patterns of the three muscle synergies. Time 0s indicates mechanical perturbation onset. The panels depict the mean time-locked activation patterns around perturbation onset. (C) Reconstruction accuracy as a function of number of muscle synergies. RA: reconstruction accuracy. (D) Added reconstruction accuracy by adding a single muscle synergy as a function of number of muscle synergies. RA: reconstruction accuracy.

Cortical source localisation and reconstruction

We selected the left paracentral lobule (left medial Brodmann area 6) as the region of interest for source reconstruction, because overall across timepoints and frequencies it yielded the maximum cortico-synergy coherence. In fact, this maximum coherence was found with synergy 2 (MNI-coordinates [-9.5, -1.5, 78.5] mm) (Figure 2.3). Coherent sources for synergies 1 and 3 were located in right Brodmann area 6 and right Brodmann area 7 (MNI-

coordinates [14.5, -11.5, 68.5] and [22.5, -61.5, 46.5] mm, respectively). Signatures of the Piper rhythm were also found at neighbouring regions at the motor and supplementary motor area, however, their magnitude of the cortico-synergy coherence around this particular frequency band was clearly lower.

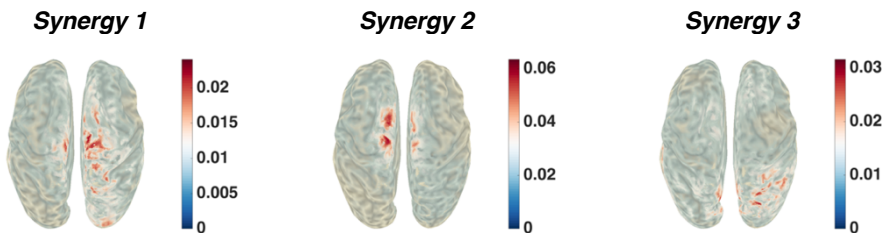


Figure 2.3 – Coherent cortico-spinal sources revealing maximal cortico-synergy coherence. Coherent cortical sources showing maximal cortico-synergy coherence, averaged over frequency (1-80 Hz) and time. Cross-spectral density matrices of the Dynamic Imaging of Coherent Sources beamformers were extended with the temporal activation patterns of the muscle synergies. The cross-spectral density matrix including the temporal activation pattern was estimated over concatenated data of pre- and post-training timepoint for all participants. Hence, the adaptive spatial filters localised sources that showed significant cortico-synergy coherence. Voxels were masked by only highlighting voxels containing the highest 95% cortico-synergy coherence.

Cortico-synergy connectivity

Connectivity estimates revealed significant coherence between the source-reconstructed activity in the left paracentral lobule and temporal activation patterns in the beta-frequency band and around the Piper rhythm (Figure 2.4A-B). All three synergies reflected significant Piper rhythm coherence. Beta-band coherence could primarily be observed in synergy 2. Coherence around the Piper rhythm was likewise visible in synergy 2, revealing synchronisation in two rhythms at this mode. Cortico-synergy coherence at lower frequencies (<10 Hz) was also present, but since this might have been caused by movement artefacts, we abstained from investigating this further. Broad-band cortico-synergy coherence estimates (10-250 Hz) did not reveal any significant contributions at frequencies above the Piper rhythm.

Clusters containing significant cortico-synergy coherence modulation between pre- and post-training timepoints were specifically found around 40 Hz (i.e., Piper rhythm). Piper rhythm cortico-synergy coherence decreased as a function of short-term postural training for all three synergies (Figure 2.4C).

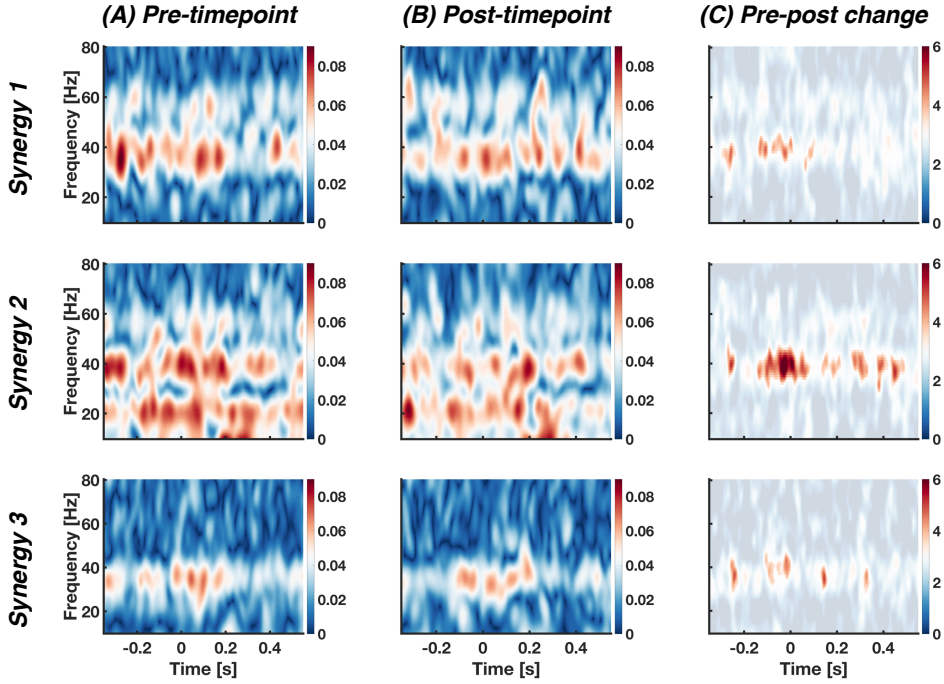


Figure 2.4 – Cortico-synergy time-frequency-coherence representations before and after short-term postural training and corresponding statistics. (A-B) Grand average cortico-synergy time-frequency-coherence representations as estimated between the source-reconstructed left paracentral lobule activity and temporal activation patterns. Time 0s corresponds to the mechanical perturbation onset. (C) Time-frequency-statistics representations estimated with cluster-based permutation tests using dependent *t*-tests as test statistic. Non-transparent clusters feature *t*-values considered as significant, revealing cortico-synergy coherence modulation around 40 Hz. Positive *t*-values correspond to a coherence decrease.

Kinematics

The time constants of the fitted exponential decays on the most central auto-covariance functions were lower at the post-training timepoint (-0.244, 95% confidence intervals: [-0.248; -0.240]) compared to pre-training timepoint (-0.203, 95% confidence intervals: [-0.208; -0.198]) (Figure 2.5). This decrease in time constant reveals that participants regained balance quicker after the mechanical perturbations after training, reflecting the effectiveness of the training at the behavioural level.

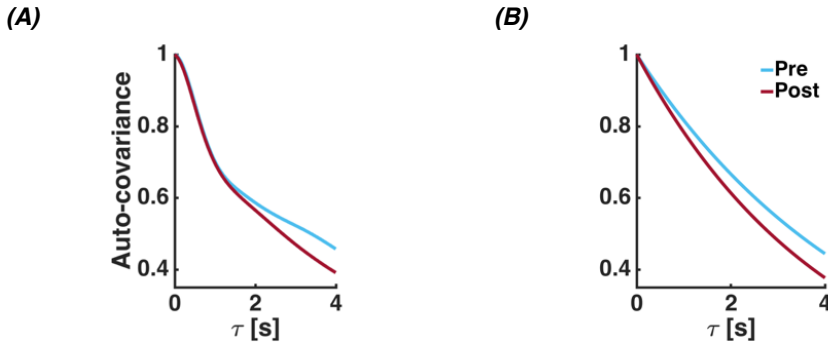


Figure 2.5 – Auto-covariance as a function of time lag of the principal component capturing most mediolateral sway. (A) Graphs represent auto-covariance functions of the most central principal component around zero time-lag at pre- and post-timepoint. The principal component capturing most mediolateral sway of the bilateral hip and shoulder markers served to estimate the exponential decay of the auto-covariance function. (B) A first-order exponential function was fitted on the first exponential decay after full convolution alignment of the principal component.

Discussion

Muscle synergies have traditionally been considered as spinally driven spatiotemporal motor patterns. The spinal cord can generate neural output largely independent of the supra-spinal levels (Grillner & Zangger, 1979). Over the years, evidence for independent spinal control came from studies on animal locomotion, which strongly relies on seemingly self-sustaining, rhythmic muscle activations to position the extremities (Grillner, 1985; Stein, 2005). More recent work suggests the involvement of the sensorimotor cortex in the formation and control of muscle synergies in such modes of motor control (Aumann & Prut, 2015; Pirondini et al., 2017).

In the current study, we examined functional cortico-synergy connectivity in terms of cortical muscle synergy coherence in postural control and its plasticity with short-term motor training. We found that: (i) temporal activation patterns of muscle synergies are coherent with neural oscillations in the motor cortex, specifically in the paracentral lobule; (ii) the Piper rhythm involves functional cortico-spinal oscillations emerging during a postural control task; and (iii) cortico-synergy coherence around the Piper rhythm decreases as a function of postural training.

Neural activation along the cortico-spinal axis is often believed to primarily reflect selective neural control of individual muscles (Bizzi & Cheung, 2013). One example is beta-band coupling of the primary motor cortex to homologous hand muscles, which decreases during bimanual coordination when compared to unimanual movement (de Vries et al., 2016). This drop in beta-band cortico-muscular coherence is likely to present a more dynamical and less stable motor output (Kristeva et al., 2007). The findings of the current study, however, demonstrate long-range synchronisation between the motor cortex and multiple muscles jointly, indicative of an effective (i.e., low-dimensional) neural circuitry to propagate neural oscillations. Cortico-spinal connectivity consists of frequency-locked communication between cortical motor areas and motor unit pools along mono-synaptic descending projections, diverging to muscles belonging to a single muscle synergy (Aumann & Prut, 2015; Nazarpour et al., 2012). Firing-rate-specific coupling may occur via closed neural loops (Lemon, 2008), enabling the distinction between multiple muscle synergy loops, tailored to meet the biomechanical demands of the motor task at hand. Neural loops convey beta-band oscillations to maintain a stable motor state (Engel & Fries, 2010), which become uncorrelated when shifting to higher movement frequencies (Brown, 2000). Distinguishable roles of the beta- and gamma-band oscillations may motivate the previous belief that cortico-spinal synchrony controls individual muscles. Multiple synchrony rhythms may be involved in a single muscle synergy, as we identified synchronisation of both beta and gamma oscillations. However, it remains to be seen whether the oscillations of this synchronisation in the beta and gamma band are propagated along the same neural pathways or by parallel-adjacent pathways. In any case, our results show that the common neural input at the muscular level contains super-imposed correlated activity that is propagated from the motor cortex along cortico-spinal pathways.

We found Piper rhythm coherence between the motor cortex and synergistic muscle groups of the contra-lateral leg. Apparently, the cortico-spinal tract conveys the Piper rhythm from the motor cortex down to groups of muscles simultaneously rather than to individual muscles. Cortico-synergy commands may be considered higher order regulations to meet the specific postural demands. Neither the muscle synergy structure (muscle weightings and temporal activation patterns), nor its complexity (reconstruction quality) varied with postural training. That is, our participants employed a selection of a reasonably fixed set of cortical muscle synergy representations to meet postural demands. In fact, this can be confirmed by

earlier studies showing largely constant muscle synergy representations at short time scale (Scott, 2003; Ting, 2007). While the structure and complexity of this set of cortical muscle synergy representations was unaffected by short-term postural training, the task-specific cortico-synergy connectivity did modulate with postural training, i.e., it decreased in the Piper rhythm. Obviously, the motor system modulates by changing the firing rates of neural populations rather than adjusting the muscle synergies themselves (Schieber, 2002).



Regional brain activity modulates when acquiring a novel motor task (Dayan & Cohen, 2011). Short-term motor skill acquisition is associated with a decreased activity of the primary motor areas (Floyer-Lea & Matthews, 2005). Arguably, the recruitment of less coherent or smaller neural populations is needed to generate proper output performing a motor task. Here, the decrease in coherence at the Piper rhythm indicates a reduced neuronal synchrony in the left paracentral lobule after postural training. The processes of neural activation may have been relegated to lower neural centres, for example, the alpha motoneurons of the brainstem or spinal cord. Interestingly, the cortical activity of the left medial sensorimotor cortex following mechanical perturbations was not modulated by postural training (Figure S2.2).

Earlier studies on cortico-muscular connectivity found a functional role for beta oscillations in practising a novel motor task (Houweling et al., 2008; Larsen et al., 2016; Perez et al., 2006). Their neural oscillatory upregulation reflects an increased likelihood to retain a stable motor output (Baker, 2007). While the function to maintain a constant motor output is typically assigned to the beta-band oscillations (Omlor et al., 2007), current findings support the hypothesis of Piper rhythm involvement in motor practice. The Piper rhythm has been associated with the readiness to perform strong isometric and slow dynamic muscle contractions (Mehrkanoon et al., 2014; Mendez-Balbuena et al., 2011; Omlor et al., 2007; Petersen et al., 2012; Schoffelen et al., 2005). Cortico-spinal gamma-band synchronisation primarily emerges in dynamic motor tasks involving multi-sensory and complex sensorimotor integration (Engel & Fries, 2010). Deafferented patients do not display cortico-muscular low-gamma synchrony between the motor cortex and upper extremity muscles during dynamic visuomotor tasks. This hints at a pivotal role of the Piper rhythm in proprioceptive feedback (Patino et al., 2008). Our Piper rhythm modulation during postural training might have been caused by a sensory re-weighting yielding a down-regulation of

proprioceptive inputs. This is essential to control unilateral posture on a moving surface (van Dieën et al., 2015).

Here, we focused on the coupling between the sensorimotor cortex and muscle synergies by examining connectivity using a non-directional measure (i.e., coherence). Although coherence is generally accepted to quantify connectivity, by construction it does not provide any information about causality and cross-frequency coupling. The application of other connectivity measures (like bicoherence, (spectral) Granger causality, or generalised phase locking) may extend the insights into the cortico-synergy connectivity. Future research should address the directionality of the cortico-synergy connectivity and potential cross-frequency synchronisation.

From a behavioural point of the view, the decrease in Piper rhythm might be related to the predictability of the repetitive postural perturbations. A relatively high predictability of the perturbation-induced task may lead to a decrease in the Piper rhythm as a higher Piper rhythm has positively been correlated to an increased probability of movement prediction errors (Mehrkanoon et al., 2014). Here, mechanical perturbations had a constant magnitude of $|3^\circ|$ and were imposed at a rate of ± 0.8 Hz. Hence, inter-perturbation variability comprised the inter-perturbation time of 0-200ms and perturbation direction (either clockwise or counter-clockwise). An increased capability to anticipate the mechanical perturbation (i.e., better ability to predict the biomechanical outcomes) will lead to a decrease in the Piper rhythm.

Conclusion

Coherent cortico-synergy pathways communicate neural oscillations between motor cortex and muscle synergies. Consequently, these cortico-synergy pathways act as a vehicle to transfer frequency-locked oscillatory activity from motor cortex to groups of muscles in the periphery and back to sensory areas. The transport along these neural pathways appears plastic as coherent oscillations of the Piper rhythm decrease during short-term postural training.

Supplementary material Chapter 2

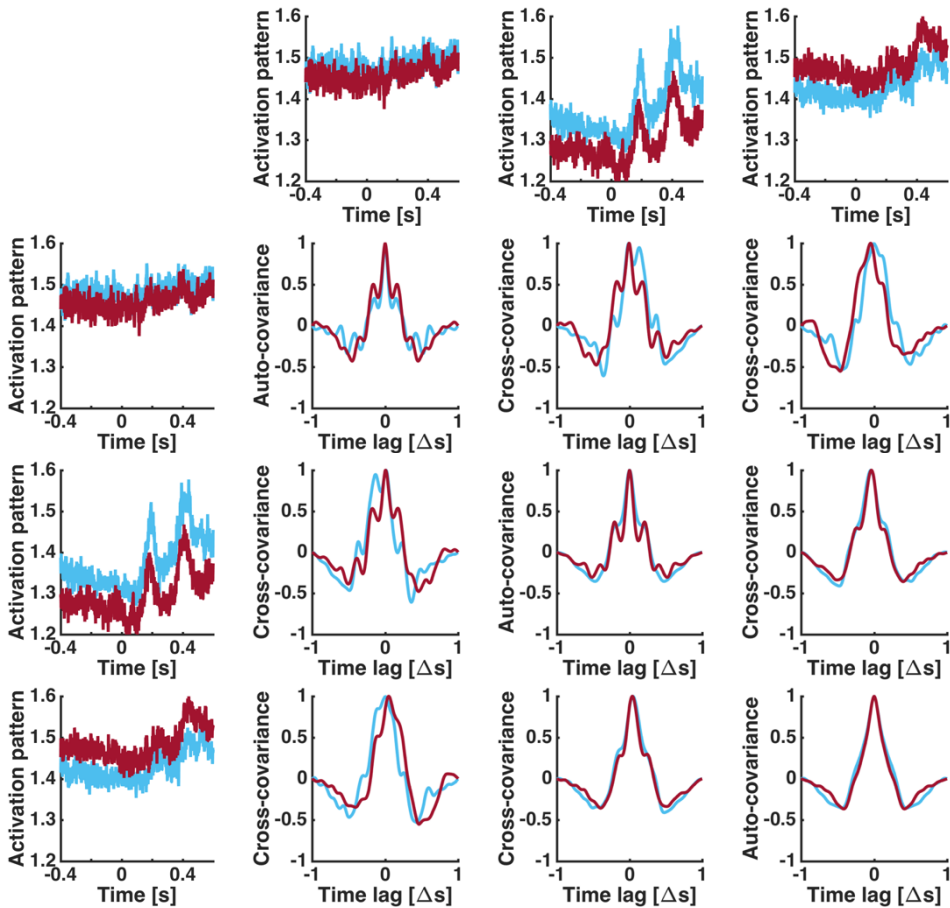


Figure S2.1 – Pairwise auto- and cross-covariance between the temporal activation patterns of the muscle synergies. Left and upper panels represent the temporal activation patterns after the decomposition of the non-filtered EMG. Time 0s indicates perturbation onset. The remaining panels depict the pairwise auto- and cross-covariance estimates between the temporal activation patterns. Auto- and cross-covariance functions were estimated on the mean temporal activation patterns over perturbations. Auto- and cross-covariance were estimated to examine the temporal relationships between the muscle synergies following the mechanical perturbation.



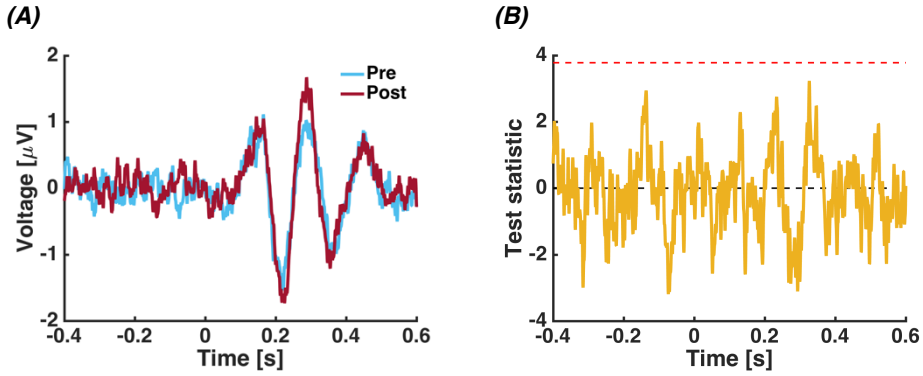


Figure S2.2 – Grand event-related potentials of the left paracentral lobule with corresponding pre-post statistics. (A) Source-reconstructed event-related potentials pooled over perturbations and participants of pre- and post-timepoint. Potential courses represent the mean activity of the left paracentral lobule. (B) Test statistic of a paired t -test comparing the event-related potentials of pre- and post-timepoints. Dashed red line indicates significance threshold. Results indicate no significant modulation of the event-related potentials as a function of the balance training.

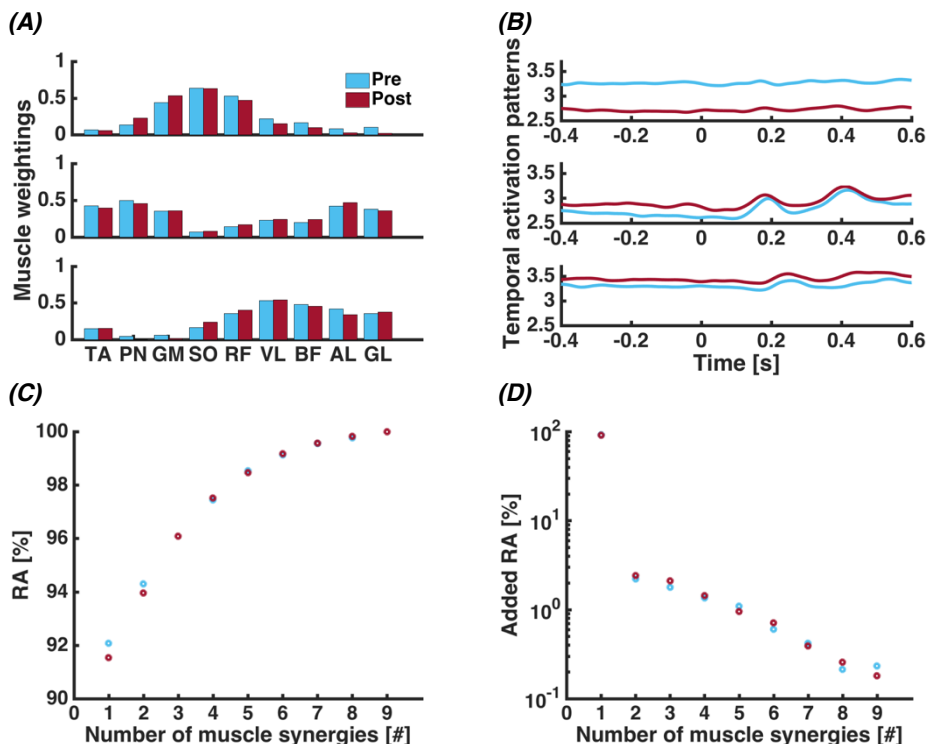


Figure S2.3 – Muscle synergies computed using the conventional decomposition procedure with the low-pass filtered electromyographic data. Grand average (A) muscle weighting coefficients, (B) temporal activation patterns, (C) reconstruction accuracy, (D) added reconstruction accuracy using the low-pass filtered electromyographic data as input of the multivariate decomposition. (A) Muscle weighting coefficients of the nine unilateral stance leg muscle for three muscle synergies. The nine stance leg muscles were tibialis anterior (TA), peroneus longus (PN), gastrocnemius medialis (GM), soleus (SO), rectus femoris (RF), vastus lateralis (VL), biceps femoris (BF), adductor longus (AL), and gluteus medius (GL). Here, virtual activation patterns were estimated by multiplying the rectified electromyographic signals (including broad spectral content) with the inverse of the muscle weightings. (B) Temporal activation patterns of the three muscle synergies. Graphs depict the mean time-locked activation patterns around perturbation onset. Time 0s indicates mechanical perturbation onset. (C) Reconstruction accuracy as a function of the a-priori determined number of muscle synergies. RA: reconstruction accuracy. (D) Added reconstruction accuracy by iteratively adding muscle synergies. RA: reconstruction accuracy.

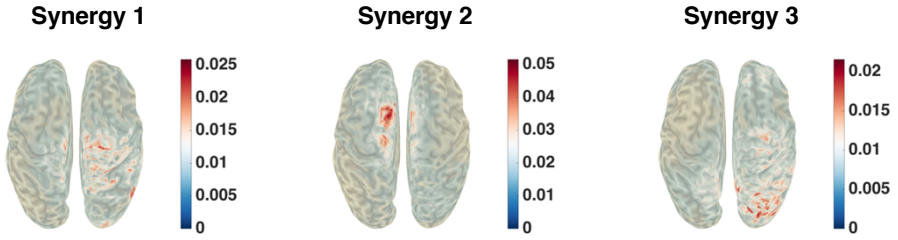


Figure S2.4 – Coherent cortico-spinal sources using virtual activation patterns. Cortical sources showing maximal cortico-synergy coherence. Cross-spectral density matrices of the Dynamic Imaging of Coherent Sources spatial filters were extended with the virtual activation patterns (i.e., electromyographic (EMG) signals multiplied with the inverse of the muscle weightings after multivariate decomposition of the low-pass filtered EMG). Adaptive spatial filters identified cortico-synergy coherence sources for the virtual activation patterns. Voxels were masked by only highlighting voxels containing the highest 95% cortico-synergy coherence.

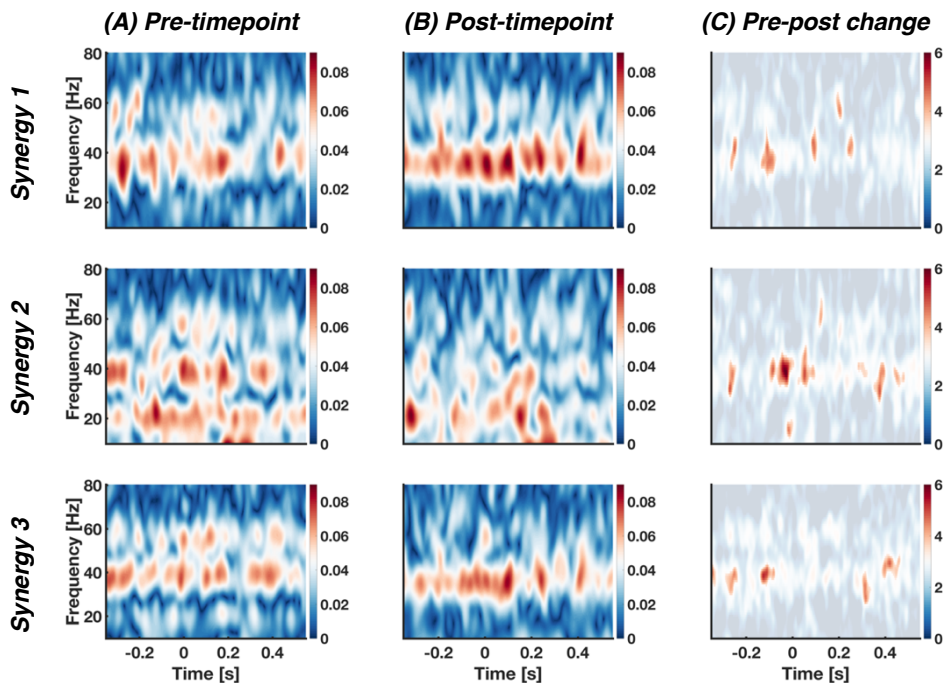


Figure S2.5 – Cortico-synergy coherence representations using source-reconstructed electroencephalographic activity of the left paracentral lobule and virtual activation patterns. (A-B) grand average cortico-synergy coherence representations as estimated between the source-reconstructed left paracentral lobule activity and virtual activation patterns (i.e., electromyographic (EMG) signals multiplied with the inverse of the muscle weightings after multivariate decomposition of the low-pass filtered EMG). Time 0s corresponds to the mechanical perturbation onset. (C) Time-frequency-statistics representations using cluster-based permutation testing with dependent *t*-tests. Non-transparent voxels indicate significant coherence modulation to evaluate training effects of pre- and post-timepoint.



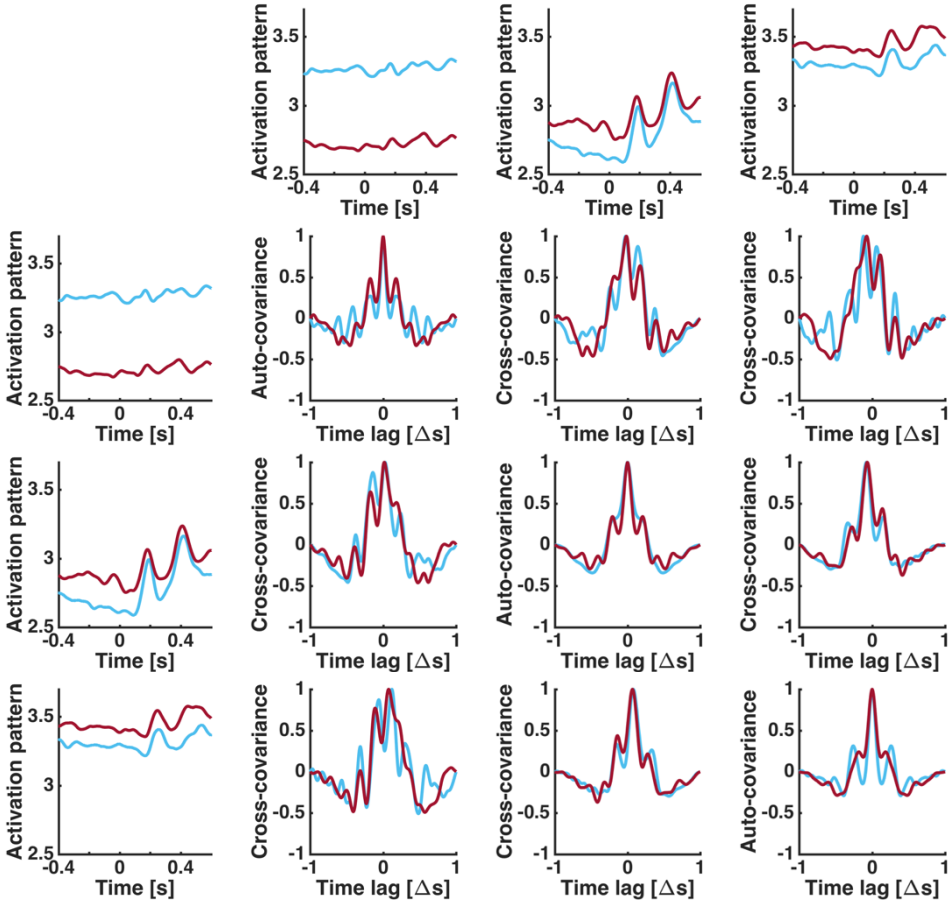
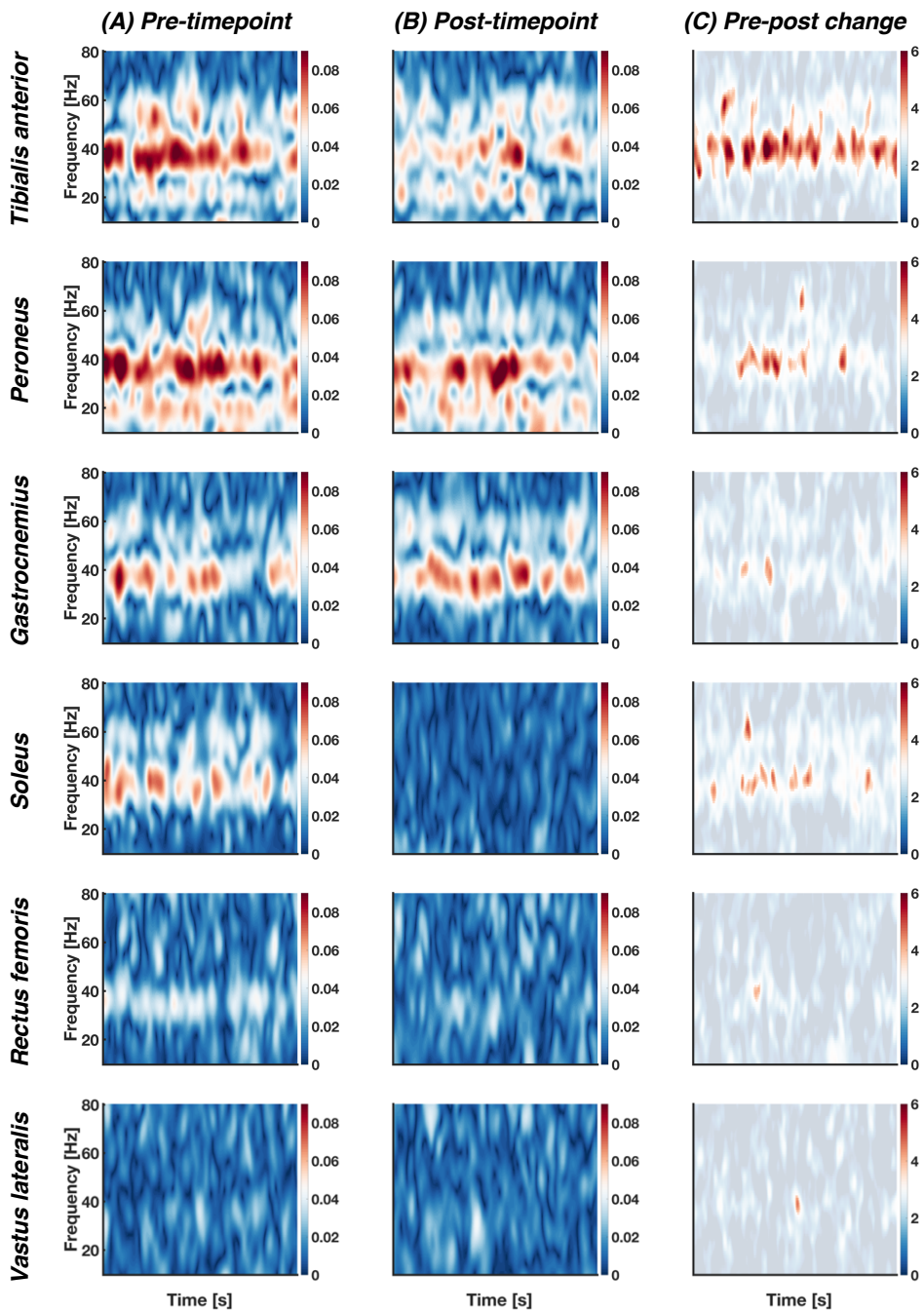


Figure S2.6 – Pairwise auto- and cross-covariance between the low-pass filtered activation patterns. Left and upper panels represent the temporal activation patterns, which was the direct output of the multivariate decomposition of the low-pass filtered EMG. Time 0s indicates perturbation onset. Remaining panels show the pairwise auto- and cross-covariance estimates between the temporal activation patterns. Auto- and cross-covariance functions were estimated on the mean temporal activation patterns over perturbations. Auto- and cross-covariance were estimated to examine the temporal relationships between the muscle synergies following the mechanical perturbation.



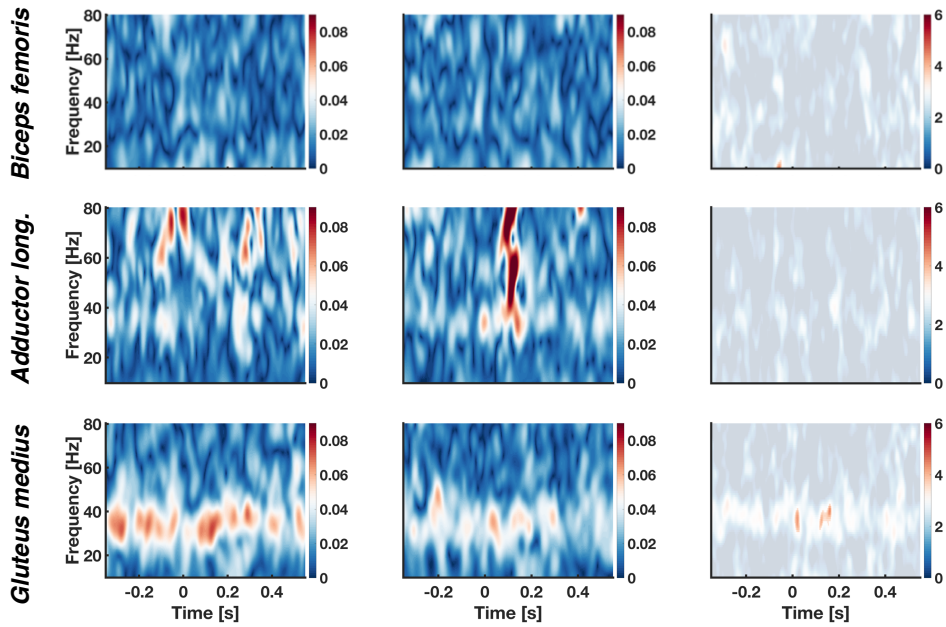


Figure S2.7 – Pairwise cortico-muscular coherence estimates between the source-reconstructed left paracentral lobule activity and electromyography of individual muscles. (A-B) Cortico-muscular time-frequency coherence representations as estimated between the left paracentral lobule and rectified electromyographic time series of individual muscles at pre- and post-timepoint. Time 0s corresponds to the mechanical perturbation onset. (C) Time-frequency-statistics representations indicating pre-post coherence modulation using cluster-based permutation tests. Non-transparent voxels indicate significant coherence modulation to evaluate training effects of pre- and post-timepoint.

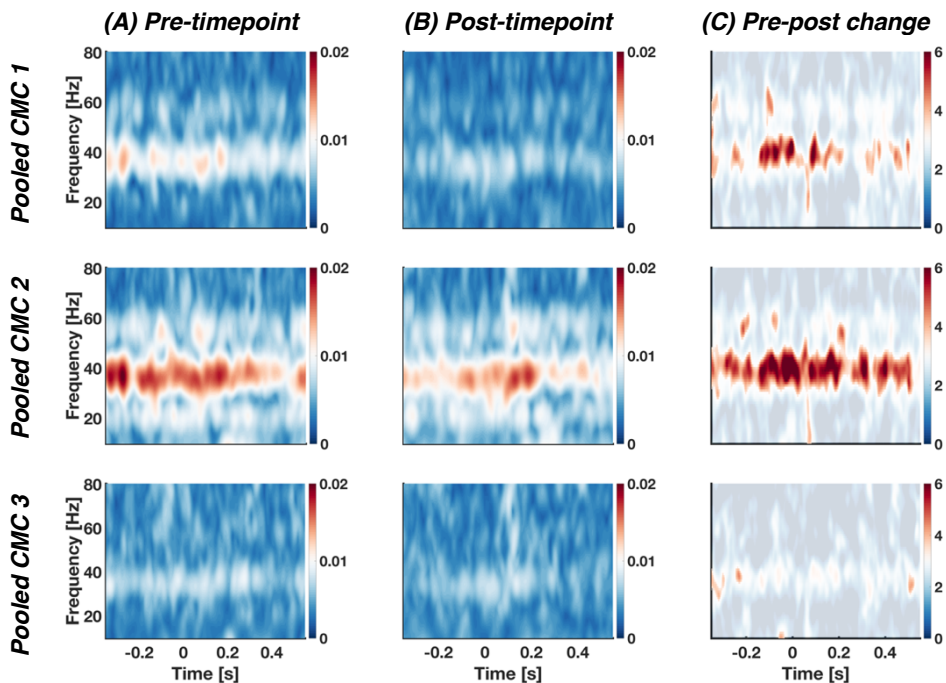
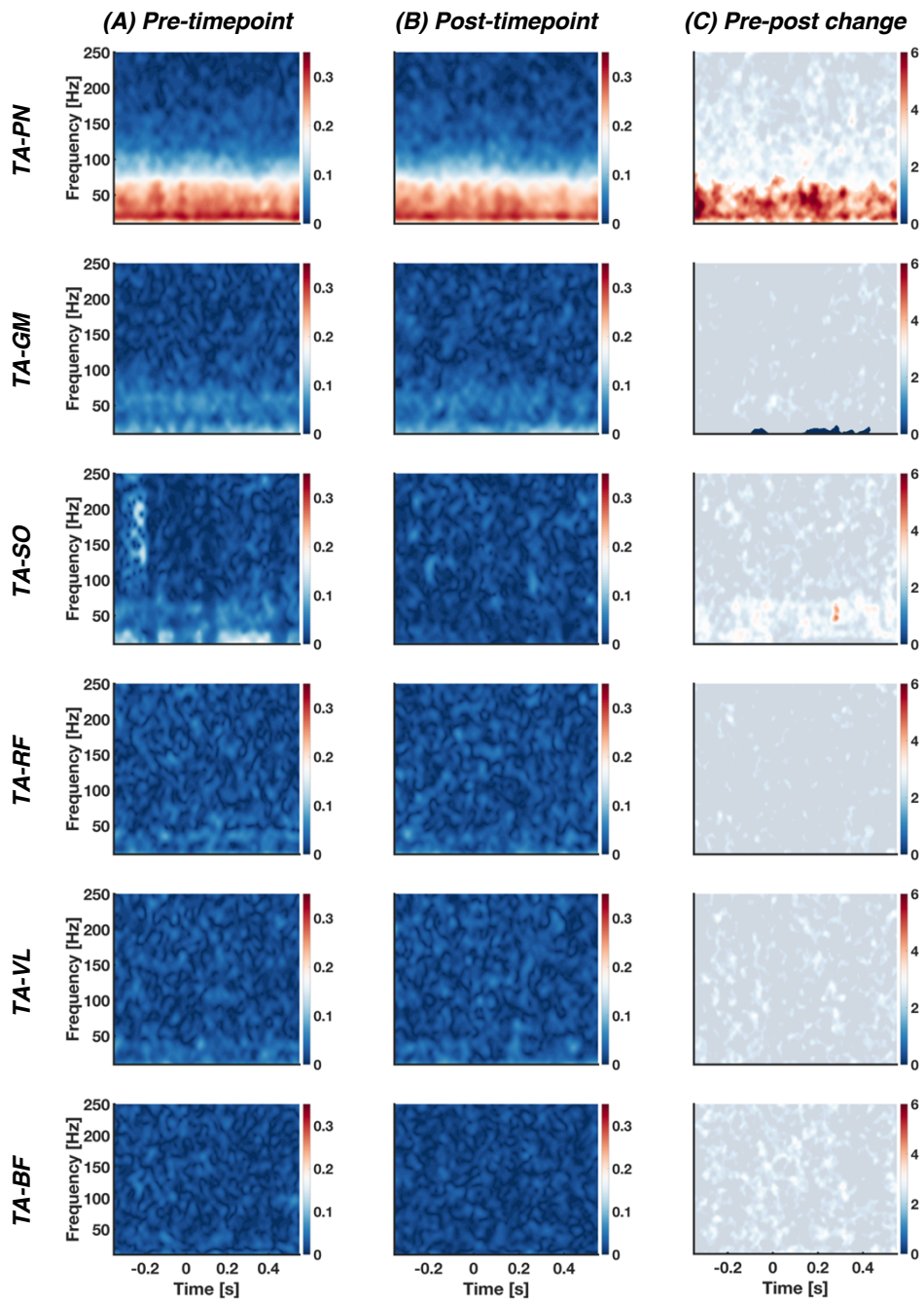


Figure S2.8 – Cortico-synergy coherence representations using source-reconstructed electroencephalographic activity of the left paracentral lobule and pooled cortico-muscular coherence estimates. (A-B) Grand average cortico-synergy coherence representations as estimated between the source-reconstructed left paracentral lobule activity and pooled cortico-muscular coherence estimates pre- and post-training. The cortico-muscular coherence magnitudes were linearly scaled to the muscle weightings of a particular muscle weighting. After linear scaling, all cortico-muscular coherence estimates of the nine muscles belonging to a certain synergy were pooled, resulting in a synergy-specific coherence estimate. Time 0s corresponds to the mechanical perturbation onset. (C) Time-frequency-statistics representations using cluster-based permutation testing with dependent *t*-tests. Non-transparent voxels indicate significant coherence modulation to evaluate training effects of pre- and post-timepoint.



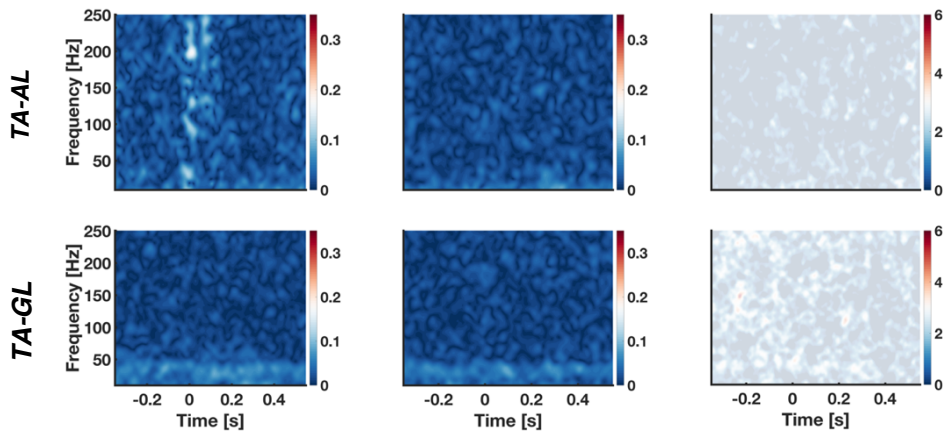


Figure S2.9 – Broadband inter-muscular coherence estimates between the tibialis anterior and the other stance leg muscles. (A-B) Inter-muscular time-frequency coherence representations as estimated between the rectified electromyographic time series of individual muscles at pre- and post-timepoint. The nine stance leg muscles were tibialis anterior (TA), peroneus longus (PN), gastrocnemius medialis (GM), soleus (SO), rectus femoris (RF), vastus lateralis (VL), biceps femoris (BF), adductor longus (AL), and gluteus medius (GL). Time 0s corresponds to the mechanical perturbation onset. (C) Time-frequency-statistics representations indicating pre-post coherence modulation using cluster-based permutation tests. Non-transparent voxels indicate significant coherence modulation to evaluate training effects of pre- and post-timepoint.

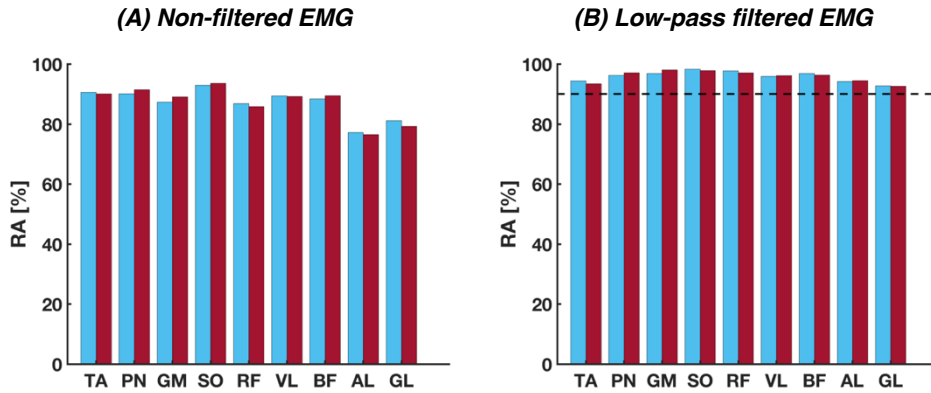


Figure S2.10 – Single muscle reconstruction accuracy (RA) when extracting three muscle synergies. (A-B) Single muscle RA for both non-filtered and low-pass filtered electromyographic (EMG) time series. EMG time series were concatenated over trials and participants. Blue and red bars represent RA at pre- and post-timepoint.

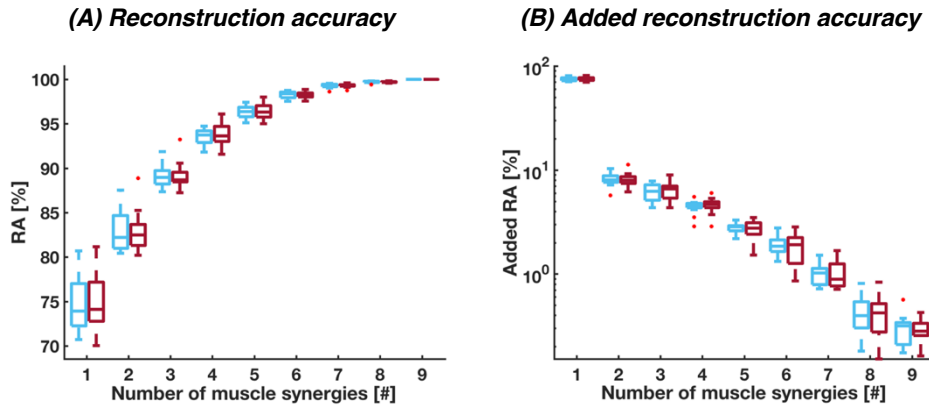


Figure S2.11 – Reconstruction accuracy (RA) when extracting muscle synergies for every participant individually. Deviation of the (A) reconstruction accuracy and (B) added reconstruction accuracy across participants for pre- and post-timepoint. Boxplots belonging to pre- and post-timepoint are coloured blue and red, respectively. The non-filtered electromyographic time series were used for the computation of the RA.



Differential sets of cortical muscle synergy signatures during adult locomotion



Muscle synergy assessments are often employed to evaluate the modular organisation of the spinal cord during a locomotion task. While they provide valuable insights into the pattern formation of the α -motoneurons at the spinal cord, by construction they cannot capture control from supra-spinal layers. We examined how locomotor muscle synergies are represented in the sensorimotor cortex, with particular focus on the cortico-synergy coherence as a measure of coupling along the cortico-spinal tract. Non-negative matrix factorization served to decompose multivariate electromyographic signals into muscle synergies. Their representations were localised in the cortex using coherence-based beamforming. Overall, the cortico-synergy coherence was maximal in sensorimotor areas especially in the beta-frequency band. However, only for the synergies timed to heel strike, that are related to the double support phases, the coherence was significant. These coherences were closely related to the timing of the activation patterns of the synergies, suggesting sensorimotor cortex to be strongly involved in emergence and control of these synergies.

Adapted from: C.S. Zandvoort, A. Daffertshofer, & N. Dominici (2021). *Differential sets of cortical muscle synergy signatures during adult locomotion*. 10th International IEEE Engineering in Medicine and Biology Society Conference on Neural Engineering (NER), EMBS NER 2021 – Proceedings (pp. 1070-1073). [9441206] Institute of Electrical and Electronics Engineers, Inc. doi: [10.1109/NER49283.2021.9441206](https://doi.org/10.1109/NER49283.2021.9441206)

Introduction

A major question in motor control is how the central nervous system (CNS) regulates muscular activation during locomotion. The CNS combines neural patterns of simultaneously operating muscles allowing for controlling them using low-dimensional commands (d'Avella et al., 2003). That is, such combinations effectively reduce the dimensionality of the neural activity generated by spinal circuitries, typically coined muscle synergies. Although the exact neural mechanisms underlying the muscle synergies remain enigmatic (Bizzi & Cheung, 2013; Tresch & Jarc, 2009), human electrophysiological recordings have shown the existence of such a modular organisation in the spinal cord during walking (Dominici et al., 2011). Such recordings often consist of co-registering many electromyographic (EMG) signals. Subsequent multivariate statistics (e.g., non-negative matrix factorization (NNMF)) revealed that four to five muscle synergies suffice to explain the EMG's envelope dynamics during walking (Ivanenko et al., 2004). This approach adequately captures the modular organisation of α -motoneuronal populations (Ivanenko et al., 2006), but which neural structures primarily control the locomotor muscle synergies remain unclear.

Neural activity in the spinal cord arguably stems from central pattern generators (CPGs) (Grillner & El Manira, 2020). Yet, in human locomotion the input of sensory and supra-spinal control seems to be crucial (Grillner, 2006; Hart & Giszter, 2010; Lacquaniti et al., 2012). Thanks to recent advances in data analysis, non-invasive electrophysiological recordings of the cortical areas, i.e., electro-encephalography (EEG), have proven valuable tools to assess dynamical motor control tasks like walking (Bruijn et al., 2015). Recent experimental findings of a dynamic postural control task indicated a pivotal role for the sensorimotor cortex in the formation of muscle synergies (Zandvoort et al., 2019). There, muscle synergy activity was shown to be phase locked with neural oscillations in the sensorimotor cortex. The cortico-synergy coupling appeared most in the beta- and (part of the) gamma-frequency bands (13-30 Hz and \sim 40 Hz, respectively). When it comes to walking, beta-band activity in the motor cortex has been reported to synchronise with the activity of shank muscles (bilateral tibialis anterior), especially during double support phases (Roeder et al., 2018). To what extent this also applies to cortico-synergy coupling during walking and, hence, whether one may speak of cortical-synergy control, remains to be elucidated.

Based on our recent findings on postural control, we hypothesised that locomotor muscle synergies also manifest in the phase-locked beta-band oscillations of the sensorimotor cortex. To investigate this, we employed cortico-synergy coherence as a measure of functional connectivity along the cortico-spinal tract.

Methods

Participants and experimental protocol

The experimental protocol of this study was approved by the local ethical committee of the Faculty of Behavioural and Movement Sciences (reference #VCWE-2020-006). Twelve healthy adults (seven females; mean age: 23.0 ± 8.0 years [mean \pm SD]; weight: 63.9 ± 6.0 kg, height: 1.74 ± 0.08 m) participated in the study. Participants were recruited from a student pool at the Faculty of Behavioural and Movement Sciences and received educational credits. Participants were asked to walk at a comfortable walking speed. Data were acquired during 30 over-ground trials and six treadmill trials, corresponding to a total of 403 ± 22 strides, and a resting state trial recorded at the beginning of the experiment.

Data acquisition

Kinematic and video data were acquired with a Vicon motion capturing system (Oxford, UK) sampled at a rate of 100 Hz. Twenty-three reflective passive markers with a diameter of 14 mm were attached to the participant's skin. As this study is integrated into a larger project, we focused on the markers that were bilaterally placed on the following landmarks: lateral malleolus, heel, and fifth metatarsophalangeal joint.

Surface EMG of a set of 24 muscles was acquired, which included the bilateral activity of the tibialis anterior (TA), gastrocnemius medialis (GM), gastrocnemius lateralis (GL), soleus (SOL), rectus femoris (RF), vastus lateralis (VL), vastus medialis (VM), biceps femoris (BF), semitendinosus (SEM), tensor fasciae latae (TFL), gluteus maximus (GLM), and erector spinae (ES; recorded at L2). After cleaning the skin with alcohol, Ag/AgCl electrode pairs were attached according to SENIAM guidelines (Hermens et al., 2000). Movement artefacts were minimised by fixating electrodes and sensor boxes using adhesive tape. Two 16-channel wireless systems (Cometa Mini Wave Plus wireless, Bareggio, Italy)



served to record the EMG signals that were digitised at 1 kHz after online band-pass filtering (10 Hz - 500 Hz).

Cortical activity was recorded using a 64-channel EEG cap (eegoTM mylab, ANT B.V., Enschede, the Netherlands). Electrode placement was based on the 10-20 system with CPz as reference (impedance values were below 10 k Ω). The EEG was sampled at a rate of 2,048 Hz. Sampling of kinematic, EMG and EEG data were synchronised.

Data analysis

The gait cycle (stride) was defined with respect to the right leg movement, beginning with right foot contact with the surface (heel strike) to the consecutive right foot contact, and thus equalled two steps. Foot-strike and foot-off onsets were automatically detected using a peak-detection algorithm based on the bilateral heel marker and its first time derivative (Roerdink et al., 2008).

For data pre-processing and artefact rejection we proceeded as follows. EEG time series were band-pass (5-250 Hz) and notch filtered (at 50, 100, ..., 200 Hz). Bad channels (defined as mean values outside the 10·mean or SD-values outside the 3·SD interval of all channels) were spherically interpolated using neighbouring channels. Next, EEG data were decomposed using independent component analysis to identify and remove muscular and movement artefacts (e.g., components with spectral composition atypical for EEG were omitted). EMG data were high-pass filtered (30 Hz) and notch filtered (at 50, 100, ..., 200 Hz).

The EMG signals were rectified with the Hilbert transform, low-pass filtered (10 Hz), and decomposed into muscle synergies using NNMF. For every subject, the NNMF was applied to the averaged muscle activation patterns over all strides to identify the underlying muscular coefficients and temporal activation patterns. To construct high-frequency temporal patterns of the muscle synergies, the rectified but not low-pass filtered EMG was weighted with the (pseudo-)inverse of the muscular coefficients. From hereon we refer to these patterns as virtual activation patterns that served as input for the subsequent cortico-synergy coherence estimates. As mentioned in the introduction, this approach helped

identifying phase locking between activity in motor areas and muscle synergies in terms of cortico-synergy coherence (Zandvoort et al., 2019).

We employed Dynamic Imaging of Coherent Sources (DICS) beamformers to localise cortical areas with maximal cortico-synergy coherence with the virtual activation patterns. White and grey matter volumes (2-mm grid) were obtained from a template MRI (Fillmore, Phillips-Meek, et al., 2015) within which spatial filters maximising coherence in beta-frequency band were constructed. The resulting sources were statistically evaluated using cluster-based permutation testing (1,024 random permutations). Critical alpha and cluster-alpha levels were both set to 0.001. The first served as significance threshold when contrasting coherence in the double support phases (i.e., maximal coherence during the gait cycle) vis-à-vis coherence during resting state. We used the LONI probabilistic brain atlas (Fillmore, Richards, et al., 2015) to map anatomy.



Source time series of the cortical activity exhibiting maximal coherence were reconstructed and used for a subsequent analysis. In particular, time-frequency coherence was estimated between virtual activation patterns and superior frontal and precentral gyri (i.e., the cortical region revealing maximal coherence) using short-time Fourier transforms with 0.2s Hanning windows.

Results

We identified four muscle synergies accounting for $94.1 \pm 1.2\%$ of the reconstruction accuracy (Zandvoort et al., 2019). The temporal activation patterns and spatial distributions (i.e., muscle coefficients) of the decomposed patterns were in line with the findings of earlier studies (Figure 3.1). These temporal activation patterns could be divided into two sets: Patterns 1 and 3 are timed during the double support phases and are involved in heel-strike and toe-off; patterns 2 and 4 are primarily active during single support phases.

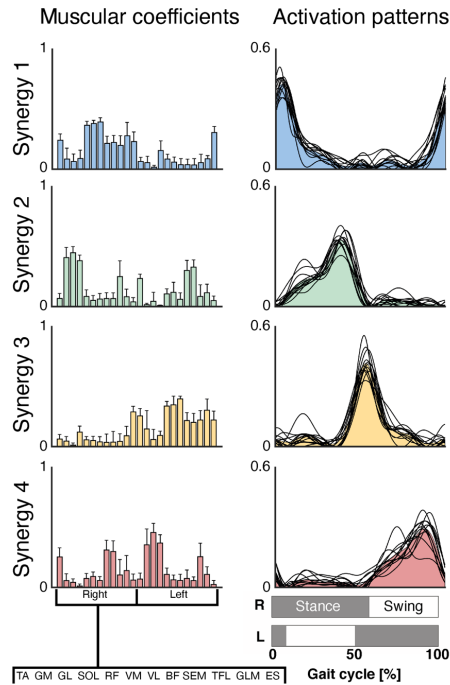


Figure 3.1 – Spatial organisation (left column) and activation patterns (right column) of the decomposed muscular activation patterns. Muscular coefficients are presented as mean and standard deviation (i.e., bars and error bars) over participants. Individual and group-average temporal activation patterns are shown as black curves and coloured surfaces, respectively. R: right; L: left

Coherence findings on sensor-level (not shown) identified that the maximal coherence for all synergies was expected during bilateral double support phases. The DICS beamforming yielded maximal statistical differences between beta-band coherences in double support phases versus resting state in bilateral premotor and sensorimotor areas of the cortex (Figure 3.2). The maximum t-statistic was localised in superior frontal gyrus (synergy 1) and precentral gyrus (synergy 3). In line with the findings of the synergy timings, their cortical representations could also be distinguished into two sets as only synergies 1 and 3 (i.e., the bilateral patterns timed at the double support phases) revealed statistically significant sources.

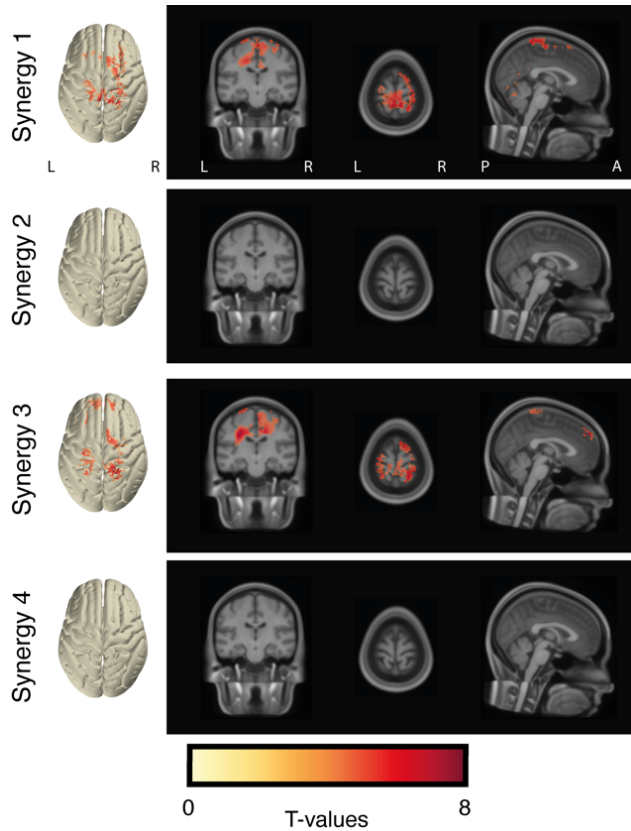


Figure 3.2 – Localisation of the muscle synergies in the cerebral cortex. Coloured dimension represents the test statistic of the statistical contrast between the coherence during locomotion (i.e., double support phases) and resting state. L: left; R: right; P: posterior; A: anterior.

As shown in Figure 3.3, the beta-band coherences modulated as a function of the gait cycle for synergies 1 and 3. Here, we focus on synergies 1 and 3 because only they displayed significant sources at the cortex. For these synergies, beta-band coherences appeared to be maximal during the double support phases and their change in time agreed with that of the corresponding virtual activation patterns. For the single support phases, no significant beta-band coherence could be observed (see our note above).

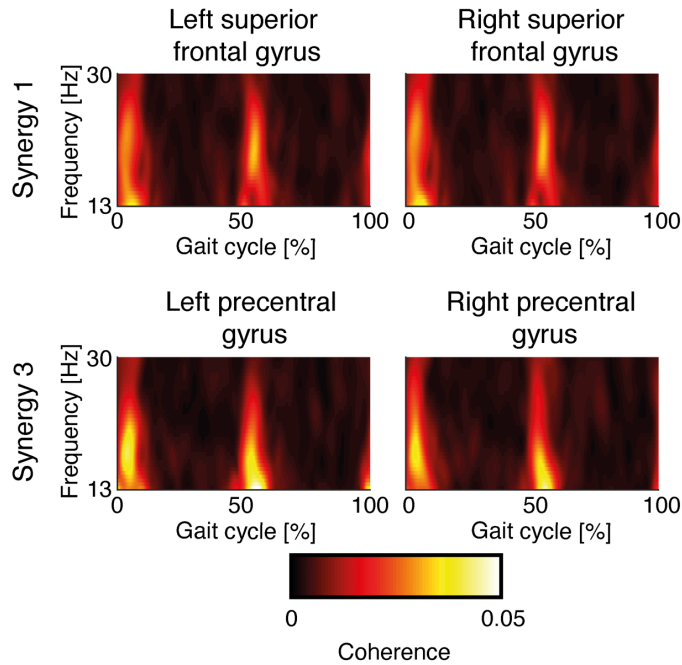


Figure 3.3 – Cortico-synergy coherence between the bilateral superior frontal gyri and synergy 1, and bilateral precentral gyri and synergy 3. Coherence was estimated as the magnitude-squared coherence and as a function of normalised time (expressed as percentage of the gait cycle) and beta-band frequencies.

Discussion

We examined how muscle synergies may be represented in the cerebral cortex during walking. To identify possible neural interactions, we focused on the cortico-synergy coherence as a measure to quantify the long-distance synchronisation in the motor system. Our findings revealed that cortico-synergy synchronisation was particularly evident in the sensorimotor cortex in the beta-frequency band.

Beta-band synchrony is a well-established signature within the motor system during voluntary movement and is apparent in both local and long-range synchronisation in terms of cortical power and cortico-spinal synchronisation (van Wijk et al., 2012b). Neural oscillations over long distances are thought to be conveyed via the monosynaptic pyramidal tracts of the cortico-spinal axis. Arguably, the main function of beta-band oscillations is to provide a stable outflow from the cortical motor nuclei to maintain a particular posture and/or movement state (Baker, 2007).

Thus far, the majority of experimental studies focused on the upper extremity tasks (van Wijk et al., 2012b). More recently, cortico-muscular coherence in the beta-band was identified during locomotion (Roeder et al., 2018). These beta-band oscillations are associated with the postural stability during locomotion (Bruijn et al., 2015).

Neural oscillations from the motor cortex are locked with the different synergies possibly via segregated cortico-synergy loops (Aumann & Prut, 2015). These loops activate cooperating groups of muscles through activation of α -motoneuronal populations. We found synchronisation between sensorimotor cortex and muscle synergies to differ between (sets of) synergies. The coherences with synergies 1 and 3 were stronger than those with synergies 2 and 4. Hence, one may argue that the sensorimotor cortex is especially crucial in establishing the control of synergies 1 and 3.



One may speculate about the cause of the 2×2 grouping of the four muscle synergies. In fact, neonatal stepping can be represented by just two muscle synergies (Dominici et al., 2011). These stepping has also been reported in premature and anencephalic infants (Allen & Capute, 1986; Peiper, 1963) suggesting a primary role of spinal and brainstem mechanisms, arguably due to an immature infrastructure of the motor cortex and cortico-spinal tract at early age and/or in pathological cases. Needless to say, neonates cannot walk independently. Interestingly, however, the temporal organisation of these neonatal synergies agrees fairly well with our patterns 2 and 4 that are not signified by cortico-synergy coherence. Throughout the first year of development, the CNS undergoes many functional and structural reorganisations (Lacquaniti et al., 2012). Around the onset of independent walking, two additional synergies emerge, whose shape and spatial organisation largely correspond with our synergies 1 and 3. We consider the agreement(s) remarkable which lets us hypothesise that these two synergies emerge once the motor cortex and cortico-spinal tract are operational. Only then, the broadcasting of motor control commands from the cortex is properly developed to enable independent walking rather than ‘reflex-like’ muscle activation via synergies 2 and 4. If true, this organisation may have major implications for our understanding of motor development, in particular, and the interaction between cortex and spinal circuitries, in general.

Conclusion

Our findings show that the locomotor muscle synergies are represented in the sensorimotor cortex. These cortical signatures are synergy-specific and differ in synchronisation strength. With respect to timing of coupling during the gait cycle, the cortico-synergy connectivity is particularly evident at periods of double support. This indicates that the two muscle synergies that temporally align to these phases of the gait cycle receive higher cortical control than the other two synergies. Locomotor muscle synergies seemingly rely on the control of distinct neural circuitries.



Cortical contributions to locomotor primitives in toddlers and adults

The neural locomotor system strongly relies on spinal circuitries. Yet, the control of bipedal gait is accompanied by activity in motor cortex. In human gait control, the functional interaction between these cortical contributions and their spinal counterparts are largely elusive. We focused on four spinal activation patterns during walking and explored their cortical signatures in toddlers and adults. In both groups, cortico-spinal coherence analysis revealed activity in primary motor cortex to be closely related to two of the four spinal patterns. Their corresponding muscle synergies are known to develop around the onset of independent walking. By hypothesis, the cortex hence contributes to the emergence of these synergies. In contrast, the other two spinal patterns investigated here resembled those present during newborn stepping. As expected, they did not show any cortical involvement. Together our findings suggest a crucial role of motor cortex for independent walking in humans.



Adapted from: C.S. Zandvoort, A. Daffertshofer, & N. Dominici (in press). *Cortical contributions to locomotor primitives in toddlers and adults*. iScience. doi: [10.1016/j.isci.2022.105229](https://doi.org/10.1016/j.isci.2022.105229)

Introduction

Walking involves spinal networks that accommodate locomotor primitives (Dominici et al., 2011; Grillner, 1985, 2006; Ivanenko et al., 2013). In vertebrate models, the spinal networks have been identified as populations of premotor interneurons located in the lumbosacral spinal cord and are often considered central pattern generators (CPGs) (Giszter, 2015; Takei et al., 2017). Locomotor primitives (or muscle synergies) comprise small sets of functional units generating the motor output to coordinate muscles (Dominici et al., 2011). Each of the primitives reduces neural dimensionality by imposing fixed activation patterns on a set of muscles (d'Avella et al., 2003). The activation patterns appear at distinct timings throughout the step cycle as shown for both animals and humans (Dominici et al., 2011). While the representation of muscular patterns via synergies appears established (Dominici et al., 2011), it is unclear how they are organised across the human nervous system (Bizzi & Cheung, 2013).

In humans, deciphering the neural basis of muscle synergies is a challenge. It typically capitalises on nervous system manipulations or developmental courses (Cheung et al., 2020; Cheung & Seki, 2021; Dominici et al., 2011). Early locomotor development can be characterised by the preservation of congenital spinal patterns and superimposition of emerging patterns (Dominici et al., 2011; Sylos-Labini et al., 2020). In newborn stepping, two locomotor primitives/muscle synergies can be observed (Dominici et al., 2011), which alternately activate flexor and extensor muscles to move the legs (Thelen & Cooke, 1987). Constant time delays between the foot/ground contact and the activity of leg muscles imply immature neonate stepping to be driven by segmental reflex pathways (Forssberg, 1985). Similarities in stepping between typically developing and anencephalic infants further suggest that these neural circuitries are organised at or below the brainstem (Peiper, 1963). Cortical motor areas and cortico-spinal tracts around this age are immature as the motor system must still acquire most of its myelin (Yang & Gorassini, 2006). One may conjecture that the “hard-wired” neural circuitries governing locomotor primitives to be pattern generating networks that are separated from descending brain input.

Independent walking in toddlers coincides with the emergence of two additional muscle synergies on top of the two congenital ones of newborn stepping (Dominici et al., 2011). Along the aforementioned conjecture, these two sets with two synergies each are likely to rely on distinct phylogenetically neural systems (Forssberg, 1985). Expectably, the

new set emerges after necessary structural and functional re-organisations of intra-spinal, sensory and supra-spinal pathways (Forssberg, 1999). Regarding the latter synergy set, we here investigate the involvement of cortical motor networks. The motor cortex – much like the cortico-spinal tract – develops significantly over the first two years after birth (Eyre et al., 2000; Eyre et al., 1991; Huttenlocher, 1979), presumably caused by myelin build-up (Kinney et al., 1988).

Many mammals can walk without neural input from supra-spinal areas by capitalising solely on spinal CPGs (Forssberg et al., 1980; Grillner & Zangger, 1979), at least if obstacle avoidance is not required (Drew et al., 2008). In quadrupeds, four locomotor primitives can be generated throughout the gait cycle without supra-spinal input (Rossignol et al., 2006). All the four primitives remain largely intact in rodents that acquired a lesion during neonatal and adult phases (Yang et al., 2019). This is remarkable since cortical areas project to the midbrain, brainstem, and spinal cord – all these pathways appear evolutionary stable (Ocaña et al., 2015). In primates, however, interrupting pyramidal tracts or descending brain-stem pathways does yield impaired locomotion (Lawrence & Kuypers, 1968a, 1968b), arguably because there, the cortico-spinal tract does contain monosynaptic pyramidal projections to leg muscles (Lemon, 2008).



Bipedal locomotion involves motor centres in the brain (Nielsen, 2003). Especially human gait is irrevocably affected without input from supra-spinal motor projections (Capaday, 2002; Oudega & Perez, 2012) and a complete interference at the spinal cord will cause an inability to walk (Dimitrijevic et al., 1998). Intact supra-spinal areas and a (largely) complete cortico-spinal tract are hence prerequisite for self-sustained walking in humans.

We studied the involvement of the cortico-spinal tract in the control of human gait by focusing on four spinal motor patterns during locomotion (Dominici et al., 2011; Grillner, 1985, 2006; Ivanenko et al., 2013). We expected cortical activity to be not coherent with the two congenital locomotor synergies whereas it should be coherent with the two synergies that are known to emerge with independent walking in toddlers. As such, functional neural reorganisations including plasticity in both motor cortex and cortico-spinal tract may contribute to establishing these synergies.

Methods

Participants

All procedures were in full compliance with the Declaration of Helsinki for experiments involving humans. The local ethical committee of the Faculty of Behavioural and Movement Sciences Amsterdam (study protocols #VCWE-2016-082 and #VCWE-2020-006) approved the experimental procedures. Responsible researchers informed the adults and children's parents about the study procedures and asked them to provide written informed consent prior to inclusion into the study. Participants visited the BabyGaitLab laboratory of the Department of Human Movement Sciences at the Vrije Universiteit Amsterdam. For the toddler measurements, at least one parent or legal guardian was present during the experiments along with the responsible researchers. Our laboratory settings and experimental procedures were adapted to children so that any risk was equal or lower to that of walking at home.

Eighteen typically developing toddlers and adults were included in the study. Population characteristics of both groups can be found in Tables 4.1-4.2. A local child healthcare clinic qualified the toddlers (gestational age: 276 ± 8 days; mean \pm SD) as healthy: no neurological disorders, nor any significant health or developmental problems. Toddlers were selected based on their time since onset of unsupported walking and had 6.4 ± 1.0 months of independent walking experience when they visited the lab. We defined the first independent steps as the ability to perform four or more consecutive strides without the need for any physical support during walking and asked the parents to report this moment to us. We scheduled a recording session for each toddler around six months after the first independent steps to guarantee that all toddlers in the group had about the same walking experience. Adult subjects were recruited from a student pool and were awarded study credits for their educational curriculum. Exclusion criteria for the adult population were a self-reported history of neurological disorders.

Table 4.1. Characteristics of the typically developing (TD) toddlers and the number of analysed strides.

Toddlers

Participant	Gender	Age (months)	Weight (kg)	Height (cm)	Walking onset (months)	# strides
TD1	F	18.2	10.5	83	11.9	457
TD2	M	17.4	10.5	80	11.7	133
TD3	M	20.8	14.0	96	15.3	468
TD4	F	23.1	13.2	91	16.7	570
TD5	F	19.4	11.7	84	14.8	349
TD6	M	18.6	12.2	81	12.9	389
TD7	F	19.8	11.2	82	13.0	648
TD8	F	20.1	11.0	81	14.0	313
TD9	M	23.6	12.2	88	14.2	126
TD10	F	19.3	11.9	81	13.0	94
TD11	M	16.5	11.3	79	10.6	431
TD12	F	17.5	10.7	82	11.3	389
TD13	M	23.0	13.5	95	15.7	779
TD14	F	19.3	12.5	81	13.1	752
TD15	F	19.0	10.4	82	12.4	824
TD16	M	20.9	11.4	84	15.0	687
TD17	M	19.1	12.9	78	12.9	306
TD18	F	19.8	10.4	84	13.1	288
Mean±SD		19.7±2.0	11.8±1.1	84.0±5.2	13.4±1.6	447±225



Table 4.2. Characteristics of the adults (A) and the number of analysed strides.

Adults					
Participant	Gender	Age (years)	Weight (kg)	Height (cm)	# strides
A1	F	21	59.9	172	416
A2	F	19	77.6	177	386
A3	F	21	65.7	173	382
A4	M	22	67.9	171	415
A5	F	22	58.5	175	363
A6	F	20	79.9	174	458
A7	M	19	66.7	187	396
A8	M	18	68.0	189	422
A9	F	19	57.0	170	434
A10	F	19	65.3	174	396
A11	F	20	66.1	165	387
A12	F	19	61.0	164	396
A13	F	46	57.0	172	403
A14	F	19	54.0	173	569
A15	F	19	54.4	165	383
A16	F	18	51.0	164	376
A17	F	26	47.0	154	457
A18	M	25	61.0	178	433
Mean±SD		21.8±6.4	62.1±8.5	172.1±8.2	415±47

Experimental procedures. When entering the laboratory, toddlers got time to familiarise with the environment and researchers before starting the experiment. The experimental design consisted of over-ground and treadmill walking. Over-ground trials were conducted at a lab space with the dimensions of $\sim 5.5 \times 3.5$ m, where participants naturally walked barefoot from one side of the lab to the other side at their preferred speed. Treadmill trials were performed at a paediatric treadmill, specifically designed for subjects of lower ages and suitable for adults (N-Mill 60x150 cm, Motek Medical B.V., Amsterdam, the Netherlands). Treadmill speed in toddlers was chosen to elicit either supported or unsupported walking. Toddlers were encouraged to walk independent of any type of physical support. Either holding one or two hand(s), stabilising the trunk or some active body-weight support (i.e., physically supporting the body) was applied in case it helped to elicit continuous walking. Short walking trials (< 2 minutes) were intermitted by rest breaks in between. Adults walked at a self-selected comfortable walking speed in 30 over-ground and six treadmill trials. Toddlers and adults performed a total of 447 ± 225 and 415 ± 47 strides, respectively (Tables 4.1-4.2).



Data acquisition

Kinematics. A Vicon motion capture system (Vicon Vero v2.2, Oxford, UK), with 10 cameras placed around the walking path, sampled bilateral kinematic and video (Vue Vicon camera) data at 100 Hz. Twenty-three infrared reflective markers (diameter: 14 mm) were attached to the participant's body with adhesive tape. Here, we specifically focused on the markers attached to the bilateral lateral malleoli and fifth metatarso-phalangeal joint, and the bilateral heel marker in the adults' group. Electro-encephalography (EEG), electromyography (EMG), kinematics, and video feed were simultaneously acquired and synchronised.

Electromyography. Bipolar muscular activity was recorded of 20 to 24 muscles simultaneously (Figure 4.1). The complete set of 24 muscles consisted of the bilateral activity of the tibialis anterior (TA), gastrocnemius lateralis (GL), gastrocnemius medialis (GM), soleus (SOL), rectus femoris (RF), vastus lateralis (VL), vastus medialis (VM), biceps femoris (BF), semitendinosus (SEM), tensor fasciae latae (TFL), gluteus maximus (GLM), and erector spinae (ES). In preparation, the participant's skin was slightly rubbed with

alcohol at the locations where the electrodes were attached. Ag/AgCl electrode pairs for toddlers and adults (Mini Golden electrodes, Cometa, 15-mm-diameter electrodes, acquisition area of 4 mm²; and Medico, Ambu® Blue Sensor®, respectively) were attached to the skin over the muscle belly according to standard recommendations for minimising cross-talk between adjacent muscles (Hermens et al., 2000). In toddlers, movement artefacts were additionally minimised by fixating the electrodes and wireless EMG sensors to the thighs and shanks using elastic gauzes. EMG signals were recorded using two 16-channel wireless EMG systems (Wave Plus wireless EMG system with mini probes, Cometa, Bareggio, Italy). They were amplified with a gain of 1,000, and online band-pass filtered between 10 and 500 Hz before sampling at 1 kHz.

Electro-encephalography. Toddlers and adults wore a 32-channel and 64-channel EEG cap (WaveGuard™, ANT-Neuro, Enschede, the Netherlands; and TMSi REFA, TMSi Twente, the Netherlands, respectively) to record electrical cortical activity (Figure 4.1). For toddlers, the EEG cap was pre-gelled before mounting it on the head. After placement, with the help of a blunt plastic little stick we distributed the impedance gel (SonoGel, Bad Camberg, Germany) homogeneously and, if required, we injected additional gel to improve the impedance between the skin and electrode. In adults, the EEG cap was aligned to the fiducials. We injected impedance gel in every channel to lower the impedance. Toddler and adult nylon EEG caps with sintered electrodes were mounted in accordance with the international 10-20 system. EEG data were sampled at a frequency of 2,048 Hz (eego™ mylab, ANT B.V., Enschede, the Netherlands). Reference and ground electrodes were mounted on channel CPz and AFz, respectively. To compare the cortical activity of toddlers and adults, the 64-channel configuration of adults was reduced to match the 32 channels of toddlers.

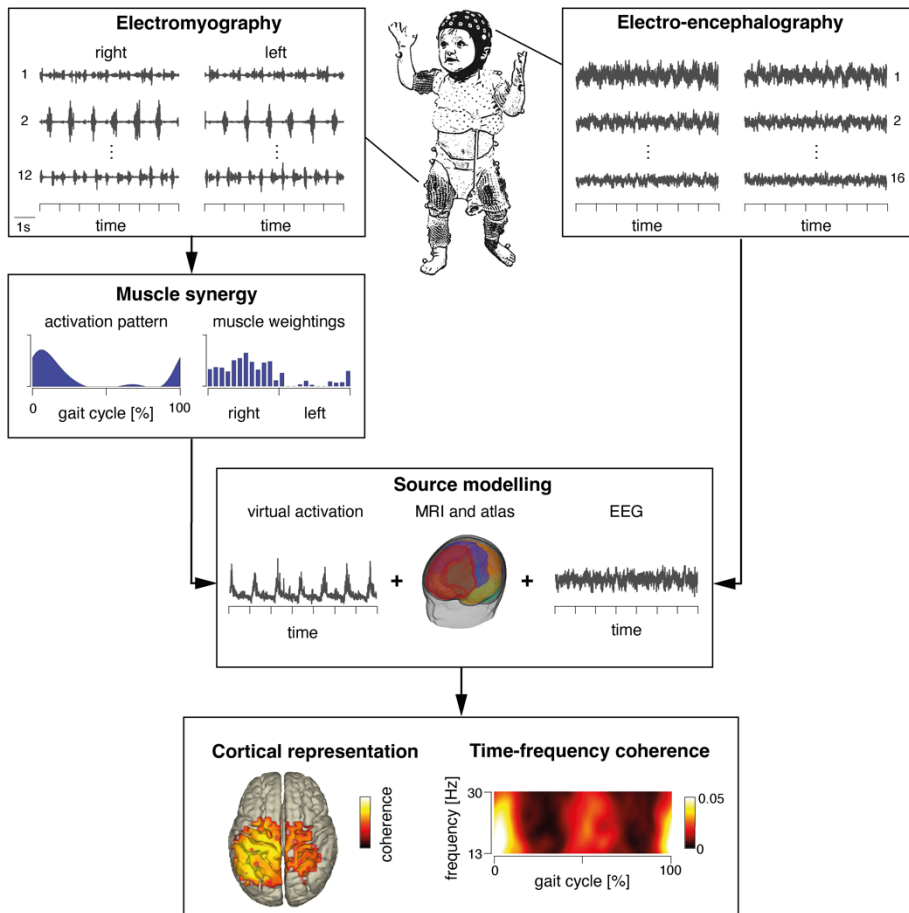


Figure 4.1 – Experimental and methodological workflow. We recorded 24-channel electromyography (EMG) and 32-channel electro-encephalography (EEG) during walking (top left and right, respectively). EMG signals of bilateral trunk and leg muscles were decomposed into muscle synergies (in dark blue an example of a temporal activation pattern and muscle weightings). Then both (EMG and muscle weightings) were exploited to estimate virtual activation patterns (see body text for more details). When source modelling, cortical coherence representations between the virtual activation patterns and EEG were localised using beamforming and age-specific anatomical MRIs. Signal reconstruction allowed for estimating coherence between synergies and primary motor cortex as a function of the gait cycle and frequency.

Data analysis

Kinematics and gait events. Foot-contact and foot-off events of adult participants were detected using a peak-detection algorithm based on the bilateral heel marker and its first-order derivative (Roerdink et al., 2008). In toddlers, gait events were determined from digital video recordings and marker trajectories using Vicon Nexus software (Vicon, Oxford, UK).

Gait events were independently assessed by at least two experienced researchers and confirmed with kinematic data. Events associated with gait initiation/termination and turning as well as non-locomotor movements (e.g., jumps) were discarded from further analysis. Here, we defined a complete stride (i.e., a gait cycle) from the moment the right foot first touched down until the next consecutive touch-down of the right foot.

Pre-processing and artefact removal electrophysiological data. EMG data were visually inspected to identify artefacts and to remove the corrupted data segments from further analysis. EMG time series were high-pass filtered at 30 Hz (bi-directional fourth-order Butterworth filter), and notch-filtered (bi-directional fourth-order Butterworth filter around $k \cdot 50$ Hz; $k=1, 2, 3, 4$). These filter parameters are commonly applied in muscle synergy analysis. EMG signals were full-wave rectified by taking the modulus of the analytic signal (Boonstra & Breakspear, 2012). Rectified EMG (\overline{EMG}) was then low-pass filtered at 5 Hz (bi-directional fourth-order Butterworth filter), since conventional muscle synergy techniques are primarily estimates of the envelope dynamics of the EMG.

Sensor-level EEG was pre-processed using custom scripts in MATLAB (ver. 2019a, Mathworks, Natick, USA) and the FieldTrip toolbox (www.fieldtriptoolbox.org/) (Oostenveld et al., 2011). Raw data were tested for outlier samples and interpolated via cubic splines. To test for outlier samples, values exceeding ten times the standard deviation of a channel after high-pass filtering were identified and subsequently corrected by cubic spline interpolation of the non-filtered data. Next, EEG time series were demeaned, bandpass- (bi-directional second-order Butterworth filter between 1 and 200 Hz) and notch-filtered (bi-directional first-order Butterworth filter around $k \cdot 50$ Hz; $k=1, 2, 3, 4$). Channels were checked for flat lines (smaller than 2^{-52} μ V) and excessive amplitudes. For the latter we used the following criteria: (1) a channel-specific standard deviation of three times higher than the mean standard deviation across channels, (2) a channel-specific maximal value of ten times higher than the mean or median maximal value of all channels and (3) a standard deviation of 100 times smaller than the mean standard deviation across channels. Artefact-sensitive channels were excluded, and their activity was spatially reconstructed using spherically spline interpolation based on available neighbouring channels. Single trials were discarded from further analysis when more than 10 channels were marked as artefact

sensitive. This led to the exclusion of 1.2% of the trials. An average of 1.5 ± 2.2 channels were considered as bad across all trials of all participants. After ‘bad’ channel detection, EEG time series were re-referenced to an average common reference. Data of every trial were subjected to an independent component analysis (ICA) using a fastICA-algorithm with online bias detection and random seed generator. The convergence parameter of the maximal number of iterations was set to 5,000. Criteria to consider modes as artefacts were a median frequency lower than 1 or higher than 100 Hz (movement and muscular artefacts, respectively). Mixing matrix components dominated by frontal channels (eye movements) were considered as eye-movement artefacts. Sensor-level EEG was reconstructed after discarding the artefact-sensitive modes from the mixing matrix. For our study population, 3.4 ± 4.0 components were discarded across all trials of all participants.



Muscle synergies. Envelope EMG time series were time and amplitude-normalised by resampling the epochs from two successive foot touch-down events of the right leg to 201 samples (Dominici et al., 2011) and normalising the amplitude to their Euclidian norm (Banks et al., 2017), respectively. Minima were subtracted from the normalised patterns (Figure S4.1). Non-negative matrix factorization (NNMF) decomposed the group average muscular envelopes (i.e., the average of all strides within the group) into muscle synergies. Generally, NNMF factorises multivariate EMG (dimensions: muscles \times time samples) into a low-dimensional set of non-negative modes, or more formally:

$$EMG = \sum_{i=1}^{N=4} P_i \cdot W_i + \epsilon \quad (4.1)$$

where the product of the temporal activation patterns (P ; time samples \times synergies) and their muscle weighting coefficients (W ; synergies \times muscles) of N synergies approximate EMG, the EMG envelopes; ϵ denotes the residual error. Factorisation parameters were set to 100 repetitions and 1,000 iterations. Termination parameters for residual size and relative change in P and W were set to 10^{-6} . NNMF-output was estimated based on multiplicative update and alternating least-squares algorithms (Berry et al., 2007), where P and W of the former

factorisation served as starting values for the latter factorisation. To determine the reconstruction accuracy of the extracted synergies, we computed the cumulative variance. In both group, four synergies were extracted to reproduce the EMG envelopes (Figure 4.2A-B and S4.1), accounting for 98.7% of variance of the mean patterns of toddlers and 91.5% of variance in adults.

Given a signal EMG, the NMF can be computed by minimising the Frobenius norm $\|EMG-(P \cdot W)\|_{\text{Fro}}$, which yields a set of weights W , with which one defines the virtual activation patterns P_{vir} as

$$P_{vir} = \widetilde{EMG} \cdot W^{-1} \quad (4.2)$$

Here W^{-1} denotes the Moore-Penrose inverse of W and \widetilde{EMG} the EMG time series before low-pass filtering – note that we used the dot notation to indicate the mere matrix multiplication. The virtual activation patterns adequately represent the waveshapes of the basic activation patterns P including high-frequency components. Virtual activation patterns were included in the coherence analyses with the EEG (Zandvoort et al., 2021; Zandvoort et al., 2019).

We would like to note that in contrast to the original signals EMG the virtual activation patterns P_{vir} should not be considered rectified EMGs, since for $|\epsilon|>0$ the rank-reduction in Eq. 4.1 may yield $P_{vir}<0$. We did encounter negative samples (see Table S4.2) rendering this note important. By the same token, however, we can stress that P_{vir} closely resembled P ; correlating P_{vir} and P revealed correlation coefficients between 0.95 and 0.99.

Source modelling models. To localise cortical sources that exhibit coherence with the muscle synergies (i.e., virtual activation patterns), we applied a source modelling approach called beamforming. Using such algorithms, the inverse problem (i.e., not knowing where brain activity originates from) can be solved. First, we created a forward model comprising a volume conduction, source, and electrode model. Realistic five-layer head models were constructed using age-specific structural MRIs from the Neurodevelopmental MRI Database (Richards et al., 2016; Sanchez et al., 2012). We selected averaged MRIs from the database

that were close to the average age of the toddler and adult population, which were 18 months and 20-24 years, respectively (Richards et al., 2016; Sanchez et al., 2012). White matter, grey matter, and cerebral spinal fluid segments were created from probabilistic tissue maps. Scalp and skull segments were modelled at the outer voxels of the inner-skull tissue maps. The five segmented tissues were meshed into hexahedrons. A realistically shaped five-shell volume conduction model was constructed from the meshed tissue volumes using the SIMBIO-software. Conductivity values of the isotropic compartments were set to 0.43 (scalp), 0.01 (skull), 1.79 (cerebral spinal fluid), 0.33 (grey), and 0.14 (white) Siemens/meter (O'Reilly et al., 2021). The grey segment of the volume conduction model was discretised into a three-dimensional grid of 5 mm³ (i.e., source model). We used an inward shift of 15 mm from the scalp. An age-matched template electrode model was (non-)linearly warped onto the outer surface of the head model so that the distances between electrodes and scalp were minimised. Forward solutions by means of lead fields were estimated using the volume conduction model, source model, and three-dimensional sensor positions. Lead-field matrices uniquely solve the forward problem and describe the propagation of the electrical activity from cortical dipoles to the sensors in three orthogonal directions.



Cortical source localisation and reconstruction. Dynamic Imaging of Coherent Sources (DICS) beamformers were estimated to localise the cortico-synergy coherence between the EEG channels and muscle synergies (Gross et al., 2001). Spatial filters of DICS-beamformers were optimised by maximising the coherence between the sensor-level EEG and virtual activation patterns. That is, the cross-spectral density matrices of the EEG were extended by employing the virtual activation patterns as reference channel. Generally, coherence describes phase locking at iso-frequencies between two signals while being weighted by the signals' power and is defined as:

$$C_{xy}(\omega) = \frac{|\langle |S_x(\omega)S_y(\omega)| e^{i(\phi_x(\omega) - \phi_y(\omega))} \rangle|^2}{\langle |S_x(\omega)|^2 \rangle \langle |S_y(\omega)|^2 \rangle} \quad (4.3)$$

where $C_{xy}(\omega)$ denotes the squared coherence as a function of frequency, $\langle \cdot \rangle$ the expectation value, and S the Fourier-transform of the signals x and y .

We specifically targeted the beta-frequency band (13-30 Hz) as coherence comprising sensor-level EEG yields highest coherence magnitudes at this frequency range. To estimate coherence beamformers, we first resampled the virtual activation patterns to 2,048 Hz so that it matched the EEG's sampling rate. Both EEG data and virtual activation patterns were down sampled to 256 Hz for computational reasons. Resampled time series of sensor-level EEG and virtual activation patterns were spectrally transformed using short-time Fourier transforms and Slepian sequences of 200ms. The frequency of 21.5 Hz was selected as centre frequency and spectral smoothing was set to 8.5 Hz. These temporal and spectral parameters resulted in Slepian sequences with two tapers. From the Fourier-transformed data, we estimated the cross- and auto-spectra for all strides available. Cross- and auto-spectra were averaged over the time and frequency dimension for every stride. From all strides available for every subject, we took the median spectra to obtain subject-specific estimates. Beamformers were constrained to be real valued to avoid phase shifts between channels. Phase shifts would violate the assumption of linear transformations between sensors and sources (Westner et al., 2022). The orientation of dipoles did not have to be fixed so that moments were obtained in the three orthogonal directions. Note that after the application of principal component analysis during source reconstruction only the strongest moment was retained. The regularisation parameter of the cross-spectral density matrix was set to 5%. We chose this value as a trade-off between the signal-to-noise ratio and spatial precision (Woolrich et al., 2011). Adding (a percentage of) mean sensor power to the diagonal of the cross-spectrum matrix will effectively broaden the passband and, hence, increases the filter's signal-to-noise ratio (Brookes et al., 2008); by the same token, however, regularisation will result in blurring of the output volumes.

Cluster-based permutation tests were employed to assess the coherence-based beamformers. The advantage of cluster-based permutation testing is that it does not require any assumptions about probability density functions (Maris & Oostenveld, 2007). Rather, their probability density functions are estimated by permuting the representations for several partitions by Monte Carlo estimations. Using permutation testing, one can also reduce the number of multiple comparisons. Permutation testing accomplishes this by thresholding based on clusters from neighbouring samples rather than individual samples. This involves

grouping test statistics of adjacent samples that exceed a certain predefined α -level. Clusters that exceed the α -level are considered significant (Nichols & Holmes, 2002). For the within-subject statistics, we iteratively performed permutation testing for each synergy (synergies 1-4) and group (toddlers and adults). We considered the subject-specific beamformer volumes that were computed over the entire gait cycle. We performed a one-sample t-test on these volumes for the contrast ‘coherence minus subject-specific mean coherence > 0 ’. To do so, we first normalised individual coherence volumes by subtracting the mean coherence over all voxels from the subject-specific volumes. We note that the mean subtraction is equivalent to contrasting the coherence volumes without mean subtraction against their own mean. This entails that our statistical volumes do not reflect the absolute coherence strength, and that significant clusters are indicative of higher spatial coherence relative to all other voxels. After mean subtraction, coherence values are bounded between -1 and 1. To stabilise its variance, we applied a Fisher transform via the inverse hyperbolic tangents (i.e., $\text{atanh}(\text{coh})$) function. In permutation testing, clusters were considered significant based on the intensity and size of the clusters. This can be realised via the weighted cluster mass (Hayasaka & Nichols, 2004; Maris & Oostenveld, 2007). The weighted cluster mass is sensitive to both amplitude of the test statistic and number of grid points. Permutation testing was performed with 4,096 randomisations and (cluster-) alpha of 0.005. The source localisation volumes, as presented in Figure 4.2, are the result of power and cross-spectral averages over the entire gait cycle (from right-to-right foot contact).



Effect of side gait cycle events on cortical coherence sources. To ensure that the cortical grouping of the muscle synergies is not simply the result of our time-locking procedure (Figures S4.2-S4.3), we again performed the source analysis by time locking from left-to-left foot contact. The cortical coherence sources defined from left-to-left foot contact were similar to those obtained with time locking from right-to-right foot contact (Figures S4.4-S4.7). That is, synergies 1 and 3 resembled significant beta-band coherence with the motor cortex whereas synergies 2 and 4 did not. Again, the observed coherence was found in both toddlers and adults.

Moreover, the coherence sources turned out to be lateralised for some of the synergies. The left hemisphere seems to be more dominantly involved as it resembled highest

beta-band coherence for synergies 1 and 3 (Table S4.1). This lateralisation was evident in toddlers and adults and was independent of the time-lock event (Figures S4.2-S4.7).

Development changes of the cortical representations. To test for between-group, developmental differences, we compared the toddlers' volumes against adults. The beamformer volumes of toddlers and adults did have different geometry, hampering valid statistical comparisons between groups. Hence, we first spatially normalised the three-dimensional coherence images (Ashburner & Friston, 2005; Friston et al., 1994). To estimate the optimal normalisation parameters, we set the bias regularisation and full-width half maximum (FWHM) to 0.0001 (very light) and 60 mm, the regularisation parameters to [0 0.001 0.5 0.05 0.2], the fudge factor smoothing to 5 mm and the sampling distance for the estimation of modelling parameters to 2. Warped volumes were interpolated using a nearest neighbouring approach. Additionally, the warped toddler and original adult volumes were smoothed with a FWHM of 1 voxel. Like the within-group statistics, source data were mean-subtracted, and $\tilde{c} = \text{atanh}(\text{coh})$. Resulting volumes were subjected to two-tailed independent t-tests using permutation testing to statistically assess the toddler-adult contrast (Figure 4.2C).

In line with the within-subject beamformer findings of the main text, significance was only found for synergies 1 and 3 in the between-group statistics (Figures S4.8-S4.10). For these synergies, mean coherence differences were both positive and negative for toddlers and adults. Positive significant clusters (toddlers > adults) were mainly found in the postcentral and parietal gyri. Negative significant clusters (toddlers < adults) were localised more frontal. Note that the locations of both cluster types are in line with the within-subject statistics.

Source reconstruction. To obtain reconstructed activity at the cortex, sensor-level EEG data were filtered to reconstruct the time series at the regions of interests (ROIs). ROIs were selected from the LONI Probabilistic Brain Atlas (LPBA-40) (Fillmore, Richards, et al., 2015). Here, we selected the linear filters at a 5-mm circle around the voxel that exhibited maximal coherence as found within the precentral and postcentral gyri. After source reconstruction, we only kept the source time series comprising the maximal dipole moment.

We took the first principal component from the three orthogonal dipole directions. The time series comprising the maximal dipole moment were considered for the estimation of the time-dependent cortico-synergy coherence.

Time-frequency cortico-synergy coherence. Auto- and cross-spectra as a function of time and frequency were obtained from source-reconstructed EEG and virtual activation patterns of entire walking trials. Auto- and cross-spectra were obtained with short-time Fourier transforms with Hanning windows of 200ms. These spectra were epoched from right-to-right foot contact and time-warped from 0 to 100% of the gait cycle. Spectra were averaged across all strides available for every subject. We computed coherence sample estimates according to Eq. 4.3.

Both toddlers and adults exhibit modulation of beta-band coherence between motor cortex and synergies 1 and 3 throughout the gait cycle. Coherence is maximal around double support phases (Figure 4.3). To test for developmental changes, we then compared the beta-band coherence of toddlers and adults. To evaluate coherence changes as a function of time and frequency between toddlers and adults, we performed permutation testing on the time-frequency-coherence representations. We employed an independent t-test to evaluate the mean coherences of toddlers and adults. Number of randomisations was set to 8,196 with an alpha-level of 0.01 and a cluster-alpha of 0.01. Again, significance of clusters was assessed by the weighted cluster mass (Hayasaka & Nichols, 2004; Maris & Oostenveld, 2007).

We further studied the time-frequency coherence involving the left and right primary sensory cortices. For primary sensory cortex, the coherence patterns with synergies 1 and 3 modulated similarly to the coherences with the primary motor cortex (Figures S4.11-S4.12). The sensory cortex yielded more pronounced clusters when comparing toddlers and adults than the motor cortex (lower rows of Figures S4.11-S4.12). These toddler-adult differences between the motor and sensory cortex agrees with the muscle synergy representations at the cortex as presented in the main text (Figure 4.2). The cortical representations in adults were localised more frontally than the ones in toddlers. While adult sources were limited to the primary and supplementary areas of the motor cortex, the primary sensory cortex was also significant in toddlers for synergies 1 and 3. Also, to exclude effects on hemisphere selection we contrasted the time-frequency representations of left and right



hemisphere from the primary motor and sensory areas in toddlers and adults. Findings revealed that there are no significant clusters when contrasting these time-frequency coherence representations of the right and left hemisphere.

To show that the observed coherence patterns were not a mere by-product of gait-cycle dependent power modulations, we estimated the event-related amplitude modulation in primary sensorimotor cortex and synergies 1 to 4 (Figure S4.13). The amplitudes of the cortical and synergy activity modulated as a function of the gait cycle. The cortical activity showed event-related beta-band (de-)synchronisation locked to double and single support phases. Likewise, the beta-band amplitude of the virtual activation patterns was temporally aligned to the temporal patterns of the synergies. For the coherence patterns involving synergies 1 and 3 this means that the maximal coherence as observed during the double support phases did not emerge due to low power from the primary motor cortex and/or synergies.

Results

To test for the hypothesised segregation of locomotor primitives into those with and without sole sub-cortical organisation and the maturation of the latter, we analysed correlative neural outputs from the cortex and the muscles that we recorded using non-invasive electrophysiological modalities during walking. We studied two groups – toddlers and adults – in which all four primitives were established (Tables 4.1-4.2) (Dominici et al., 2011). In both groups, we co-registered EEG and EMG activity of trunk and leg muscles (Figure 4.1). Cortical muscle synergy signatures were assessed by combining conventional muscle synergy and coherence-based source modelling analyses (d'Avella et al., 2003; Gross et al., 2001). In brief, cortico-synergy coherence served as a measure of long-distance phase locking between cortical areas and muscle synergies (Zandvoort et al., 2021; Zandvoort et al., 2019). We specifically targeted neural synchronisation of the cortico-spinal drive in the beta-frequency band (13-30 Hz) as these oscillations are known to contribute to cortical control of voluntary movements (Baker, 2007; Engel & Fries, 2010; Kilner et al., 2000), locomotion (Roeder et al., 2018), and postural control (Zandvoort et al., 2019).

Muscle synergies and coherence-based beamformers. For the synergy assessments we relied on the linear decomposition of muscular activation profiles through non-negative matrix factorization (Figure S4.1). Both toddlers and adults displayed four locomotor primitives (Figure 4.2A-B). Synergy patterns 1 and 3 were mainly active during double support phases, seemingly involved in the touch-down and lift-off of the legs. Synergy patterns 2 and 4 occurred during single support phases contributing to forward propulsion and swinging the legs. The temporal shapes of synergies 1 and 3 largely corresponded to the supplementary primitives reported in earlier work, and the ones for synergies 2 and 4 were comparable to the congenital primitives (Dominici et al., 2011). The cortical sensorimotor, supplementary motor, and premotor areas displayed significant beta-band coherence sources for synergies 1 and 3 (Figures 4.2A-B and S4.2-S4.7). Cortical sources were absent for synergies 2 and 4. That is, only two out of four muscle synergies displayed significant cortical representations and that was evident in both toddlers and adults. Yet, the beta-band coherences appeared more posterior for toddlers compared to adults (Figure 4.2A-B). Beta-band coherences of synergies 1 and 3 showed a significant increase and decrease in premotor areas and somatosensory areas, respectively, suggesting further development and maturation from toddlers to adults (Figures 4.2C and S4.8-S4.10).



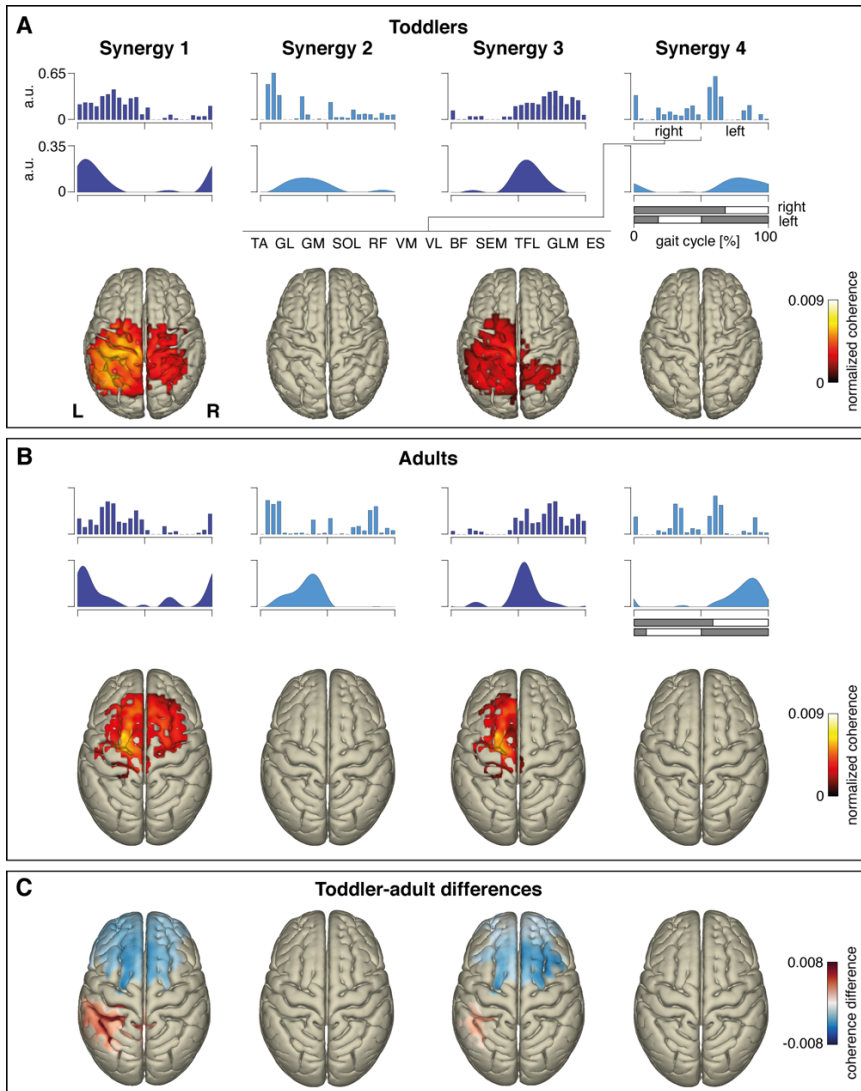


Figure 4.2 – Muscle synergies and their cortical coherence representations for (A) toddlers, (B) adults and (C) toddler-adult differences. (A-B) Blue-coloured bars and areas show ensemble-averaged muscle weightings and activation patterns. The latter are time locked from right-to-right foot contact (percentage of the gait cycle). TA, tibialis anterior; GL, gastrocnemius lateralis; GM, gastrocnemius medialis; SOL, soleus; RF, rectus femoris; VM, vastus medialis; VL, vastus lateralis; BF, biceps femoris; SEM, semitendinosus; TFL, tensor fasciae latae; GLM, gluteus maximus; ES, erector spinae. Dark and light blue colours refer to the group of synergies 1 and 3, and synergies 2 and 4, respectively. Reconstructed coherence representations between electro-encephalography and muscle synergies are projected onto age-matched cortical surfaces. Coloured parts on these surfaces correspond to the significant voxels determined via one-sided, intra-group t-tests ($p < 0.005$; see Figure S4.3 for the statistical assessments) and indicate areas of the cerebral cortex at which coherence exceeds the individual subjects' means. (C) Cortical surfaces demonstrated significant mean coherence differences as obtained by the inter-group independent t-tests, i.e., contrasting toddlers versus adults. Positive and negative values, hence, correspond to “toddlers > adults” and “toddlers < adults” ($p < 0.025$; see Figure S4.9 for the statistical assessments). L: left; R: right.

Time-frequency coherence. The time-resolved beta-band coherence between the source-reconstructed activity of primary motor areas and synergy patterns 1 and 3 was maximal during double support phases (Figures 4.3 and S4.11-S4.12)¹, i.e., when the peak amplitude of the synergy patterns can be observed (Figure 4.2A-B). This reveals that coherence and synergy patterns were temporally aligned. Such a time locking can also be established between the beta-power modulation and virtual activation patterns (Figure S4.13). Coherence at double support phases is also evident for the cortico-muscular coherence estimates (Figure S4.14). Around the double support phase, the coherences involving synergies 1 and 3 appeared higher in the toddlers than in the adults, indicating that coherent epochs became more focal in time in the adults. For synergy 1, this was significant after the right heel contact, for synergy 3 after the left one (see Figure 4.3, right panels). They differed between groups in that coherence epochs became more focal in the adults. That is, while beta-band coherence is already present in toddlers, the cortico-spinal pathways carrying beta-band oscillations mature until adulthood (Figure 4.3).

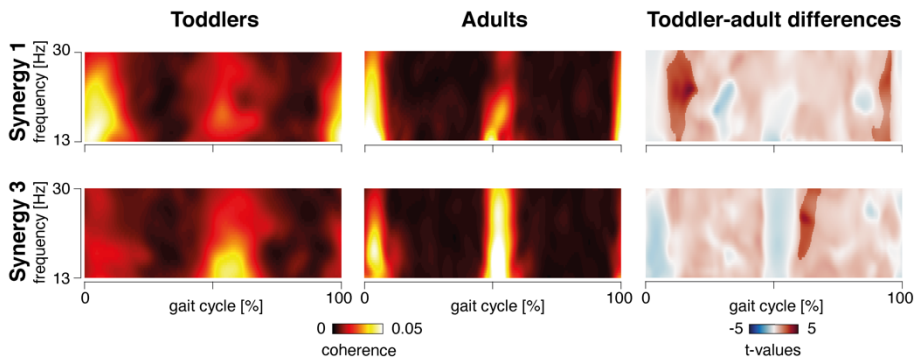


Figure 4.3 – Time-frequency magnitude-squared coherence between the primary motor cortex and synergies 1 and 3 for toddlers and adults. The gait cycle is defined from right-to-right foot contact. Time-frequency coherences are pooled over participants for every synergy pattern and group. For the toddler-adult differences, time-frequency statistics were estimated with cluster-based permutation tests using independent t-tests. Non-transparent colours correspond to statistically significant clusters. The positive t-values mean higher coherence for toddlers compared to adults.

¹ We here present time-frequency coherence of the bilateral primary motor areas as cortico-synergy coherence turned out to be independent of hemisphere (Figures S4.11-S4.12).

Discussion

The cortical representations and time-dependent coherences reported here provide first support that in humans two locomotor primitives relate to cortical areas. We translated these findings into a schematic shown in Figure 4.4, where we highlighted the cortex-dependent motor primitives by discarding any additional neural circuitries related to, e.g., cerebellum, thalamus, and basal ganglia (Berger et al., 2020; Cheung et al., 2020; Forssberg, 1985) for their contribution to the control of motor primitives.

We found synergies 1 and 3 to be represented in motor network activity both in toddlers and adults. The corresponding cortico-synergy coherence was most pronounced during the double support phases. This particularly applies to oscillatory activity in the beta-frequency band that seemingly propagates along the cortico-spinal tract to neuronal layers in the spinal cord (Baker, 2007). Its presence around the double support phases suggests cortical control of (dorsiflexor) leg muscles involved in the touchdown of the foot. Neonatal stepping typically does not display a clear touchdown and – remarkably – this age group lacks synergies 1 and 3. Like quadrupeds, neonates touch the ground with their forefoot after which they lower their ankle through dorsiflexion, indicating a lack of ankle control (Forssberg, 1985). Here, we note that leg muscle activity can be suppressed before foot contact by stimulating the motor cortex (Petersen et al., 2001). In any case, our findings hint at an important role of motor cortex in the activation of the lower leg muscles around foot contact. By contrast, synergies 2 and 4 seem to utilise sub-cortical structures for control, e.g., deeper cerebellar, brainstem, and spinal networks. They were not fostered by cortical networks and may stem from pattern generators that are (largely) independent of cortical input.

Cortical signatures of synergies 1 and 3 develop further from toddlers to adults (Figures 4.2C and 4.3). In the cerebral cortex, the muscle synergy signatures seem to shift from the primary somatosensory and motor areas in toddlers to premotor areas in adults (Figure 4.2C). In the early stages of walking development, they may therefore reflect sensory rather than motor processes. Recall that synergies 1 and 3 were primarily active during double support phases, when both legs are in contact with the ground calling for balance control via tangential forces decelerating and accelerating the body (Dominici et al., 2011). Around the double support phases, cortico-synergy coherence becomes more focal in time in the adults in agreement with earlier findings on synergy and muscular activation patterns (Dominici et al., 2011; Ivanenko et al., 2013).

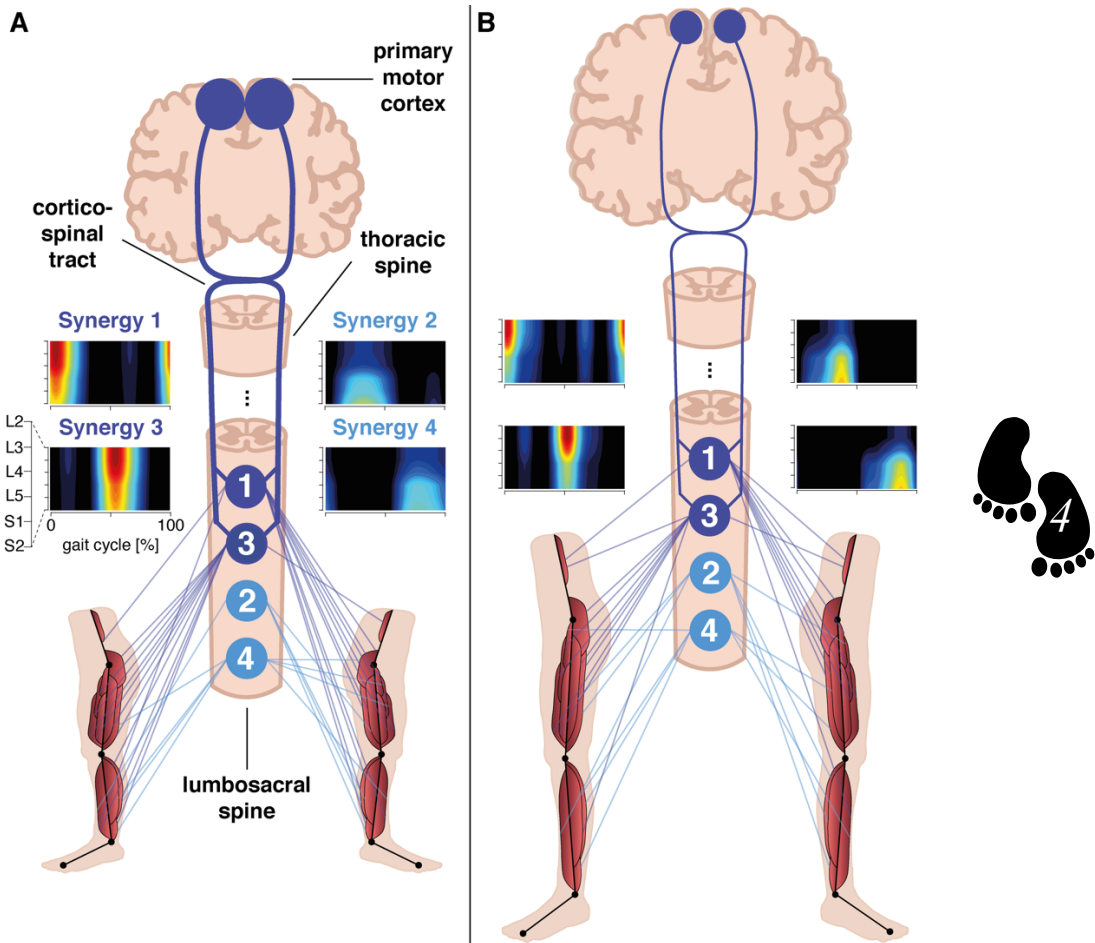


Figure 4.4 – Conceptualisation of how muscle synergies relate to activity in the primary motor cortex in (A) toddlers and (B) adults. The four locomotor primitives are represented at the lumbosacral spinal cord as pinpointed by the spinal maps (i.e., spatiotemporal reconstructions of synergy activity at the spinal cord) ranging from segments L2 to S2. Spinal maps estimated the alpha-motoneuron activity of synergies 1-4 for toddlers and adults by using weighted muscle innervations representative for the spinal cord (Ivanenko et al., 2006). As confirmed by the spinal maps, synergies 1 and 3 are accommodated more lumbar in the spinal cord compared to synergies 2 and 4. Every synergy co-activates multiple muscles with a specific weight (dark and light blue lines from the 1 to 4 synergies to the corresponding muscles – muscle weightings > 0.15). The two dark-blue synergies – circles “1” and “3” – reveal phase-locking with oscillations in motor areas. This, however, does not necessarily mean that these synergies solely rely on activities in motor cortex. Yet, from our findings, we can only infer cortico-spinal interactions. Admittedly, this gross schematic lacks lots of detail, e.g., the involvement of cerebellum and deeper cerebellar nuclei like thalamus and basal ganglia (Berger et al., 2020; Cheung and Seki, 2021; Forssberg, 1985). No cortico-spinal pathways appear in the two light-blue synergies – circles “2” and “4” – which must be regulated by sub-cortical circuitries. The bigger cortical sources and thicker cortico-spinal tract in toddlers indicate stronger coherence between synergies and primary motor cortex (Figure 4.2C), and broader beta-band bursts in the time-frequency coherence (Figure 4.3), respectively.

In mammals, the spinal cord contains autonomously regulated networks that solely suffice to control alternating extensor-flexor activation of the limbs (Forssberg et al., 1980). There, repetitive rhythmic locomotor behaviour may be evoked by local injections of neurochemical substances in spinally transected quadrupeds (Grillner & Zangger, 1979). This leads to locomotor primitives that are similar for spinal and healthy mammals (Desrochers et al., 2019). These networks closely resemble CPGs (McCrea & Rybak, 2008). While “[s]tudies of the neural control of animal locomotion certainly provide an important basis for such work on human walking...[one] should not expect that the results would inevitably be comparable. Decerebrate animals do not have the full gamut of descending inputs, and spinalised preparations have none” (Capaday, 2002). The motor cortex has a privileged role in humans compared to other mammals as any interference of its downwards projections results in locomotor deficits in humans. Our non-invasive assessment of cortico-synergy coherence allows for disentangling the organisation of the locomotor primitives and for separating cortical and sub-cortical processes that possibly underly the formation of muscle synergies. As we showed, it may serve to quantify cortical involvement in distinct primitives.

In humans, restoring walking capability after spinal lesions has been nearly impossible until recently (Wagner et al., 2018). In motor-complete spinal cord injury subjects, alternating locomotor-like movements together with rhythmic muscular activity can be evoked by stimulating the spinal cord at frequencies within the beta-frequency range (13-30 Hz) (Danner et al., 2015; Dimitrijevic et al., 1998). Arguably, the neural loops comprising beta-band synchrony are key components in the pattern-generating capacity within the spinal cord.

The two locomotor primitives associated with the motor cortex closely resemble those developing when toddlers start to walk independently (Dominici et al., 2011). To pinpoint these developments in more detail, longitudinal studies are needed. They may shed light on the differential neural organisation of the muscle synergies. In view of our current cross-sectional assessments, we expect starting to walk independently to coincide with the emergence of the supplementary synergies and the accompanying cortico-synergy coupling.

Limitations of the study

The present study found that the motor cortex predominantly interacts with two muscle synergies. Here, the strength of coupling between the motor cortex and these muscle synergies was assessed through cortico-synergy coherence. In neurophysiological sense, it is thought that such cortico-spinal coherence particularly reflects neural processes along the cortico-spinal tract operating at isolated frequencies. This means that neural processes cannot be captured in case the spectral interactions do not occur linearly. In that sense, it would be interesting to re-assess cortico-synergy coupling by examining cross-frequency measures to see if the functional coupling between the cortical areas and two muscle synergies with double support phase patterns persists.



Supplementary material Chapter 4

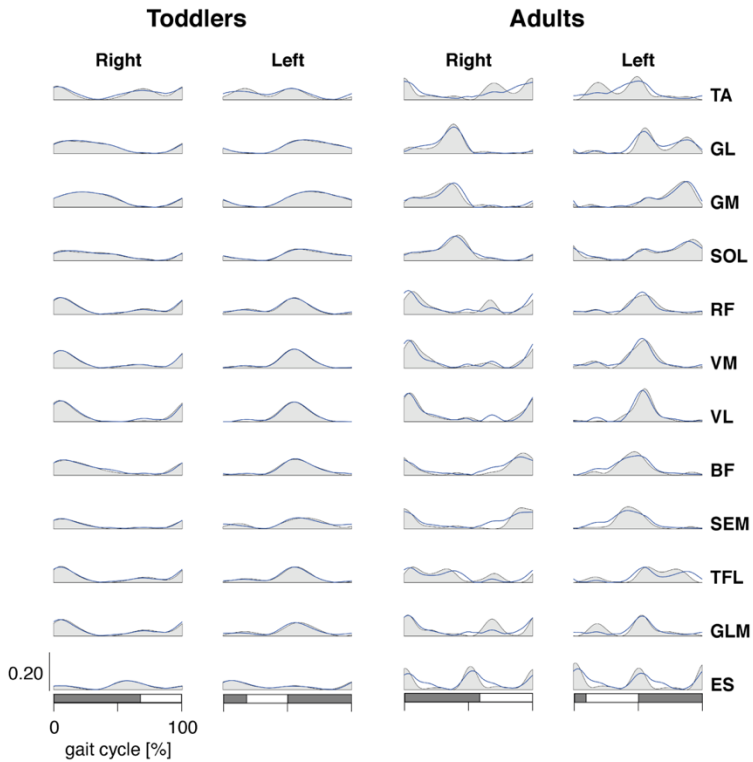


Figure S4.1 – Bilateral muscular activation patterns of toddlers and adults. Patterns represent ensemble averages for both groups and are amplitude-normalised (i.e., EMG envelopes divided by their norm over time) and time-locked from right-to-right foot contact (percentage of the gait cycle). Thin blue graphs depict reconstructed EMG-activity based on the inner product of the basic activation patterns and muscle weightings. TA, tibialis anterior; GL, gastrocnemius lateralis; GM, gastrocnemius medialis; SOL, soleus; RF, rectus femoris; VM, vastus medialis; VL, vastus lateralis; BF, biceps femoris; SEM, semitendinosus; TFL, tensor fasciae latae; GLM, gluteus maximus; ES, erector spinae. Horizontal bars below represent average stance (grey) and swing phases (white).

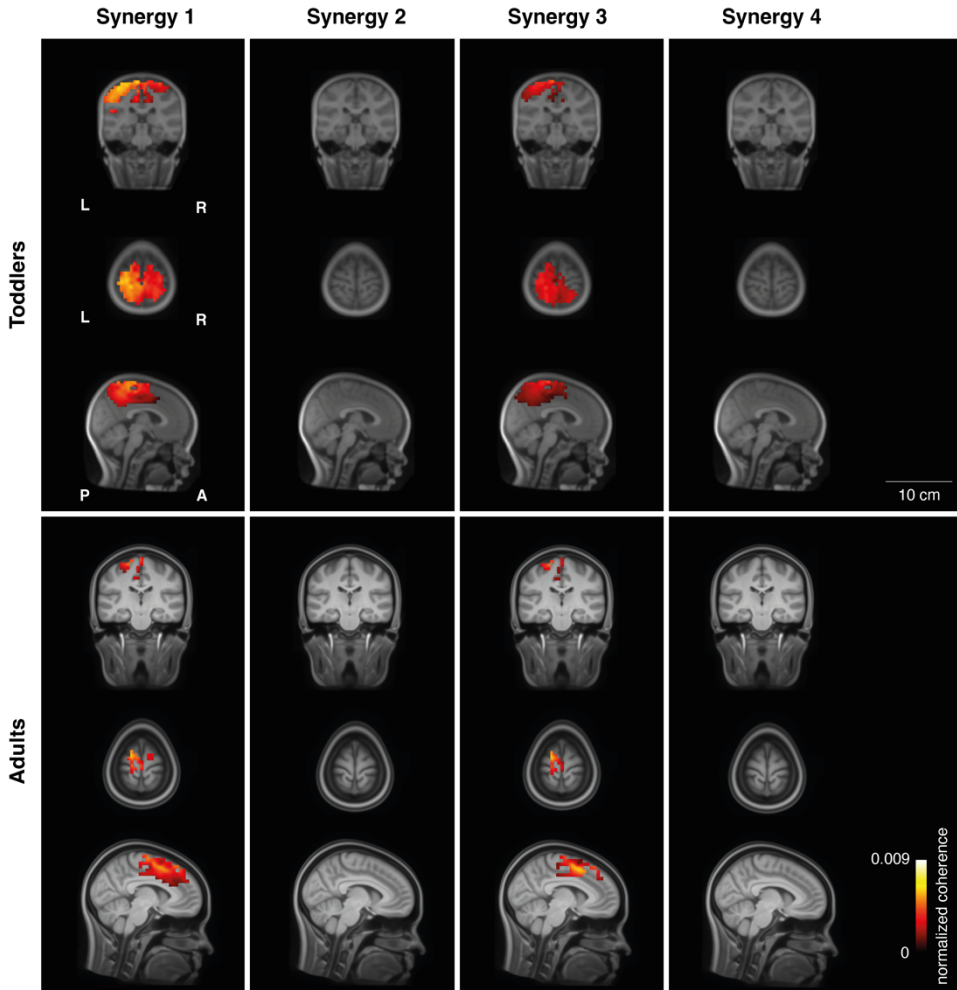


Figure S4.2 – Cortical beta-band coherence representations projected on age-matched MRIs for toddlers (top) and adults (bottom) over the gait cycle computed from right-to-right foot contact. Coherence sources are like those presented in Figure 4.2 of the main text. The coloured dimension represents the coherence voxels that significantly exceeded the subject's mean coherence. Coloured sources are masked by the voxels that turned out significant from one-sided t-testing ($p < 0.005$; Figure S4.3). L: left; R: right; P: posterior; A: anterior.

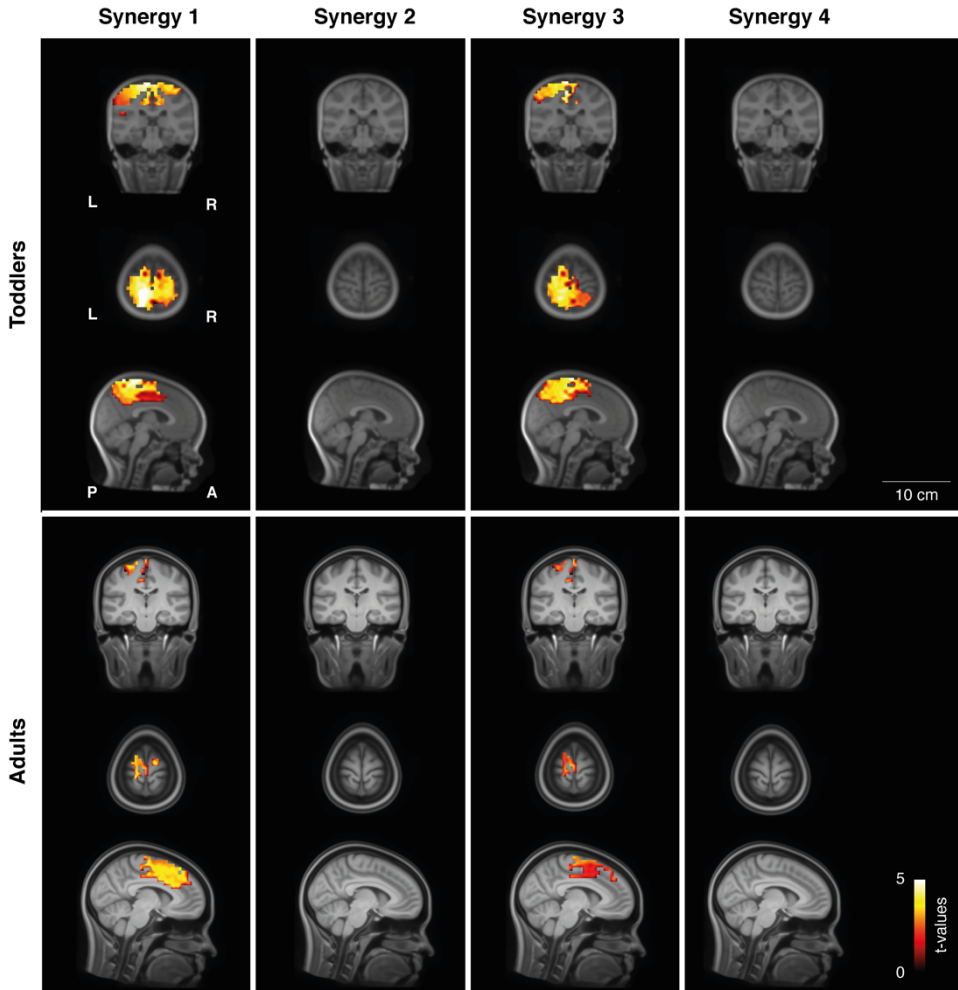


Figure S4.3 – Statistical coherence representations for toddlers (top) and adults (bottom) over the gait cycle computed from right-to-right foot contact. Cortical beta-band volumes were subjected to one-sided t-tests for the contrast ‘coherence minus subject-specific mean coherence > 0’ ($p < 0.005$). Significant sources for these contrasts are projected onto age-matched template MRIs. L: left; R: right; P: posterior; A: anterior.

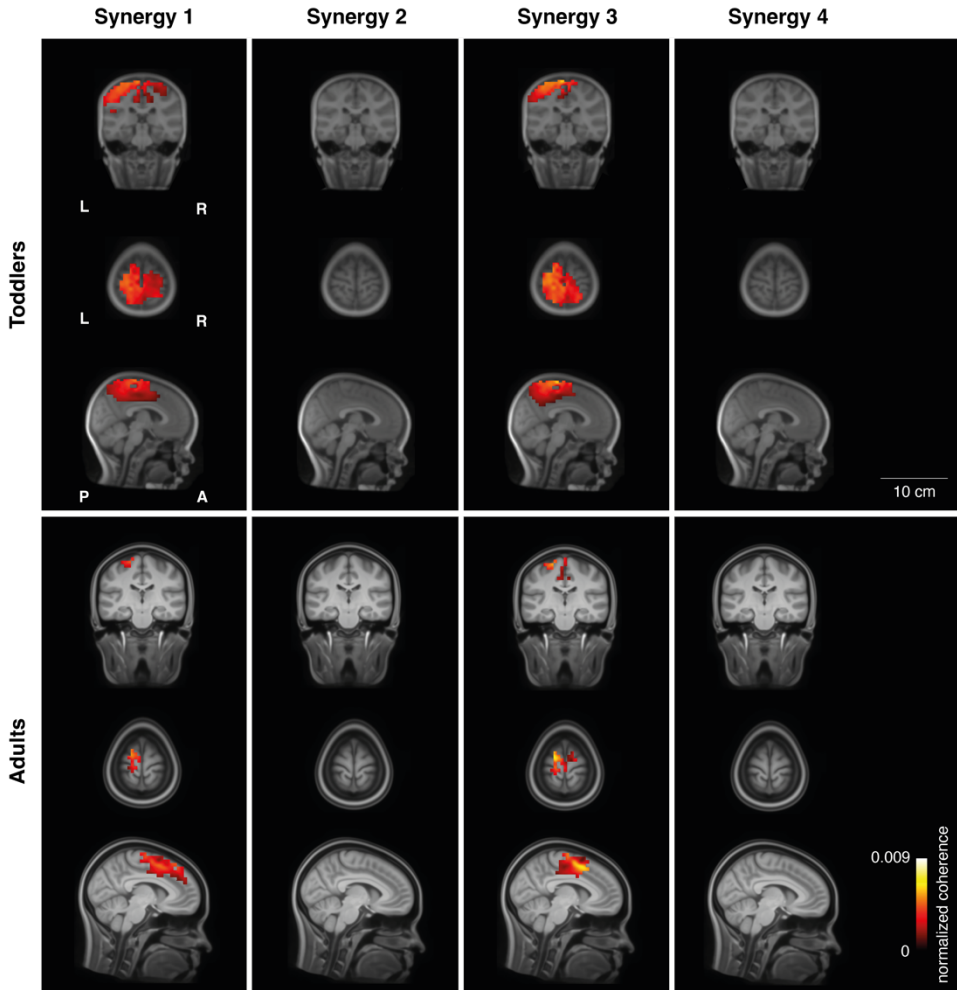


Figure S4.5 – Beta-band coherence representations for toddlers (top) and adults (bottom) when source reconstruction is applied from left-to-left foot contact. Sources are identical to those presented in Figure S4.4. Cortical volumes are masked by the voxels that were significant when testing the contrast ‘coherence minus subject-specific mean coherence > 0’ ($p < 0.005$; Figure S4.6). L: left; R: right; P: posterior; A: anterior.

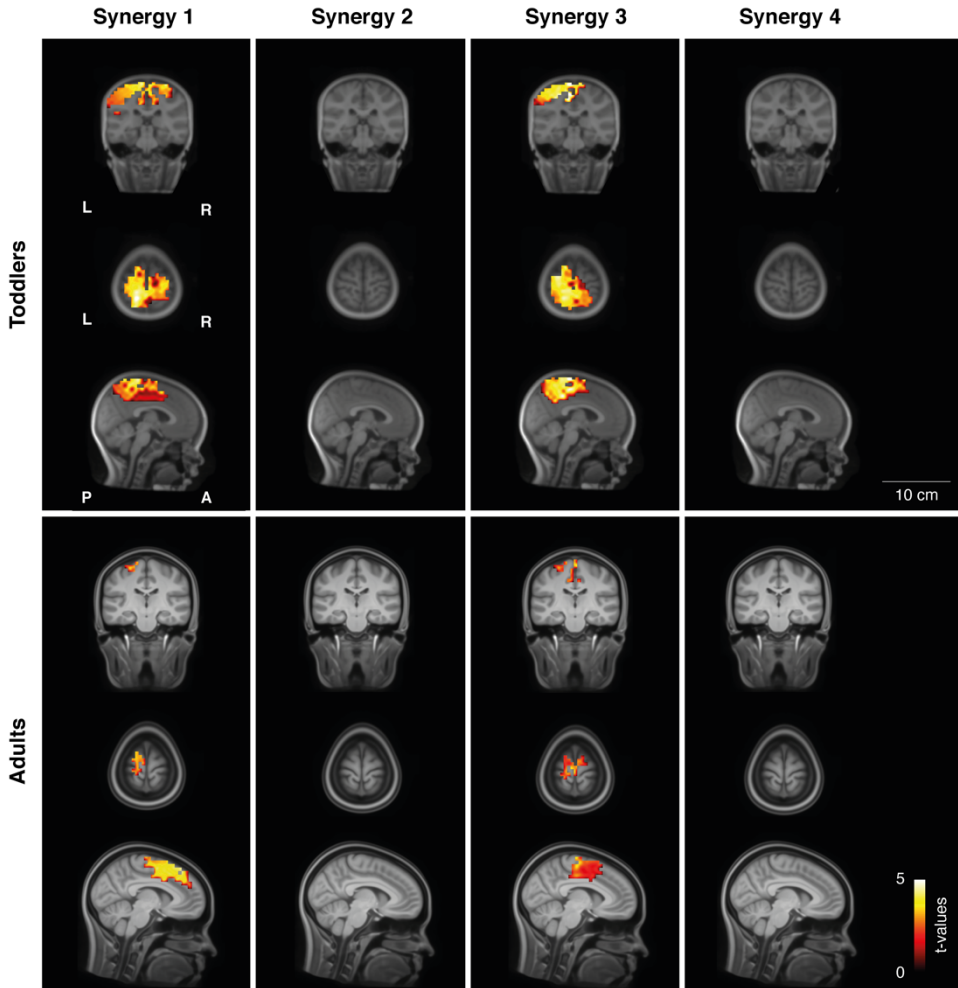
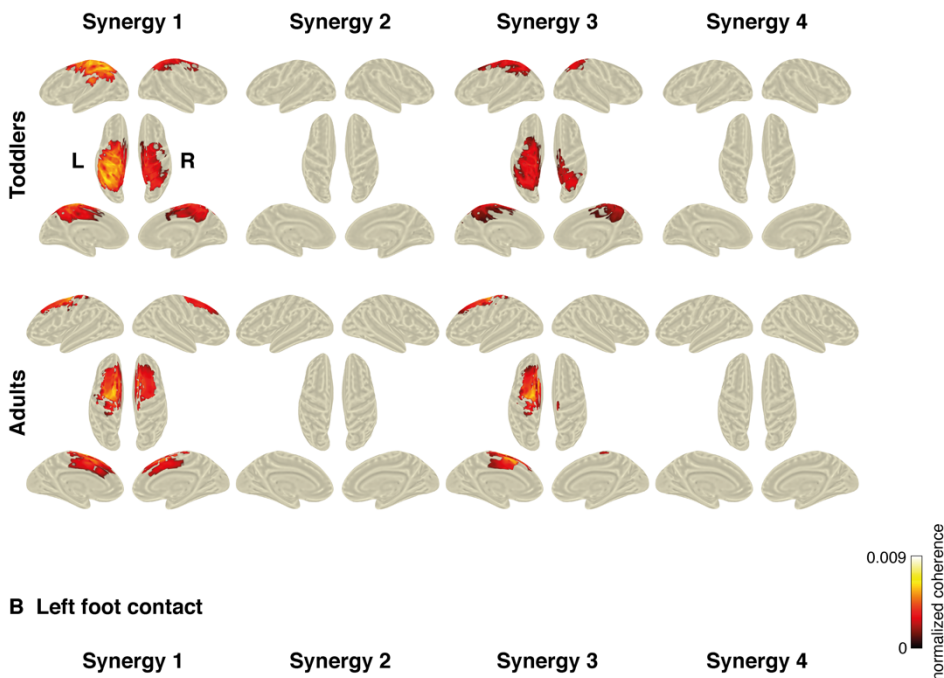


Figure S4.6 – Statistical coherence representations for toddlers (top) and adults (bottom) when time locking from left-to-left foot contact. Cortical beta-band volumes were subjected to one-sided t-tests for the contrast ‘coherence minus subject-specific mean coherence > 0’ ($p < 0.005$). Significant sources for these contrasts are projected onto age-matched template MRIs. L: left; R: right; P: posterior; A: anterior.

A Right foot contact



B Left foot contact

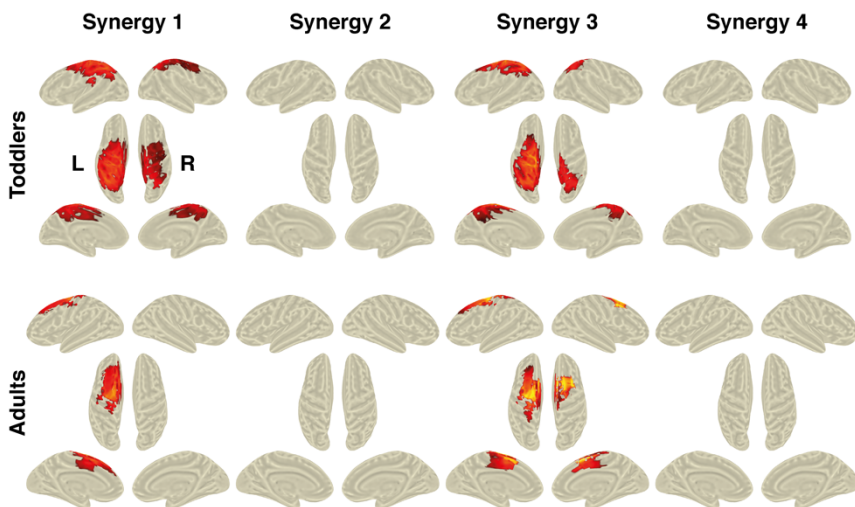


Figure S4.7 – Beta-band coherence projected on inflated surfaces for toddlers (top) and adults (bottom). (A) Right and (B) left foot contact correspond to the event used for time locking during source analysis. Cortical volumes were subjected to one-sided t-tests for the contrast ‘coherence minus subject-specific mean coherence > 0’ ($p < 0.005$) to create a mask to identify cortical areas resembling significant coherence. L: left; R: right.

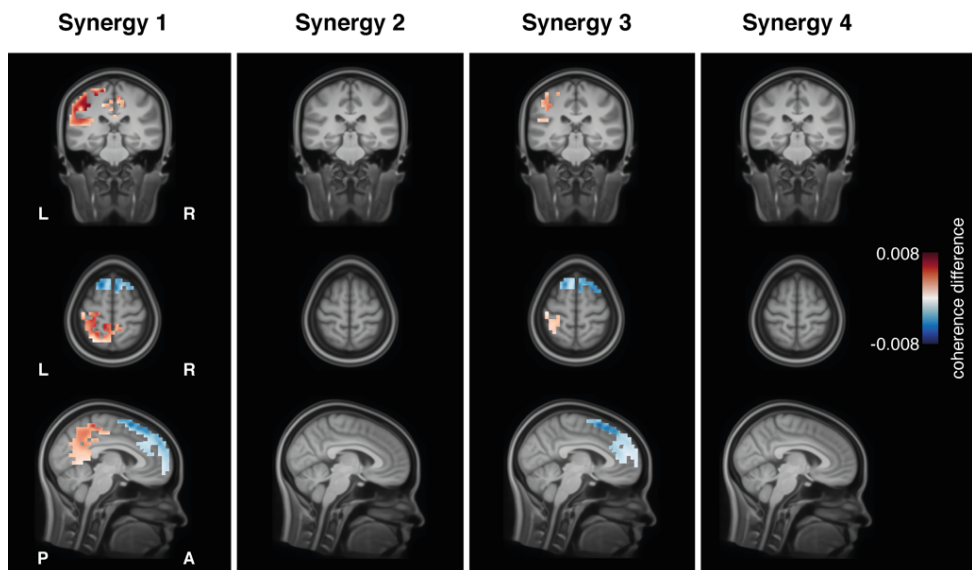


Figure S4.8 – Toddler-adult differences of the cortical muscle synergy representations presented as mean coherences. Source-localised coherence volumes of toddlers and adults were subjected to statistical tests to evaluate for between-group differences. Sources have been defined as mean coherence difference between toddlers and adults for the contrast ‘Toddlers minus Adults’. Hence, a positive coherence difference indicates a higher coherence for toddlers compared to adults. Cortical volumes are masked by the voxels that were significant when testing the contrast ($p < 0.025$; Figure S4.9). L: left; R: right; P: posterior; A: anterior.

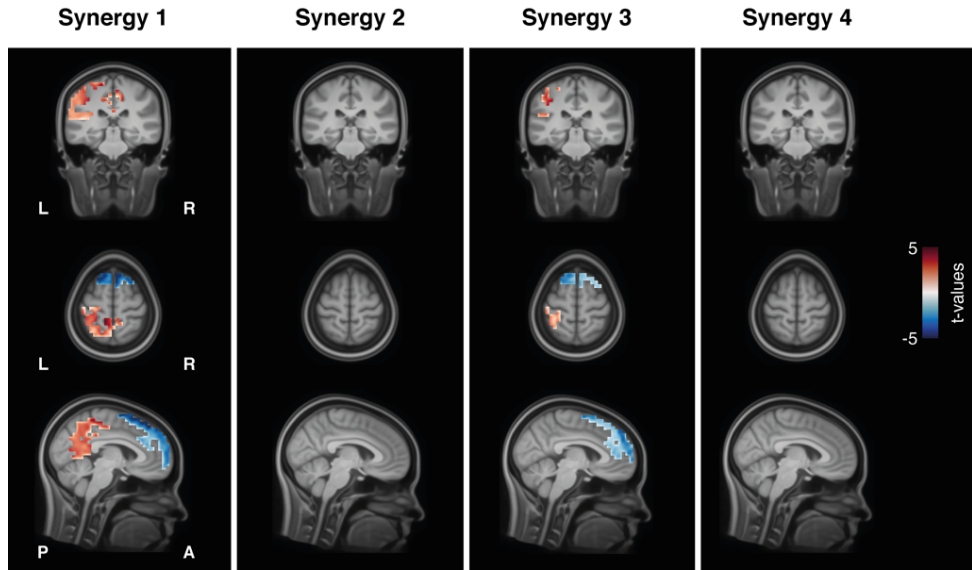


Figure S4.9 – Toddler-adult differences of the cortical muscle synergy representations presented as significant *t*-values after unpaired *t*-testing between the two groups. Source-localised coherence volumes of toddlers and adults were subjected to statistical tests to evaluate for between-group differences. Sources have been based on the contrast ‘Toddlers minus Adults’. Hence, positive *t*-values indicate higher coherence for toddlers compared to adults. Cortical volumes are masked by the voxels that were significant when testing the contrast ($p < 0.025$). L: left; R: right; P: posterior; A: anterior.

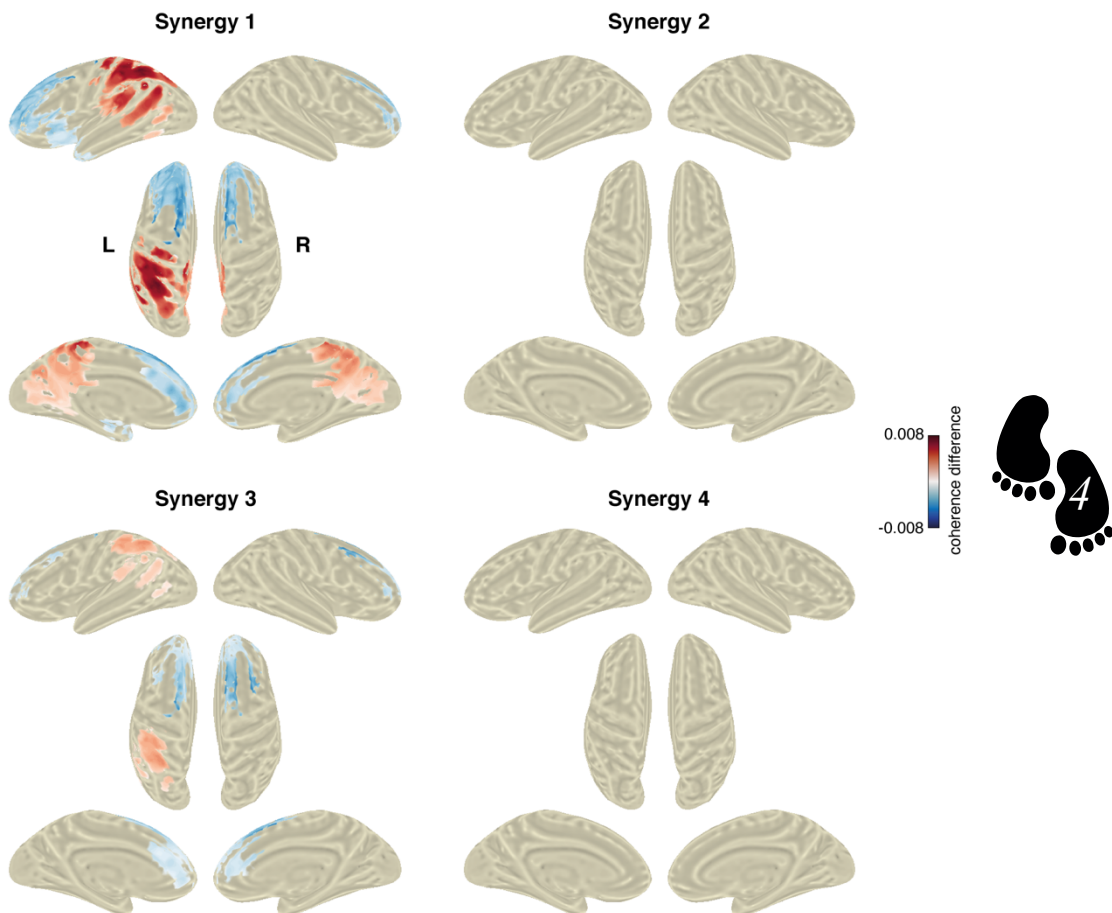


Figure S4.10 – Between-group statistics of the beta-band coherence projected on inflated surfaces. Sources have been based on the contrast ‘Toddlers minus Adults’. Hence, positive coherence differences indicate higher coherence for toddlers compared to adults. Cortical volumes are masked by the voxels that were significant when testing the contrast ($p < 0.025$). L: left; R: right.

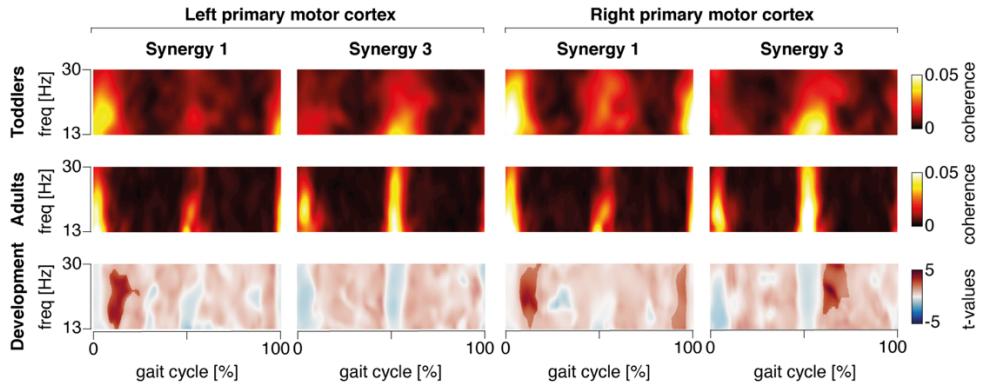


Figure S4.11 – Time-frequency magnitude-squared coherence between bilateral primary motor cortices and synergies 1 and 3. Gait cycle is defined from right-to-right foot contact. Time-frequency coherences are pooled over participants for every synergy pattern for toddlers (upper row) and adults (middle row). Opaque colours indicate significant t-values for the developmental changes (lower row). Positive t-values yield higher coherence for toddlers compared to adults. freq: frequency.

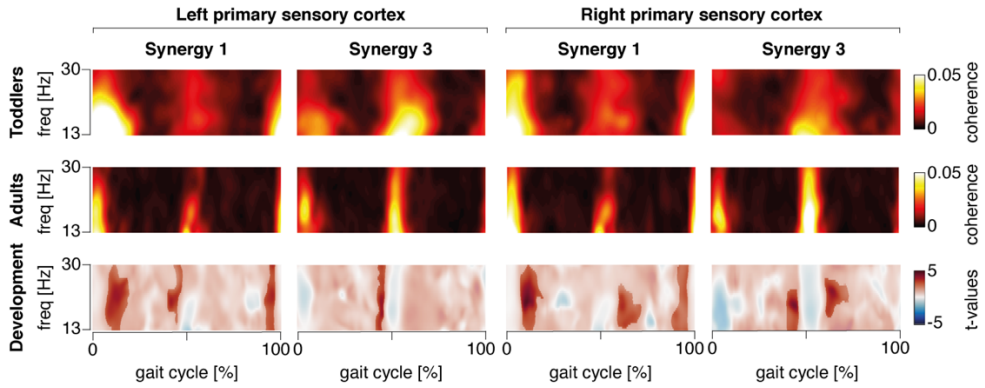


Figure S4.12 – Time-frequency coherence between primary sensory cortices and synergies 1 and 3. Similar format as Figure S4.11. Developmental coherence changes are larger in the primary sensory cortices compared to the primary motor cortices (lower row of Figure S4.11). Opaque colours indicate significant t -values for the developmental changes (lower row). Positive t -values yield higher coherence for toddlers compared to adults. freq: frequency.



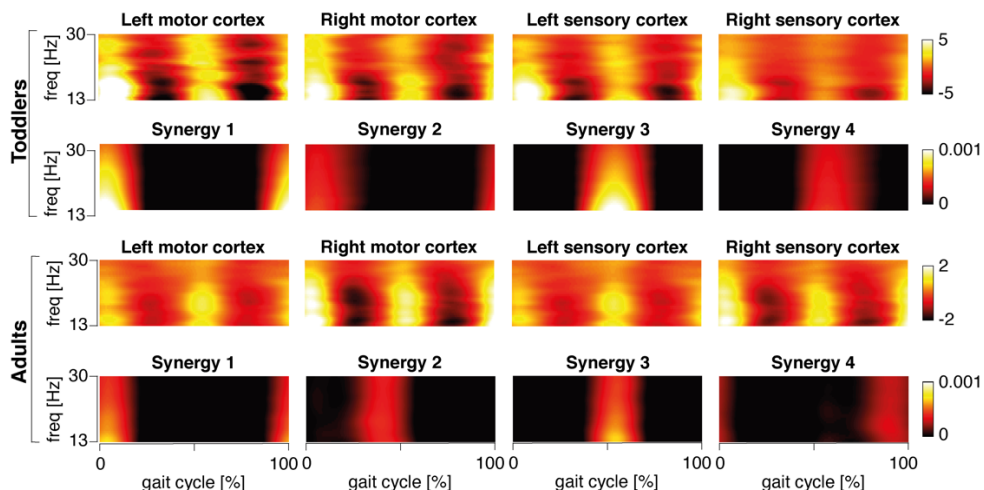


Figure S4.13 – Event-related amplitude modulation of the primary sensorimotor cortices and muscle synergies. Amplitude modulation was defined as the instantaneous Hilbert amplitude. The amplitude of the cortical and synergy activity modulates as a function of the gait cycle. The cortical activity shows event-related beta-band [de-]synchronisation. Beta-band amplitude of the virtual activation patterns is temporally aligned to the temporal patterns of the synergies. *freq*: frequency.

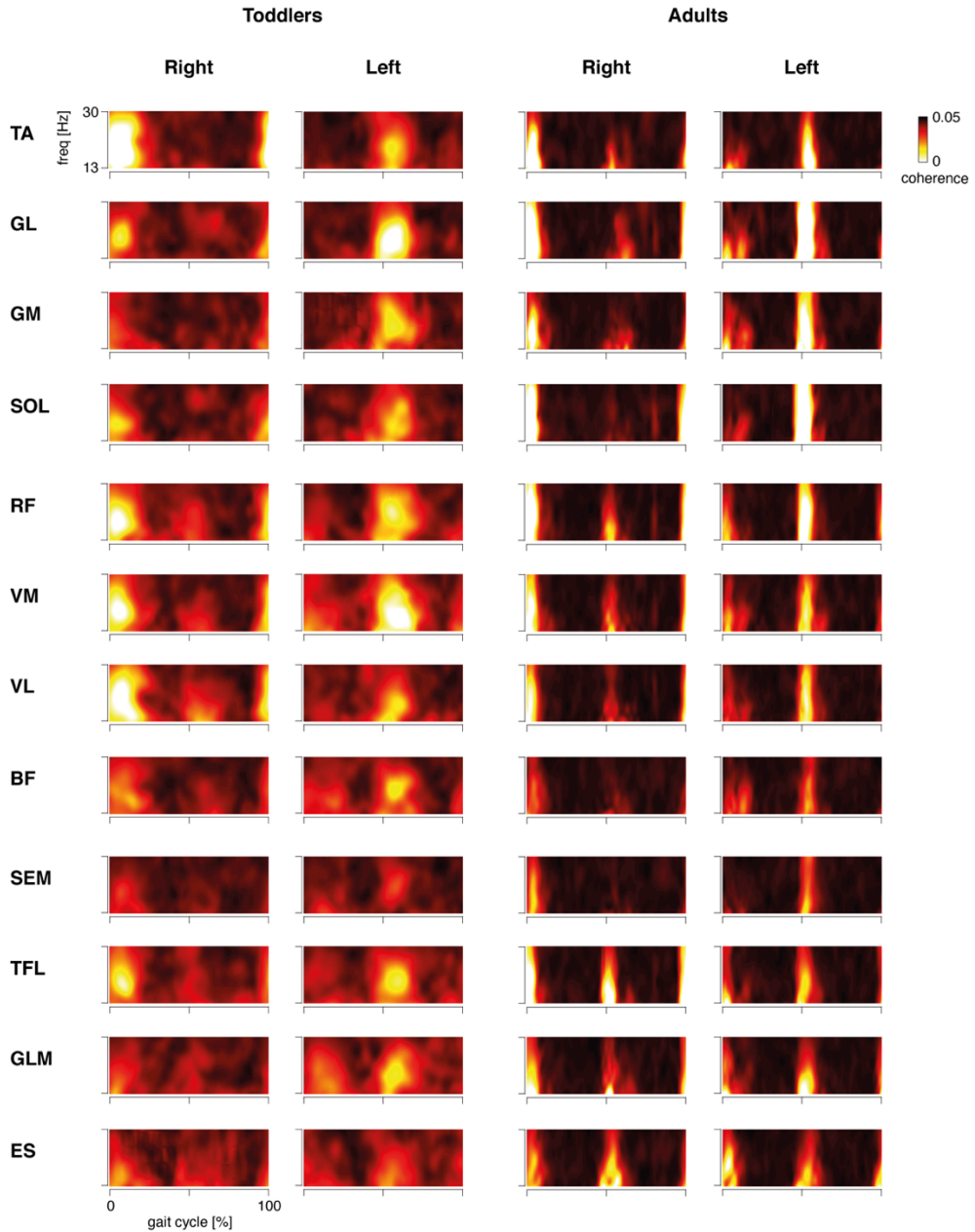


Figure S4.14 – Pairwise cortico-muscular coherence estimates between channel Cz and all individual muscles. Gait cycle is defined from right-to-right foot contact. Time-frequency coherences are pooled over participants for every muscular pattern for toddlers and adults. Abbreviations: freq - frequency; TA: tibialis anterior; GL: gastrocnemius lateralis; GM: gastrocnemius medialis; SOL: soleus; RF: rectus femoris; VM: vastus medialis; VL: vastus lateralis; BF: biceps femoris; SEM: semitendinosus; TFL: tensor fasciae latae; GLM: gluteus maximus; ES: erector spinae; freq: frequency.

Table S4.1. Test-statistic characteristics of the cortical muscle synergy representations.

	# synergy	Atlas area	Peak t-val.	RAS [mm]	MNI [mm]	Talairach [mm]
Toddlers	S1	left superior parietal gyrus	6.31	[0, -51, 63]	[0, -47, 84]	[0, -42, 79]
	S2	-	-	-	-	-
	S3	left precentral gyrus	5.87	[-5, -26, 62]	[-5, -22, 82]	[-5, -18, 76]
	S4	-	-	-	-	-
Adults	S1	left postcentral gyrus; left superior parietal gyrus	4.54	[-23, -35, 52]	[-22, -25, 65]	[-22, -21, 61]
	S2	-	-	-	-	-
	S3	left middle frontal gyrus	4.17	[-31, 26, 37]	[-30, 34, 43]	[-30, 35, 38]
	S4	-	-	-	-	-

S1: synergy 1; S2: synergy 2; S3: synergy 3; S4: synergy 4; RAS: right anterior superior; MNI: Montreal Neurological Institute

Table S4.2. Mean fraction of negative activations within the virtual temporal components averaged across participants.

	Toddlers	Adults
Synergy 1	0.0	0.0
Synergy 2	0.111	0.071
Synergy 3	0.0	0.018
Synergy 4	0.100	0.088



Defining the filter parameters for phase-amplitude coupling from a bispectral point of view

Background: Two measures of cross-frequency coupling are Phase-Amplitude Coupling (PAC) and bicoherence. The estimation of PAC with meaningful bandwidth for the high-frequency amplitude is crucial in order to avoid misinterpretations. While recommendations on the bandwidth of PAC's amplitude component exist, there is no consensus yet. Theoretical relationships between PAC and bicoherence can provide insights on how to set PAC's filters.

New method: To illustrate this, PAC estimated from simulated and empirical data are compared to the bispectrum. We used simulations replicated from earlier studies and empirical data from human electro-encephalography and rat local field potentials. PAC's amplitude component was estimated using a filter bandwidth with a ratio of (1) 2:1, (2) 1:1, or (3) 0.5:1 relative to the phase frequency.

Results: For both simulated and empirical data, PAC was smeared over a broad frequency range and not present when the estimates comprised a 2:1- and 0.5:1-ratio, respectively. In contrast, the 1:1-ratio accurately avoids smearing and results in clear signals of cross-frequency coupling. Bicoherence estimates were found to be essentially identical to PAC calculated with the recommended frequency setting.

Comparison with Existing Method(s): Earlier recommendations on filter settings of PAC lead to estimates which are smeared in the frequency domain, which makes it difficult to identify cross-frequency coupling of neural processes operating in narrow frequency bands.

Conclusions: We conclude that smearing of PAC estimates can be avoided with a different choice of filter settings by theoretically relating PAC to bicoherence.



Adapted from: C.S. Zandvoort, & G. Nolte (2021). *Defining the filter parameters for phase-amplitude coupling from a bispectral point of view*. Journal of Neuroscience Methods, **350**, 109032. doi: [10.1016/j.jneumeth.2020.109032](https://doi.org/10.1016/j.jneumeth.2020.109032)

Introduction

Electro-encephalography (EEG), magnetoencephalography (MEG), and local field potentials (LFPs) are often used to measure brain activity. They allow for the registration of neuronal population activity with high temporal precision. Associations within and between neural populations are regularly assessed using second-order measures, like power- and cross-spectral estimates. However, such measures are constrained to merely reveal linear interactions between signals. It does not come as a surprise that brain activity also contains neural dynamics related to nonlinear processes (Florin & Baillet, 2015; Jensen & Colgin, 2007; Tort et al., 2007). To unravel these dynamics, nonlinear measures have gained much popularity in recent decades.

In general, measures of cross-frequency coupling describe the nonlinear interactions of signals across frequencies, being it coupling across amplitude, phase, or frequency. A cross-frequency coupling measure that was rather unexplored but gained increasingly popularity to assess phase-amplitude interactions is bicoherence (Bartz et al., 2019; Shahbazi et al., 2018). Bicoherence describes the normalised cross-bispectrum. The cross-bispectrum is a measure of cross-frequency coupling since it evaluates the interactions across three frequencies. The first two frequencies can be chosen at will and the third frequency is always constrained to be the sum of these two frequencies. In statistical terms, the cross-bispectrum is the third-order moment in the frequency domain. Similar to coherence, bicoherence is a measure of phase-phase coupling even though it also somewhat depends on amplitudes because trials with larger amplitudes receive a larger weight in the average. This dependency on amplitudes should be distinguished from the observation by Hyafil (2015) that bicoherence is strongly related to phase-amplitude coupling because specific phase relations can in general generate an amplitude modulation. This is well known in acoustics as the phenomenon of beating where, for example, two sinusoidal sounds with similar frequencies lead to a modulated amplitude with the difference of these frequencies. In this setting, the modulation of one amplitude and the relation between two phases describe the same phenomenon in different terminology. If such an amplitude modulation is related to a phase of a low-frequency signal, then, this phenomenon can be described by both a relation of a low-frequency phase and a high-frequency amplitude and also by the relation of three phases at three different frequencies.

It is somewhat confusing that the term “phase-amplitude coupling” is used interchangeably in the literature to mean a specific phenomenon and also specific measures used to detect this phenomenon. The construction of those measures is guided by the idea of the mechanism: first, amplitudes and phases are extracted from the data, and then the functional relation between these signals is calculated. Here, we show in much detail that both bicoherence and PAC-measures detect phase-amplitude coupling as a phenomenon, but we will reserve the abbreviation PAC for those measures which are defined explicitly as a coupling between phase and amplitude.

Although PAC and bicoherence are related and share similarities (Kovach et al., 2018), it has been argued that bicoherence has several advantages over PAC (Shahbazi et al., 2018). One advantage of bicoherence over PAC is that it is not necessary to filter the signals before cross-frequency coupling computation since Fourier transforms are iteratively performed over isolated frequencies. Earlier investigations also emphasised that the filter characteristics (i.e., centre frequencies and bandwidth) of PAC have effects on the subsequent estimates (Berman et al., 2012). Hence, filter features selected for both the low- and high-frequency signals can affect the detection of PAC significantly. The bandwidth of the high-frequency component is critical in accurately estimating PAC. A bandwidth that is chosen too narrow or broad is prone to statistical errors (i.e., result in false negatives and positives, respectively). The optimal bandwidth settings remain to be examined further. A recent investigation recommended that the bandwidth of the amplitude component should be at least twice as large as the frequency of the phase component (Aru et al., 2015). This recommendation was followed by experimental studies (Cheng et al., 2016; Martínez-Cancino et al., 2019; Murta et al., 2017; Seymour et al., 2017). If one aims to investigate narrow-band brain rhythms and their higher harmonics; however, a bandwidth that is twice as large as the phase component would result in the inclusion of multiple carrier frequencies. Although this would result in significant PAC, clear smearing across neighbouring frequencies will be shown. To find associations in brain rhythms that are operating within narrow frequency bands would therefore be too complicated for PAC. A typical example of a narrow-band rhythm is the alpha rhythm (8-12 Hz) and its higher harmonics in closed-eyes human resting state. PAC may prevent us to find coupling in such rhythms with a spectrally narrowed operational window.



In the current study, we show that the recommendation of taking a bandwidth of PAC's amplitude component that is twice as large as the frequency of the phase component is neither necessary nor optimal. This will especially be problematic when one investigates cross-frequency coupling for higher harmonics. To show this, we focus on phase-amplitude coupling from a bispectral analysis point of view and compare bicoherence and PAC analytically and findings of both simulations and empirical data. We first replicate the simulations performed in the earlier investigation for both PAC and bicoherence (Aru et al., 2015). Specifically, we show how bicoherence relates to PAC filtered with varying bandwidths for the amplitude component. This bandwidth is determined relative to the phase frequency and is set to double, the same as, and half this frequency. We additionally discuss the effects of estimating PAC with a squared and unsquared version of the amplitude component in a second set of simulated data. Empirical findings using human EEG and rat LFPs are reported to substantiate the simulation findings. For real EEG and LFPs data, we demonstrate how results for PAC depend more heavily on these ratios when one is interested in narrow-band neural dynamics, and how such findings can be understood from bicoherence analyses.

Methods

Phase-Amplitude Coupling and bicoherence definitions

Phase-Amplitude Coupling. Several versions of PAC exist, and we first recall the formal definition of PAC given in Canolty et al. (2006). The essential quantity for PAC, which we consider as a weighted phase locking, is

$$P(f_L, f_H) = \langle |x_H(t)| e^{i\Phi_L(t)} \rangle_t = \left\langle |x_H(t)| \frac{x_L(t)}{|x_L(t)|} \right\rangle_t \quad (5.1)$$

where $x_L(t)$ and $x_H(t)$ are the (complex) Hilbert transforms of a signal filtered in a low- and high-frequency band with centres at frequencies f_L and f_H , respectively. i corresponds to $\sqrt{-1}$. We here defined P as a complex number and consider its absolute value as a

coupling measure if needed. The corresponding phases and magnitudes at time t are denoted by $\Phi_L(t)$ and $|x_{L/H}(t)|$, and $\langle \cdot \rangle_t$ denotes the average over time. From P and corresponding values of that quantity for surrogate data, P_s , where the low- and high-frequency parts are shifted relative to each other by a random delay, Canolty et al. (2006) calculate a z-score as

$$PAC = \frac{|P| - \text{mean}(|P_s|)}{\text{std}(|P_s|)} \quad (5.2)$$

where $\text{mean}(|P_s|)$ and $\text{std}(|P_s|)$ are the mean and standard deviation of $|P_s|$, respectively, calculated of K surrogate datasets. In our opinion, the calculation of this z-score and its interpretation as a Gaussian distributed variable with zero mean and unit standard deviation is not trivial, because $|P|$ tend to be non-Gaussian distributed. An alternative statistic will be discussed in section *Statistical assessments*. Apart from details how significance is estimated, the crucial point is that in this approach PAC is normalised statistically.

Using a statistical normalisation, one cannot directly compare results for a different number of trials. For example, when there is a true effect, the normalised quantity diverges if the number of trials goes to infinity. This would be different for a non-statistical normalisation where the result converges to a constant in that limit.

A different approach was suggested by Osipova et al. (2008) where the coherence between the instantaneous high-frequency power and the original data was calculated at some low frequency. A difference is that coherence includes a normalisation while Canolty et al. (2006) only use a statistical normalisation, i.e., coupling measures are normalised by estimates of the standard deviation. Here, we will present results using both a conventional and statistical normalisation, and we therefore essentially adopted the approach by Osipova et al. (2008) with an additional statistical normalisation.

Another difference is that instantaneous power is calculated by Osipova et al. (2008) with a wavelet approach rather than Hilbert-transformed high-frequency filtered data. We slightly deviate from the approach by Osipova et al. (2008) by using high-frequency amplitude rather than power and we used the absolute value of the Hilbert transform of the filtered data rather than wavelets to estimate the time-dependent amplitude, because we then have more freedom to design an appropriate filter. In particular, we used a filter which is



essentially flat within the high-frequency band, whereas the wavelet approach corresponds to a filter which is maximal in the centre of the band and decreases with distance from the centre.

We emphasise that relations between PAC and bispectra, as will be recalled or newly derived below, can only be found if the respective PAC measure can be expressed by third-order statistical moments. With minor modifications, this is the case for the approaches in Osipova et al. (2008) and Canolty et al. (2006), but this is not the case for the modulation index proposed by Tort et al. (2010).

Relations for the bispectra and conventional PAC were discussed in Shahbazi et al. (2018). In section *Relations between Phase-Amplitude Coupling and bispectra*, we analytically prove that the approach of Osipova et al. (2008) leads to the same relation with the bispectra, but we would like to first comment on the relations between estimations based on wavelets and the Hilbert transform. In a wavelet approach, the complex signal $x_H(t)$ at frequency f_H is calculated as

$$x_H(t) = (x * h_{f_H})(t) \quad (5.3)$$

where $*$ denotes convolution, x is the original time series, and $h_{f_H}(t)$ is the wavelet.

To simplify the notation, we consider an odd number of discrete time points running from $-N$ to N , and the Fourier transforms, to be used below, are defined for discrete frequencies f also running from $-N$ to N . With such a convention the wavelet is defined as

$$h_{f_H}(t) = h_0(t) \exp(-i2\pi f_H t / (2N + 1)) \quad (5.4)$$

with $h_0(t)$ chosen by Osipova et al. (2008) to be a Hanning window. This window is multiplied by the Fourier transform at some high frequency. PAC is finally defined in that approach as the coherence at some low frequency f_L between the original data and the instantaneous power, $V(t)$. $V(t)$ can then be defined as

$$V(t) = |x_H(t)|^2 \quad (5.5)$$

In the context of PAC, we prefer the Hilbert approach over the wavelet approach, but there is no fundamental difference between them. To see this, let $\hat{h}_0(f)$ be the Fourier transform of the window, which is substantially different from zero only for small frequencies. Then the Fourier transform of the wavelet reads

$$\hat{h}_{f_H}(f) = \hat{h}_0(f - f_H) \quad (5.6)$$

The convolution of Eq. 5.3 is a product in the Fourier domain, and hence

$$x_H(t) = \frac{1}{2N+1} \sum_f \hat{h}_0(f - f_H) \hat{x}(f) \exp(i2\pi f t / (2N+1)) \quad (5.7)$$



with $\hat{x}(f)$ being the Fourier-transformed signal. The exponent term denotes the inverse Fourier transform. The crucial point now is that, while $\hat{h}_0(f)$ does not vanish for negative frequencies, $\hat{h}_0(f - f_H)$ is negligible for negative frequencies provided that the high frequency f_H is remote from zero and the Nyquist frequency relative to the width of the wavelet in the frequency domain. We here assume that this is an excellent approximation in practice, and using this approximation we can write

$$x_H(t) = \frac{1}{2N+1} \sum_{f>0} \hat{h}_0(f - f_H) \hat{x}(f) \exp(i2\pi f t / (2N+1)) \quad (5.8)$$

which only differs from Eq. 5.7 by the range of the sum over f . This has the form of a Hilbert transform of a filtered signal with the filter given by $\hat{h}_0(f - f_H)$. Thus, the wavelet approach

is, to excellent approximation, equivalent to the approach based on the Hilbert transformation. This result is almost identical to the main result of Bruns (2004), where it is argued that these two approaches are formally equivalent. The only difference is that we do not think that the derivation given by Bruns (2004) is perfectly accurate, but contains an approximation at some point.

Bispectra and bicoherence. The cross-bispectrum is a poly-spectrum, or more specifically, the third-order statistical moment of the Fourier transform. The cross-bispectrum reads in the most general form for channels k, m, n and frequencies f_1 and f_2

$$B_{kmn}(f_1, f_2) = \langle \hat{x}_k(f_1) \hat{x}_m(f_2) \hat{x}_n^*(f_1 + f_2) \rangle \quad (5.9)$$

where $\hat{x}_k(f)$ denotes the Fourier transform of data in channel k at frequency f and $*$ the complex conjugate. $\langle . \rangle$ is the expectation value, which can be estimated using a windowed segmentation approach. The third frequency of the cross-bispectrum is always constrained to be the sum of f_1 and f_2 .

The cross-spectrum is a nonlinear measure of a single time series across multiple frequencies. To be able to interpret bicoherence like coherence, the cross-bispectrum is here normalised with a three-norm defined as

$$N_{kmn}(f_1, f_2) = (\langle |\hat{x}_k(f_1)|^3 \rangle \langle |\hat{x}_m(f_2)|^3 \rangle \langle |\hat{x}_n(f_1 + f_2)|^3 \rangle)^{1/3} \quad (5.10)$$

to obtain a coupling measure with absolute value bounded between 0 and 1 (Shahbazi et al., 2014). Bicoherence is obtained by dividing the cross-bispectrum of Eq. 5.9 by normalisation as described in the equation above

$$b_{kmn}(f_1, f_2) = \frac{B_{kmn}(f_1, f_2)}{N_{kmn}(f_1, f_2)} \quad (5.11)$$

The open-source software code to estimate univariate bicoherence as provided in Eq. 5.11 is available in the MATLAB-based toolbox *MEG & EEG - Toolbox of Hamburg (METH-toolbox)*, which can be downloaded from the website of the Department of Neurophysiology and Pathophysiology at the Universitätsklinikum Hamburg-Eppendorf (<https://www.uke.de/english/departments-institutes/institutes/neurophysiology-and-pathophysiology/research/research-groups/index.html>).

Relations between Phase-Amplitude Coupling and bispectra

To set the filter of PAC's low- and high-frequency component using bispectral analysis, we show how PAC is related to bicoherence. Relations between both quantities were defined in earlier studies (Kovach et al., 2018; Shahbazi et al., 2018). PAC as used in Osipova et al. (2008) and the current study was slightly different from the widely applied version of PAC (Canolty et al., 2006). Here, we define PAC as the coherence between the original data and the instantaneous power using the Hilbert transform rather than using wavelets. Note that relations between PAC and bispectra can be given only for the numerator and not for the normalisation factors.



The Hilbert transform of filtered data in the high-frequency band reads

$$x_H(t, f_H) = \frac{2}{2N+1} \sum_f F(f, f_H) \hat{x}(f) \exp(i2\pi f t / (2N+1)) \quad (5.12)$$

where $F(f, f_H)$ is the filter with centre f_H which is assumed here to be real valued. Also, in this formulation $F(f, f_H)$ is set to zero for negative f . The numerator is multiplied by a factor 2 since half the frequencies are omitted. Hence, the magnitude of the Hilbert-transformed signal matches the original filtered signal. Using the orthogonality of sinusoidal functions to

show that isolated frequencies are uncorrelated, one could substitute part of the inverse Fourier transform by the Kronecker-delta function (denoted as the delta function below)

$$\sum_t \exp(i2\pi ft/(2N+1)) = (2N+1)\delta_{f,0} \quad (5.13)$$

The Fourier transform of the power $V(t, f_H) \equiv |x_H(t, f_H)|^2$ at some frequency f_L reads

$$\hat{V}(f_L, f_H) = \sum_t |x_H(t, f_H)|^2 \exp(-i2\pi f_L t/(2N+1)) \quad (5.14)$$

with \hat{V} being the Fourier-transformed power that depends on a low and high frequency and $|x_H(t, f_H)|^2$ being the instantaneous power of the high-frequency component. Considering Eq. 5.14 and integrating Eq. 5.12 into this equation results in

$$\begin{aligned} \hat{V}(f_L, f_H) &= \frac{4}{(2N+1)^2} \sum_{f_1, f_2} F(f_1, f_H) F(f_2, f_H) \hat{x}(f_1) \hat{x}^*(f_2) \sum_t \exp(i2\pi t(f_1 - f_2 - f_L)) \\ &= \frac{4}{2N+1} \sum_f F(f, f_H) F(f + f_L, f_H) \hat{x}(f) \hat{x}^*(f + f_L) \end{aligned} \quad (5.15)$$

The cross-spectrum, c , at frequency f_L between the original data and the power now reads

$$c(f_L, f_H) = \langle \hat{x}(f_L) \hat{V}(f_L, f_H) \rangle \quad (5.16)$$

in which \hat{V} can be substituted by Eq. 5.15, which reads

$$\begin{aligned}
c(f_L, f_H) &= \frac{4}{2N+1} \sum_f F(f, f_H) F(f + f_L, f_H) < \hat{x}(f_L) \hat{x}(f) \hat{x}^*(f + f_L) > \\
&= \frac{4}{2N+1} \sum_f F(f, f_H) F(f + f_L, f_H) B(f_L, f)
\end{aligned} \tag{5.17}$$

with B denoting the bispectrum as defined in Eq. 5.9.

Setting the low- and high-frequency filters

While the width of the filter for the high-frequency part is much debated, the filter for the low-frequency part can in principle be arbitrarily narrow and is only limited by the trade-off between frequency resolution, statistical robustness, and stability of the low-frequency process. To discuss the implications of the above relation we will therefore introduce a simplification and assume that the low-frequency filter is point-like in the frequency domain, i.e.,

$$F_L(f_L, f_L) = \delta_{f_L, f_L} \tag{5.18}$$

which leads to

$$c(f_L, f_H) = \sum_f G(f, f_L, f_H) B(f_L, f) \tag{5.19}$$

with the kernel G that is equal to

$$G(f, f_L, f_H) = F_H(f, f_H) F_H(f + f_L, f_H) \tag{5.20}$$



where $F_H(f, f_H)$ is the filter with centre f_H which is assumed here to be real valued and bandwidth depending on f_L . The kernel is a product of the high-frequency filter and a shifted version of it and, hence, \tilde{P} (i.e., the coherence-based PAC) is in general a smeared version of B .

The smearing is negligible if the kernel G is approximately equal to a delta function. For perfect high-frequency filters, i.e., if the filters are 1 within some band and vanish outside that band, the filter kernel is approximately equal to a delta function if the width is chosen to be slightly larger than the low frequency f_L (i.e., $\Delta f = f_L + \epsilon$ with ϵ being a small positive number). The filter and its shifted version then only overlap in a very narrow frequency region and the kernel has a sharp peak. A schematic visualisation of such a filter kernel is visualised in Figure 5.1B. More formally, if

$$F_H(f, f_H) = \chi_{[f_H - \Delta f/2, f_H + \Delta f/2]}(f) \quad (5.21)$$

in which Δf denotes the bandwidth and $\chi_A(f)$ is the characteristic function for the filter on the interval A , here, specified around f_H . If choosing $\Delta f = f_L + \epsilon$ with a tiny number ϵ , then

$$F_H(f + f_L, f_H) = \chi_{[f_H - \Delta f/2 - f_L, f_H + \Delta f/2 - f_L]}(f) \quad (5.22)$$

and having a kernel G that approximates the delta function

$$G(f, f_L, f_H) = \chi_{[f_H - f_L/2 - \epsilon/2, f_H - f_L/2 + \epsilon/2]}(f) \approx \delta_{f, f_H - \Delta f/2} \quad (5.23)$$

leading to

$$\tilde{P}(f_L, f_H) \sim B(f_L, f_H - f_L/2) \quad (5.24)$$

Note that in this case \tilde{P} and B are identical apart from a frequency shift by $f_L/2$ and apart from an overall constant, which depends on the filter and is usually irrelevant. The frequency shift is due to different conventions regarding what is meant by a frequency. That shift would disappear if PAC would be written as a function of the lower end of the filter rather than the centre. For example, the first higher harmonic of the alpha rhythm (i.e., coupling between 10 and 20 Hz) could be observed with PAC with a bandwidth of 10 Hz for the high-frequency filter at low frequency $f_L = 10$ Hz and high frequency $f_H = 15$ Hz, because then the high-frequency band includes both signals at 10 and 20 Hz. In contrast, the same phenomenon can be observed with the bispectrum at $f_1 = f_2 = 10$ Hz, which corresponds to a coupling between 10 Hz and $f_1 + f_2 = 20$ Hz. Note that displaying PAC as a function of the centre of the high-frequency band can be misleading in the case of higher harmonics because we would observe a peak at 15 Hz even though there is no relevant signal at 15 Hz.

In practice, filters are not perfect, and it is not necessary to choose the filter width slightly larger than the low frequency. Rather, choosing the width of the high-frequency filter to be equal to the low-frequency results in sharp kernels (with details depending on filter order) and avoids smearing over frequencies. We therefore recommend selecting the filter bandwidth of the high-frequency component in a 1:1-ratio relative to the frequency of the phase component. In other words, the amplitude component of PAC is filtered with a bandwidth that is linearly proportional to the frequency of the phase component in a 1:1-ratio. This filter setting should avoid spectral leakage for PAC (i.e., smearing) over a broad frequency band and identify narrow-band coupling. The effect of such a filter width on the kernel G is shown in Figure 5.1B. Taking a larger bandwidth includes the signal content of more neighbouring frequencies, resulting in smearing of PAC. As an earlier study recommended to have a filter width of the amplitude component that is twice as large as the phase frequency (Aru et al., 2015), we filter the amplitude component and phase frequency in a 2:1-ratio. Following our theory defined above, this kernel will result in a smeared version of PAC (Figure 5.1A). On the other hand, if the ratio gets smaller than 1:1, PAC inevitably vanishes (Figure 5.1C). To show that the bandwidth cannot be too small, we additionally filter the amplitude component with a bandwidth that is half the frequency of the phase component (0.5:1-ratio). Figure 5.2 provides a detailed overview which steps were taken to compute bicoherence and PAC.



This is the main theoretical result of this paper which will be illustrated below for simulated and empirical data, in which we will compute PAC using these above-mentioned filter settings of PAC and relate it to bicoherence. For simplicity, we only focus on the univariate cases of bicoherence and PAC. We finally recall that such relations are only valid for the numerators of the coupling measures, but for bicoherence it was shown in Shahbazi et al. (2014) and Shahbazi et al. (2018) that different normalisations have almost no effect on its statistical properties.

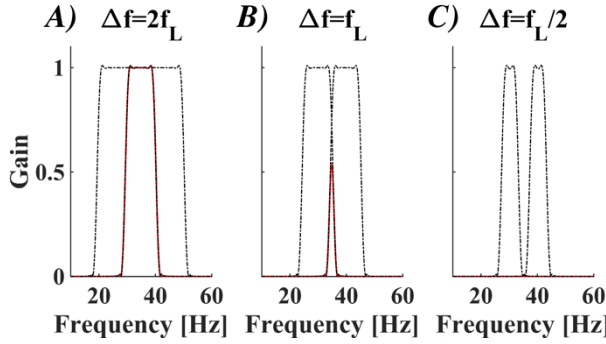


Figure 5.1 – Filters were calculated for fixed low frequency $f_L = 10$ Hz and high frequency $f_H = 40$ Hz for varying widths of the high-frequency band, denoted as Δf and indicated in the titles of the subpanels. The filters and the corresponding shifted filters are shown by black lines. The kernels G , i.e., the products of the filters, are shown in red. We used a FIR filter of 1s duration. At (B) $\Delta f = f_L$ we observe a (moderately) sharp kernel. For (A) $\Delta f = 2f_L$ the kernel is not sharp, and for (C) $\Delta f = f_L/2$ it basically vanishes altogether. Of course, the kernel can be made sharper with longer filters.

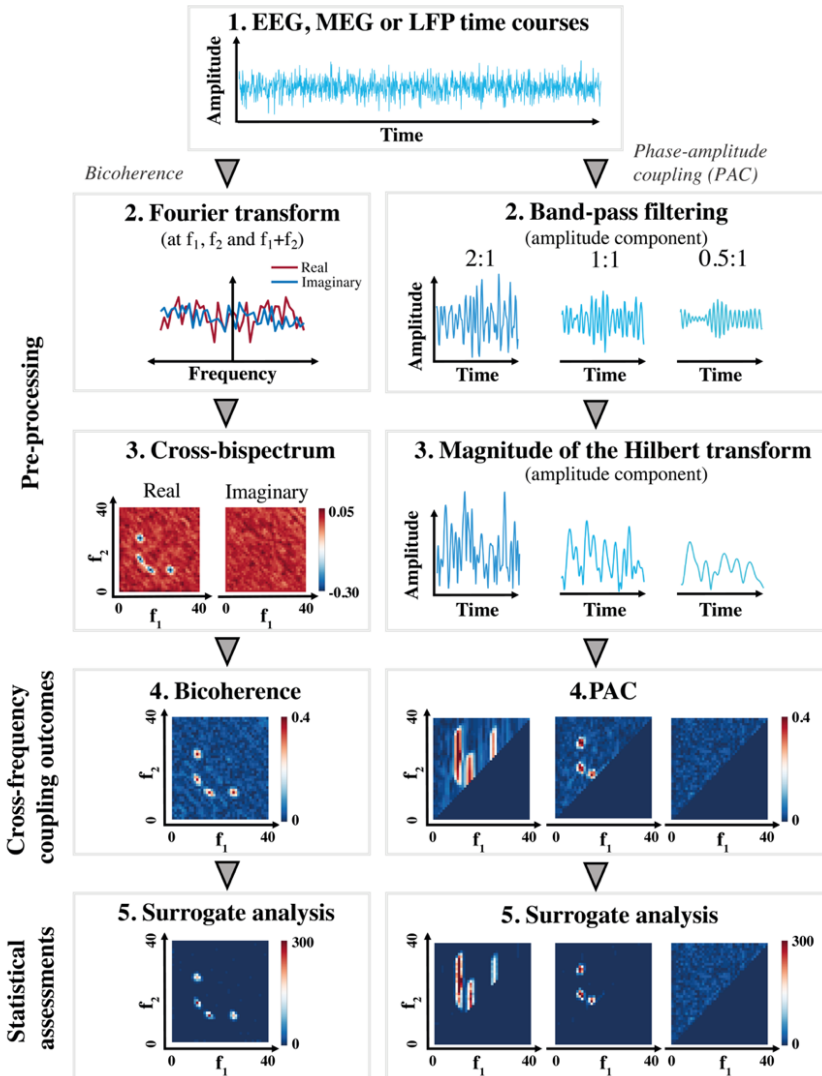


Figure 5.2 – Overview of the analysis pipelines in the current study to derive the bicoherence and phase-amplitude coupling (PAC) measures. (1.) Cross-frequency coupling measures can be computed from various electrophysiological time courses (e.g., EEG, MEG, or LFP). For the bicoherence case (left column), (2.) data is transformed to the frequency domain at the frequencies f_1 , f_2 , and $f_1 + f_2$. (3.) The complex-valued cross-bispectrum can be obtained iteratively for f_1 and f_2 . (4.) The magnitude of the cross-bispectrum corresponds to bicoherence. For the PAC-case (right column), (2.) the bandwidth to filter the amplitude component is considered being critical. Hence, time courses are filtered with three bandwidths at frequency f_2 . The bandwidth is proportionally scaled in a ratio of 2:1 (i.e., the bandwidth to filter the amplitude component is twice as large as the frequency of the phase component, f_1), 1:1, and 0.5:1 to the frequency of the phase component. (3.) After taking the magnitude of the Hilbert transform to get the amplitude component, (4.) PAC is estimated as the coherence between the original time course and high-frequency amplitude at some low frequency. For both bicoherence and PAC, (5.) statistical meaning of the outcomes was validated by surrogate analyses. For the illustrative examples in this flowchart, we simulated a time course having cross-frequency coupling with centre frequencies at 10 and 25 Hz.

Simulated data

We first focus on the simulations as performed by Aru and colleagues (2015). In their study, they simulated a univariate signal oscillating at different frequencies. More precisely, the simulated signals manifested PAC dynamics because the amplitude of the high-frequency signal was modulated by the phase of the low-frequency signal. We formulate the following time series which is analogous to theirs:

$$\begin{aligned} x(t) &= \sin(\Phi_L(t)) + (1 - \sin(\Phi_L(t))) \sin(\Phi_H(t)) + \eta(t) \\ &= \sin(\Phi_L(t)) + \sin(\Phi_H(t)) - \frac{1}{2}(\cos(\Phi_H(t) - \Phi_L(t)) - \cos(\Phi_H(t) + \Phi_L(t))) + \eta(t) \end{aligned} \quad (5.25)$$

where $\Phi_L(t)$ and $\Phi_H(t)$ denote the phase time series at some low and high frequency, and $\eta(t)$ is white Gaussian noise with a standard deviation of 3. The noise is added to avoid oscillating effects at irrelevant frequencies merely due to spectral leakage. We note that taking the phases as

$$\Phi_{L,H}(t) = 2\pi f_{L,H}t \quad (5.26)$$

would have resulted in comparable results in our case. However, taking pure sine waves in simulations should be avoided because of principal reasons. Pure sine waves have infinite auto-correlation length and, hence, if data are divided into epochs, all epochs are statistically dependent on each other. In fact, pure sine waves are not ergodic, meaning that the time averages are generally not identical to ensemble averages. As an example, consider two perfect sine waves of identical frequency but random and independent initial phases. The coherence between the two sine waves is 1 when calculated as a time average, because the phase difference is constant across time whereas it vanishes when calculated as an ensemble average, because the phases are random. Here, the phase time series are obtained from the phase of the Hilbert transforms of white Gaussian noise which was narrowly filtered around the frequencies of 10 and 40 Hz. We note that the simulated time series contain additional dominant frequencies at 30 and 50 Hz because of the modulated high-frequency component.

A common problem for the interpretation of PAC is the question whether the result is a consequence of genuine phase-amplitude coupling as opposed to the mere presence of a non-sinusoidal waveshape. However, such a distinction can be ambiguous as it is not clear why phase-amplitude coupling cannot result in repeated non-sinusoidal waveshapes. In particular, using deterministic phases as in Eq. 5.26 the simulated PAC results in waveshapes which are repeated every 100ms, which is not the case for random phases. Still, results for PAC and bicoherence are almost identical for the deterministic and stochastic version. The question whether a specific waveshape is repeated cannot be answered using third-order statistical moments only. In this paper, we do not make an attempt to answer that question, and we take the view that sharp peaks at multiples of the base frequency are likely to be caused by higher harmonics due to non-sinusoidal waveshapes.

The above-described theory on the equivalence between PAC and bicoherence specifically applies to third-order statistical moments and cannot be developed for second-order moments. Yet, we estimate PAC as the coherence between the original time series and the instantaneous amplitude. In a second simulation, we investigate the effects of using a squared (i.e., power) and unsquared (i.e., amplitude) version for PAC's amplitude component. The simulated signal comprised a sawtooth signal with cross-frequency coupling at a base frequency of 10 Hz and its higher harmonics (for bicoherence). To do so, we generated a sawtooth signal sampled at 500 Hz that repeats every 100ms with a total duration of 10 minutes. White noise with an equal variance was superimposed on top of this sawtooth signal.



Empirical electro-encephalographic and local field potential data

To substantiate our simulation findings, we compared estimates of bicoherence and PAC on empirical data recorded in humans and rats. Both datasets are open-source and publicly available on <http://clopinet.com/causality/data/nolte/> and <http://doi.org/10.5061/dryad.12t21>.

The human data comprise cleaned resting state EEG. The online dataset is a subset of data that was reported earlier (Nolte et al., 2008) as the original dataset consisted of 88 participants. In the experimental paradigm, participants were asked to close their eyes for 10-13 minutes. Simultaneously, EEG recordings were acquired, which were epoched into

152-202 segments of 4s each. 19-channel EEG (configured to the international 10-20 system) was registered at a sampling rate of 256 Hz. EEG data are referenced to a linked mastoids reference. Nineteen Ag/AgCl electrodes included Fp1, Fp2, F7, F3, Fz, F4, F8 T3, C3, Cz, C4, T4, T5, P3, Pz, P4, T6, O1, and O2. Given that we were interested in the coupling of narrow-band brain rhythms, the primary aim was to localise neural oscillations at the alpha rhythm and its higher harmonics. To find the strongest coupling effects, we specifically targeted the EEG channel comprising maximal alpha power. Hence, we selected channel 17 of participant 8 (i.e., the channel yielding maximal alpha power at 10 Hz) for further analysis. The alpha oscillations have a ground frequency around 10 Hz. The higher harmonics yield frequencies of a factor $k \times 10$ higher (with $k=1,2,3,\dots$).

Rat data comprise LFPs of seven animals. LFP data were recorded during 12 hours of sleep and awake periods. We report findings on the REM sleeping periods. LFP activity was recorded from the CA1 pyramidal cell layer of the hippocampus. Data of 16-channel silicon-layered probes were sampled at a rate of 1,000 Hz. In the original investigation, the authors mainly aimed to identify theta-gamma PAC (and cross-frequency phase-phase coupling) in hippocampal activity (Scheffer-Teixeira & Tort, 2016). We predominantly focus on the theta-gamma phase-amplitude coupling, which would be the cross-frequency coupling between the frequencies of 4-8 and 40-150 Hz. For the rat findings, we specifically report the results of channel 16 of rat 7.

Statistical assessments

In order to statistically assess single PAC and bicoherence representations, we applied a surrogate technique. The null-hypothesis is defined as the cross-frequency coupling being zero. More specifically, it is assessed whether non-zero values of PAC and bispectra can be considered as meaningful phase-amplitude coupling or as findings by chance. The surrogate analysis consists of time-shifting the amplitude component of PAC and shuffling the third Fourier transform of the cross-bispectrum. For the construction of the surrogate datasets we follow the approach of Canolty et al. (2006) but deviate in the statistical interpretation of the results. For PAC, we randomly time-shift the amplitude component by a random multiple of 1s with periodic boundary condition, and for the bispectra the same is done for the signal at the highest frequency (i.e., at frequency $f_1 + f_2$). Using the central limit theorem, under the

null-hypothesis P is approximately Gaussian distributed in the complex plane with zero mean and uniformly distributed phase. Then $|P|^2$ is exponentially distributed with density $pdf(|P|^2) \sim \exp(-|P|^2/\alpha^2)$ and with $\alpha^2 = \langle |P|^2 \rangle$ (Freyer et al., 2009). Furthermore, under the null-hypothesis P is drawn from the same ensemble as the surrogates, and hence α^2 can be estimated as

$$\alpha^2 \approx \langle |P_{surr}(k)|^2 \rangle_k \quad (5.27)$$

where $P_{surr}(k)$ is the coupling of the k .th surrogate dataset, and $\langle \cdot \rangle_k$ denotes average over all surrogate datasets. In the results shown below we will display the quantity

$$r = \frac{|P|^2}{\langle |P_{surr}(k)|^2 \rangle_k} \quad (5.28)$$



and it is straightforward to show, by integrating the probability density, that the p -values can be calculated as $p = \exp(-r)$. Statistical results for bispectra were calculated analogously. Note, for both PAC and bispectra, we used non-normalised quantities for statistical evaluation because it is these quantities which are plane averages over segments, and which are then approximately Gaussian distributed in the complex plane.

Results

Simulated data

An example epoch of the first simulated data and the power spectral density are depicted in the left column of Figure 5.3. The power spectral density highlights peaks at 10, 30, 40, and 50 Hz. Although our simulated data only contained two frequencies (i.e., 10 and 40 Hz), the two side peaks at 30 and 50 Hz were introduced due to the 40-Hz modulation. To be able to identify PAC, at least one of these two side frequencies must be included in the filtered signal of the amplitude component.

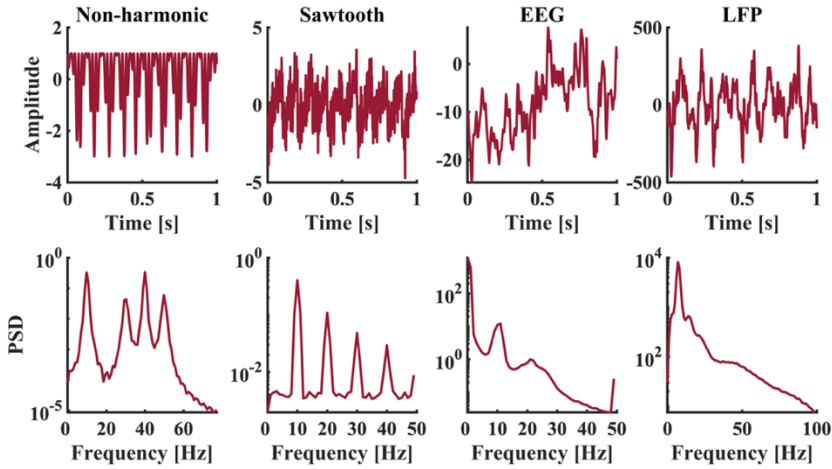


Figure 5.3 – Temporal and spectral characteristics of the simulated signals (non-harmonic and sawtooth signals), empirical electro-encephalographic (EEG), and empirical local field potential (LFP) data. The upper row depicts example epochs of the time series. The lower row reveals the power spectral density (PSD) of the signals.

Figure 5.4 reveals the core of our argumentation why the filter bandwidth of the amplitude component should not be twice as large as the frequency of the phase component. The left panel of Figure 5.4A depicts PAC as a function of the frequency of the amplitude component (abbreviated as f_2^2) and the bandwidth used for its filter (f_W). In this representation, the frequency of the phase component (f_1) was fixed to 10 Hz. No PAC is observed when f_W is smaller than 10 Hz. At an f_W of 10 Hz, two coupling peaks appear around 35 and 45 Hz. Increasing f_W further leads to smearing of both peaks and eventually to a merge of the two peaks when f_W approaches 20 Hz. In fact, the mere reason why PAC at 40 Hz can be observed is because the peaks at 35 and 45 Hz merge together. The right-hand representation of Figure 5.4 reveals the statistical ratio between the real and surrogate coupling (as defined in Eq. 5.28). We recall that p -values can be derived from this ratio by taken $p = \exp(-ratio)$.

Another way to show PAC's tendency to smear is by presenting PAC as a function of the frequencies f_1 and f_2 for various f_W . When f_2 is computed with an f_W that is twice as large as f_1 (i.e., ratio 2:1), a smeared PAC can be observed ranging from 30-50 Hz (left panel

² In the plots of PAC, we abbreviated the phase and amplitude frequency as f_1 and f_2 , respectively. Although we use f_1 and f_2 to abbreviate the frequencies of bicoherence as well, we would like to emphasise that these frequencies are based on different conventions.

of Figure 5.4B). Note that f_W would be 20 Hz when f_1 equals 10 Hz, meaning that the two side peaks at 30 and 50 Hz are included when PAC is computed at 40 Hz. If we, however, select f_W in a 1:1-ratio then PAC reveals the two peaks at 35 and 45 Hz while the PAC-peak centred around 40 Hz disappears (left panel of Figure 5.4C). For this filter setting, the side peak at either 30 or 50 Hz is included. PAC vanishes if f_W becomes substantially smaller than f_1 , which is shown for a 0:5-1-ratio (left panel of Figure 5.4D). The previously observed PAC at 40 Hz and the neighbouring peaks at 35 and 45 Hz disappear. Put differently, this f_W cannot include the dominant peak at 40 Hz and one of the side frequencies simultaneously. The latter result emphasises the pivotal role of including at least one of the side frequencies at 30 and 50 Hz in the estimation of PAC. The above-mentioned cross-frequency coupling results were confirmed by the ratio using surrogate statistics, which are provided in the right column of Figure 5.4. The reported statistical ratios correspond to significant coupling findings.



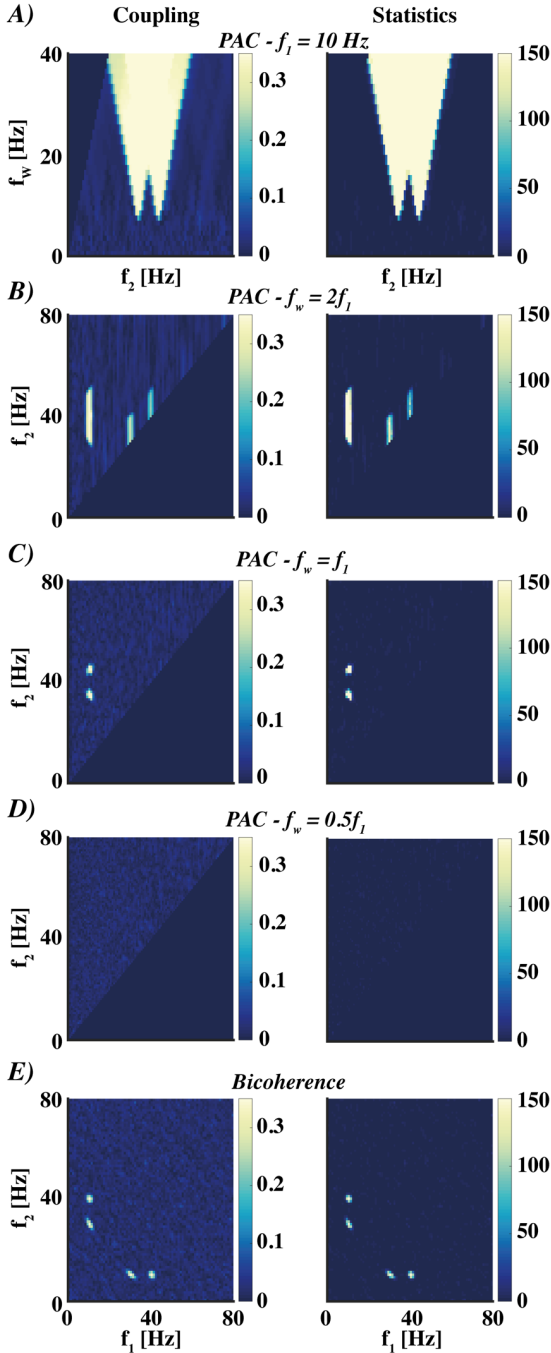


Figure 5.4 – Phase-amplitude coupling (PAC) and bicoherence in the non-harmonic simulated data. Left-hand plots represent the mean and right-hand plots the ratios between the actual cross-frequency coupling and surrogate datasets. (A) PAC as a function of the amplitude component (f_2) and its filter bandwidth (f_w). Here, the frequency of the phase component (f_1) was set to 10 Hz. This representation reveals that two peaks of PAC can be observed at a filter bandwidth of 10 Hz while a bandwidth of 20 Hz reveals a smeared version. (B–D) PAC as a function of the phase and amplitude component chosen a bandwidth that is double as large as ($2:1$ -ratio; $PAC - f_w = 2f_1$), equals ($1:1$ -ratio; $PAC - f_w = f_1$) or is half as large as ($0.5:1$ -ratio; $PAC - f_w = 0.5f_1$) the frequency of the phase component. The representations reveal a clear dependency of PAC on the filter bandwidth. (E) Bicoherence representation yielding significant cross-frequency coupling at 30 and 40 Hz. Cross-frequency coupling in bicoherence matches the PAC estimate comprising a bandwidth that equals the phase component frequency. PAC: phase-amplitude-coupling; f_w : filter width; f_1 : low frequency; f_2 : high frequency.

In the view of bicoherence, the observation of phase-amplitude coupling would be rather different compared to PAC (left panel of Figure 5.4E). The bispectrum is the third-order moment of the spectrum and measures the coupling between signals at three frequencies. Given the simulated data, two things could happen in terms of observing coupling between frequencies. There will be coupling between either 10, 30, and 40 Hz or 10, 40, and 50 Hz. In the bispectral analysis, bicoherence reveals most comparable results to the PAC estimated with a 1:1-ratio, except for a frequency shift of 5 Hz (i.e., 30 and 40 Hz for bicoherence versus 35 and 45 Hz for PAC). This frequency shift is due to a different convention for the meaning of the frequencies. For example, bicoherence with f_1 and f_2 chosen to be 10 and 30 Hz reveals coupling between 10, 30 and 40 Hz. A comparable finding for PAC can be observed with the filter for the high-frequency part centred at 35 Hz such that the lower and upper end of that filter, having a width of 10 Hz, include the rhythms at 30 and 40 Hz.

As mentioned earlier, the theory of section *Relations between Phase-Amplitude Coupling and bispectra* and *Settings the low- and high-frequency filters* specifically applies to PAC-forms expressed as a third-order statistical moment, however, the PAC-results of the simulated data as presented above were estimated with amplitude rather than power. The simulated data qualitatively reveal comparable results when estimating PAC with a high-frequency amplitude and power component. For empirical findings, our theory can essentially be used for unsquared versions of PAC as well. Yet, differences between both PAC-versions were found in the sawtooth simulation (i.e., our second set of simulated data), which are presented in Figure 5.5. An example time series and the power spectral density are depicted in the second column of Figure 5.3. Generally, PAC-results obtained in a 1:1-ratio are most comparable to bicoherence (middle row of Figure 5.5). While the squared version (i.e., power) still reveals non-smeared PAC, PAC slightly smears for the unsquared (i.e., amplitude) version (centre versus middle-right panels of Figure 5.5). Thus, although we found fairly comparable results for PAC between the squared and non-squared version in the non-harmonic simulation, the squared version of PAC better relates to bicoherence in the sawtooth simulation. PAC-estimates computed in a 2:1- and 0.5:1-ratio are comparable to the first simulation. For those filter settings, PAC is either smeared or non-existent, respectively.



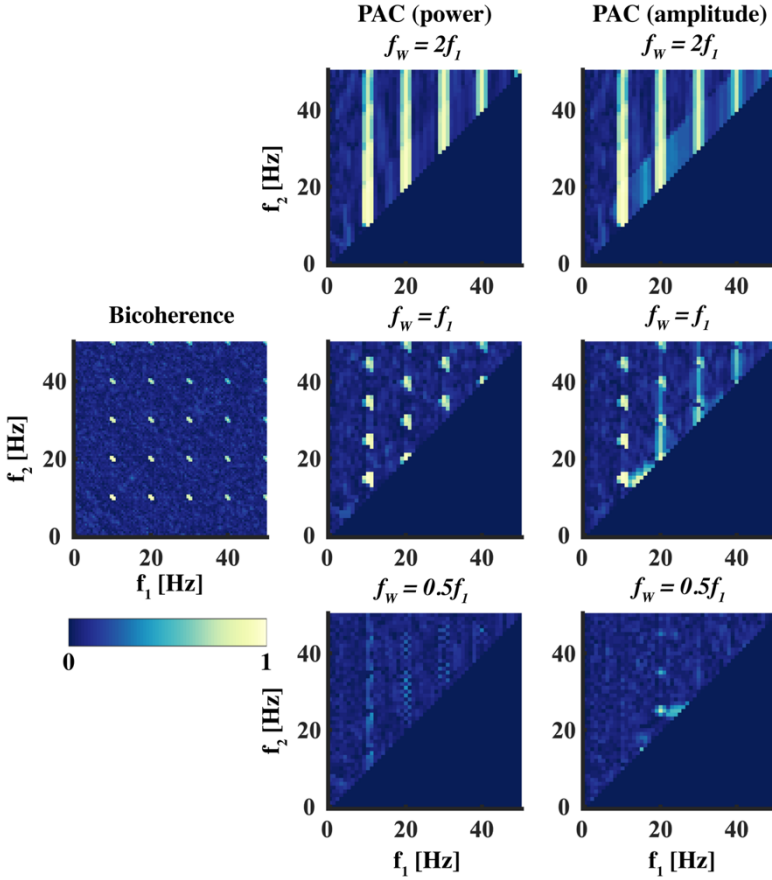


Figure 5.5 – Cross-frequency coupling of the simulated sawtooth time series. Coupling was estimated for bicoherence (left panel), phase-amplitude coupling (PAC) with a power component (PAC (power); middle column), and PAC with an amplitude component (PAC (amplitude); right column). Both versions of PAC are computed with a high-frequency component estimated in a 2:1- (upper row), 1:1- (middle row), and 0.5:1-ratio (lower row). PAC: phase-amplitude coupling; f_w : filter width; f_1 : low frequency; f_2 : high frequency.

Empirical electro-encephalographic data

The human EEG data yield highest power at the occipital channels at the alpha-band and its higher harmonics (see the third column of Figure 5.3). Like the simulated data, PAC estimated on the EEG data highlight clear dependency on f_w (left panel of Figure 5.6A). When f_1 is set constant to 10 Hz, two peaks appear at an f_w that is close to 10 Hz. Note that this would correspond to a 1:1-ratio between f_w and f_1 . It is hardly possible to identify two PAC peaks when f_w is below 10 Hz. Enlarging f_w above 10 Hz leads to an increased spectral

window in which we can observe significant PAC and the two coupling peaks get smeared out over a broader frequency range. This ultimately results in the merging of the two peaks around an f_w of 15 Hz. At this point the f_w only is 1.5 times as large as f_1 .

Such cross-frequency coupling patterns also emerge when representing PAC over f_1 and f_2 while defining f_w based on f_1 . The coupling is rather broadly smeared (i.e., roughly between 10 and 35 Hz) when the spectral representations are computed with an f_w of twice f_1 , the 2:1-ratio (left panel of Figure 5.6B). For such an f_w , which roughly equals 20 Hz when f_1 is 10 Hz, the two dominant frequencies at 10 and 30 Hz are included in the coupling. Hence, the inclusion of both frequencies results in a smeared version of PAC. Lowering f_w to a 1:1-ratio results in the emergence of multiple disentangled PAC peaks (left panel of Figure 5.6C). A focal PAC peak can be observed around 18 Hz with higher harmonics around 28 Hz. A combination of f_1 and f_2 equalling 10 and 18, and 10 and 28 Hz, respectively, results in the higher harmonics in the PAC plots. This emphasises the essential role of setting f_w in a 1:1-ratio when one is interested in phase-amplitude coupling in a small frequency band. The bandwidth size shrinkage following a change from a 2:1- to 1:1-ratio leads to PAC-modulation from broad-band smearing across a frequency band to multiple narrowed peaks. If f_w is narrowed even more to a 0.5:1-ratio, no PAC can be detected anymore (left panel of Figure 5.6D). Here, f_w is simply too narrow to include spectral content at dominant frequencies at an intermediate frequency.

Bicoherence spectrally identifies significant phase-amplitude coupling at the alpha rhythm, peaking at 11 Hz (left panel of Figure 5.6E). Bicoherence at this frequency can be observed when f_1 and f_2 are 11 Hz and $f_1 + f_2$ is constrained to be 22 Hz. As expected, the bicoherence peak at 11 Hz is much more prominent than the higher harmonics, which can be found at 22 Hz. To identify these higher harmonics for bicoherence, f_1 should equal 11 or 22 Hz with f_2 being the opposite. $f_1 + f_2$ is set to 33 Hz by default in both cases. Compared to the PAC-estimates, bicoherence spectrally localised separated peaks, which were evident in the PAC-estimates with a 1:1-ratio. Here again, bicoherence is therefore most comparable to the PAC-estimates with a filter bandwidth that equals the frequency of the phase component. The significance of such coupling is validated by surrogate analyses (right column of Figure 5.6).



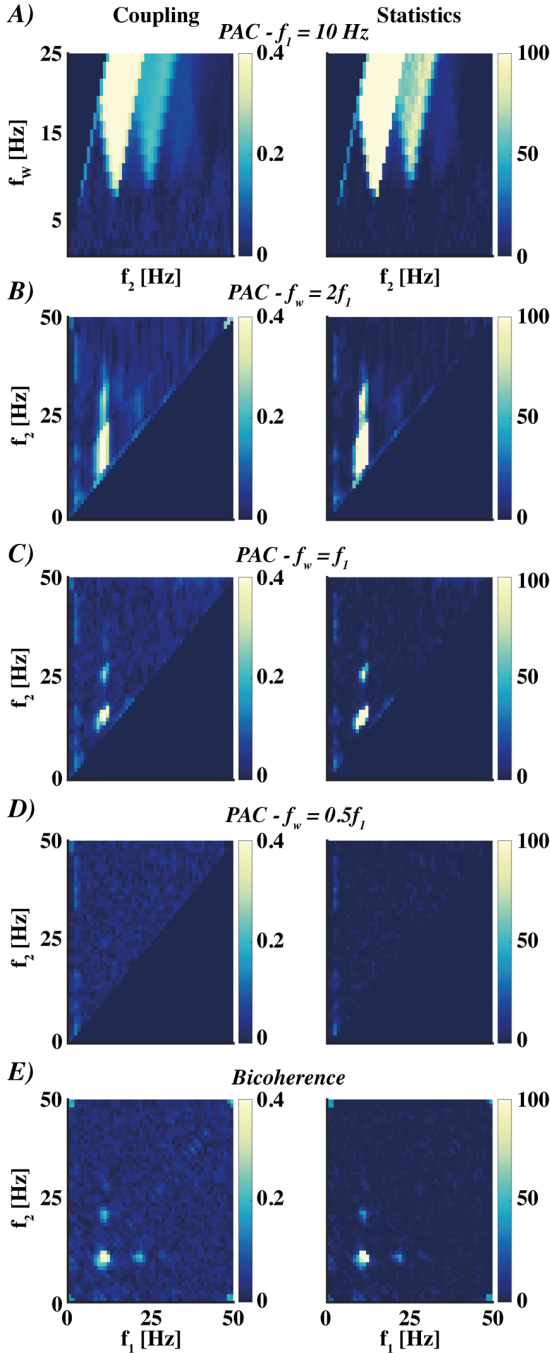


Figure 5.6 – Phase-amplitude coupling and bicoherence in the human electro-encephalographic data. Illustrative coupling estimates examples of the electro-encephalographic data of a single participant (channel 17 of subject 8). Left-hand plots represent the mean and right-hand plots the ratio statistics using the surrogate data. (A) Phase-amplitude coupling (PAC) as a function of the amplitude component (f_2) and its filter bandwidth (f_w). The low-frequency component was fixed at 10 Hz as this frequency corresponded to the power peak in the alpha range. (B-D) The PAC representations based on a broader (2:1-ratio; $PAC - f_w = 2f_1$), equalling (1:1-ratio; $PAC - f_w = f_1$), or narrowed (0.5:1-ratio; $PAC - f_w = 0.5f_1$) bandwidth underlines the importance of using filter settings in a 1:1-ratio. Here, the broad-band smearing results in merging multiple peaks. (E) Bicoherence spectrally localises the peaks 11 and 22 Hz like the PAC-estimates with a narrowed bandwidth. PAC: phase-amplitude coupling; f_w : filter width; f_1 : low frequency; f_2 : high frequency.

Empirical local field potential data

The LFP data yield theta-gamma coupling resembled between 4-8 and 40-100 Hz. An example time series and the power spectral density of the LFP data are depicted in fourth column of Figure 5.3. Like the simulation and EEG findings, coupling smearing across frequencies manifests in PAC when increasing f_W and fixating f_1 (left panel of Figure 5.7A). In this case f_1 was fixed to 7 Hz. When f_W roughly equals f_1 (i.e., the 1:1-ratio), two separated coupling peaks could be identified around 10 and 18 Hz. The coupling at higher frequencies (e.g., >40 Hz) is hardly affected by f_W and does not clearly smear when f_W is increased. When f_W is higher than the 1:1-ratio (i.e., higher than 7 Hz), a merging of the two low-frequency peaks appears at an f_W that is lower than twice f_1 . In the extreme case, the low- and high-frequency coupling converges into one broad frequency range of coupling when f_W is increased even further, for example, up to four times f_1 .

An f_W with a ratio of 2:1 to f_1 results in broadly-smeared low-frequency coupling from 10 to 25 Hz (left panel of Figure 5.7B). If f_W matches f_1 (i.e., the 1:1-ratio), peaks around 13 and 20 Hz can be recognised (left panel of Figure 5.7C). Likewise, bicoherence is able to localise these two low-frequency coupling peaks (left panel of Figure 5.7E). These peaks are around 9 and 16 Hz, and were found to an even larger extent by Sheremet et al., (2016) and Sheremet et al., (2019) where cross-frequency coupling was studied using bicoherence estimated from LFP data of the rat hippocampus.

For both PAC and bicoherence, and as displayed in Figure 5.7A, the coupling between 40 and 100 Hz does not depend on f_W and remains unchanged. This component only vanishes when PAC is estimated with a 0.5:1-ratio between f_W and f_1 (left panel of Figure 5.7D). Statistics between the actual and surrogate coupling reveals significant coupling for bicoherence and PAC estimated with the 2:1- and 1:1-ratio, as shown in the representations in the right column of Figure 5.7.



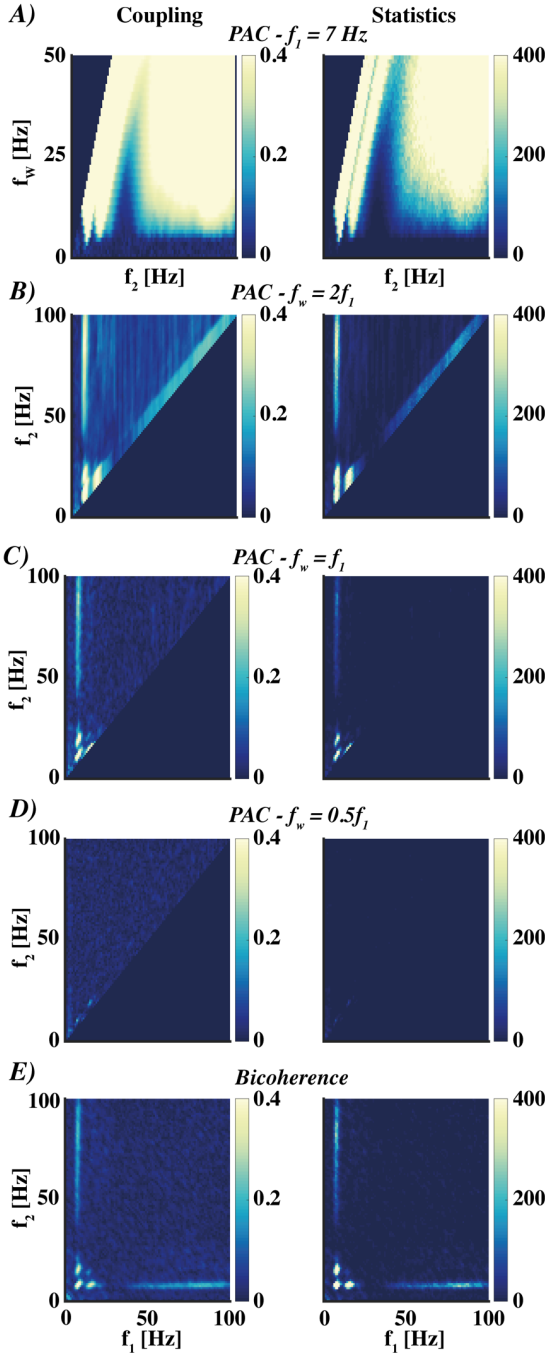


Figure 5.7 – Phase-amplitude coupling and bicoherence in the local field potentials data of rats. Illustrative examples of the coupling estimates of the local field potentials data of a single rat (channel 16 of rat 7). Left-handed plots represent the mean coupling. Right-handed representations show the statistics of the surrogate data (i.e., the ratios between the coupling and surrogate coupling). (A) Phase-amplitude coupling (PAC) that depends on (the bandwidth of) the high-frequency component (f_w) while the frequency of the low-frequency component is set constant. To do so, the bandwidth was fixed at 7 Hz (i.e., the frequency where most coupling was expected). (B-D) When the ratio between the phase component frequency and bandwidth of the amplitude component is set at a 2:1- ($PAC - f_w = 2f_1$), 1:1- ($PAC - f_w = f_1$), or 0.5:1-ratio ($PAC - f_w = 0.5f_1$), the (low-frequency) coupling reveals either smeared, non-smeared or non-existent PAC. The 1:1-ratio PAC establishes two low-frequency coupling peaks. (E) These cross-frequency coupling peaks are also accurately identified by bicoherence. PAC: phase-amplitude-coupling; f_w : filter width; f_1 : low frequency; f_2 : high frequency.

Conclusion

Much of the brain's dynamics is related to nonlinear neural activity. Cross-frequency coupling measures are sensitive to identify such neural processes. Here, we evaluated the phenomenon of phase-amplitude coupling from a bispectral point of view.

Our main theoretical finding is that PAC and bispectra are not only related but are literally equivalent for an appropriate choice of the filter to estimate the high-frequency amplitude, and even then PAC is just a special case of bicoherence. As a mathematical result, this finding is an idealisation, and there can still be rather minor deviations in practice for several reasons which we would like to summarise:

- We have shown the equivalence for PAC and bispectra for infinite frequency resolution, but frequency resolutions are finite in practice with details depending on the implementations.
- Equivalence is shown when PAC can be expressed as a third-order statistical moment, which requires that the low-frequency phase is weighted by the low-frequency amplitude. This is not the case in the PAC version presented in Eq. 5.1 where the Hilbert transformed signal for the low frequency was normalised to unit amplitude, but it is the case for the approach of Osipova et al. (2008) where PAC is defined by coherence. Expressing PAC as a third-order statistical moment also requires that the coupling to the squared amplitude is studied rather than the amplitude itself. Here, we have only used the squared version of the amplitude component in the example of the simulated sawtooth data.
- Mathematical relations refer only to the numerators of the coupling measures, i.e., the bispectra. However, we found in empirical studies that the normalisations do not affect the principal finding.

Our own implementation of PAC, i.e., coherence between signal and high-frequency amplitude at some low frequency, deviated from the above idealisation with regard to all three aspects. We still found that results for PAC and bicoherence are always very similar using a proper choice of filters for the calculation of PAC.

From these findings we can derive some recommendations how to choose filters for the calculation of PAC. When cross-frequency phase-amplitude interactions are estimated with PAC, filter settings substantially affect the coupling. Although it is already well



established that the use of adequate filter bandwidths is critical to estimate PAC accurately (Aru et al., 2015; Berman et al., 2012), there is no consensus in terms of the optimal filter settings. A recent study recommended to have the bandwidth of the amplitude component at least double as large as the low-frequency component (Aru et al., 2015). Here, we showed that this recommendation is not trivial from a bispectral perspective. In particular, such filter settings hamper coupling estimation when one is interested in neural dynamics within a narrowed frequency range. As revealed by both simulation and empirical findings, phase-amplitude coupling across frequencies is evident in both PAC and bicoherence estimates. However, as expected, the PAC dynamics were clearly modulated as a function of the filter settings (i.e., the bandwidth of the amplitude component). Specifically, we show that the frequency range over which significant PAC can be observed decreases when the bandwidth of the high-frequency component decreases. PAC-estimations comprising a bandwidth that is twice as large as the low-frequency component results in smearing of the phase-amplitude coupling over a broad frequency range. In other words, the spectral resolution of PAC substantially decreases when taking a bandwidth of the amplitude component that is too large. It then becomes difficult to distinguish wide-band phenomena from higher harmonics. Bicoherence and PAC provide comparable results in case the bandwidth of the amplitude component is narrowed to match the frequency of the phase component. When the bandwidth of the amplitude component decreases even further, the likelihood that carrier frequencies are not included increases, meaning no PAC can be observed at all.

A further advantage of bicoherence over PAC is that the filtering of the phase and amplitude component at many isolated frequencies and frequency bands makes the estimation of PAC computationally heavy. In particular, the computation of a sufficient number of surrogate data during statistical assessments is time-demanding. In contrast, bicoherence is based on the fast Fourier transforms at three isolated frequencies. The latter, therefore, has the advantage that there is no necessity to filter signals before coupling estimation. We conclude that, although PAC and bicoherence are measures to estimate cross-frequency phase-amplitude coupling, bicoherence has the advantage that it does not have to be estimated with additional pre-processing steps. Likewise, the filter settings of PAC's amplitude component bandwidth should be chosen with precaution and should be equal to the frequency of the low-frequency (i.e., the phase) component. This is especially true for neural rhythms operating in narrow frequency bands.



CHAPTER 6

Epilogue



Posture, balance, and locomotion are often seen as easy tasks, arguably because in many circumstances we can perform them with little effort. Nevertheless, our central nervous system is heavily involved in generating and controlling them. The spinal cord distributes neural activity to motoneuron pools indicating its modular organisation. Much of this neural activity stems from the cortical motor network and passes several subcortical structures, at least in parts, before eliciting spinal modules. I approached the modular organisation via muscle synergies. Muscle synergies are believed to be accommodated in spinal premotor interneuron circuitries, imposing temporal activation profiles on groups of muscles. Despite considerable research into muscle synergies, there are many unanswered questions, some of which I sought to answer in this thesis.

The cortico-spinal tract connects the motor cortex and spinal cord. It is the major pathway for cortico-muscular communication in the majority of species despite their phylogenetical differences. In humans, motor cortical influences are particularly pronounced (Capaday, 2002). The overarching research question I addressed in my thesis was: How does the cortical motor activity contribute to muscle synergies in the context of locomotion, balance and posture? In these three tasks, I assessed spectral correlations between muscle synergy patterns and cortical activity. This entailed a novel analysis of cortico-synergy coherence, which quantifies phase locking between neural oscillations in the cortical motor network and in muscle synergies. Cortico-synergy coherence was first introduced in **Chapter 2** and applied to data collected during a postural control task. This study revealed prominent coherence signatures when reconstructing broad-band temporal activities of the muscle synergies that are employed in the task. Interestingly, next to the motor-related beta-frequency band, the cortico-synergy coherence was task-modulated in the Piper rhythm, a high-frequency component known for its association with multisensory integration.

In the studies summarised in **Chapters 3 and 4**, I applied cortico-synergy coherence to data collected during locomotion. There, I demonstrated that the involved muscle synergies can be discriminated as ones that are coherent with cortical activity and others that are not coherent. More specifically, in groups of toddlers and adults, only two out of four locomotor synergies showed activity that was synchronous with activity in the motor cortex, in particular, in the beta-frequency band. These synergies are dominant during the double support phases in the gait cycle. While both age groups displayed this two-by-two synergy partitioning with statistical significance, it seemed that the two cortical synergy

representations develop further with maturity, an observation on which I will elaborate on further below.

While iso-frequency coherence did (and does) allow for identifying and discriminating cortical contributions to muscle synergies, one has to realise that at least two frequency bands appeared relevant in the motor tasks employed in this thesis. This triggered my work on cross-frequency functional connectivity in **Chapter 5**. There, I showed that both bicoherence and PAC can capture multi-frequency coupling between low-frequency phases and high-frequency amplitudes. As such, both measures have the capacity for quantifying functional coupling of the cortico-spinal drive. Below I will provide a glimpse on how these measures may enter future studies on the contribution of motor cortex in the muscle synergy organisation.

Revisiting the research questions

Q1. How does the motor cortex contribute to muscle synergies during the generation and maintenance of locomotion, posture, and balance?

The cortico-spinal axis may constitute segregated loops to broadcast activity at motor-related frequencies to muscle synergies at the spinal cord. According to a model of Aumann and Prut (2015), the motor cortex projects to different synergies via distinct loops; however, they can be combined to support the control of complex movements. Support for the existence of cortico-synergy loops comes from the close associations between the phase shifts of beta oscillations and the conduction times based on rhythmic discharges of neuronal populations (Cheney & Fetz, 1984; Witham et al., 2011). In this sense, cortico-synergy pathways exploit the cell-intrinsic features to form an efficient network for the propagation of neural oscillations (Aumann & Prut, 2015). If true, the motor cortex can essentially activate the spinal layers accommodating the muscle synergies by single neural commands.

Starting with my findings on a postural control task, it seems that cortico-synergy coherence is prominent not only for beta-band oscillations but also in the Piper rhythm. This dual-band coherence was particularly apparent for the muscle synergy consisting of muscles that are primarily involved in mediolateral balance control (i.e., tibialis anterior, peroneus longus, adductor longus, and gluteus medius).



A similar pattern appears during walking; however, two locomotor synergies display strong coherence with the cortex while two others rely on subcortical activities. The two synergies that are coherent with the motor cortex are both active during the double support phases (see Figures 3.1-3.2 and 4.2-4.3). Apparently, the two double support phase synergies exchange synchronous neural activity with the motor cortex while the two single support phase synergies do not (Figure 4.4).

Of course, this raises the question of why cortico-synergy beta-band coherence is limited to the double support phases. From a biomechanical point of view, the most stable gait phases are the periods when both feet are in contact with the ground, i.e., during double support, because the body's centre of mass is mostly inside the base of support and switches from the ipsilateral to contralateral leg (Bruijn & Van Dieën, 2018). One may argue that, hence, the corresponding muscle synergies play a role in the balance control during locomotion. In a neurophysiological sense, assuming gait is unstable during the single support phases (i.e., the body's centre of mass is outside the base of support), super-spinal centres can exert control on the legs when both feet are in contact with the ground. Here, I would like to note that the association between cortical beta-band oscillations and stabilising gait has been suggested before (Bruijn et al., 2015). Yet, it remains to be seen how beta-band oscillations are involved in the balance control of gait rather than in gait stability per se.

Interestingly, the coherent firing of neural populations is not limited to the interaction between cortex and (groups of) motor unit pools/motor synergies. Recent studies on so-called muscle networks suggest that functional, anatomical, and neural connectivity shapes synchronised muscle activity and induces a modular control structure (Kerkman et al., 2018; Kerkman et al., 2022). As such it seems that neural synchronisation – in particular in the two frequency ranges highlighted in my thesis – is at the heart of the neural communication needed to control posture and movements, be that between muscles or between cortex and synergies.

Q2. How do the locomotor muscle synergies and their interaction with the motor cortex develop? Specifically, does the interaction differ between toddlers and adults?

In neonatal stepping, the corresponding EMG waveforms can be factorised into two synergies with patterns that are active during the two single support phases (Dominici et al., 2011). When a toddler walks independently, describing the corresponding EMG requires a set of four synergies. It appears that the synergies of neonatal stepping are supplemented by two new muscle synergies that are timed to the double support phases (Dominici et al., 2011). I showed that the two synergies comparable to the emerging synergies in toddlers were indeed the ones displaying significant beta-band coherence with cortical activity.

This led to the yet-to-be-proven theory that this set of synergies emerges because of development-related changes in the cortex and cortico-spinal tract. I tested this two-on-two grouping of the muscle synergies in independently walking toddlers. As hypothesised, the two muscle synergies with patterns active during the double support phases again revealed significant beta-band coherence. Even in toddlers with only six months of independent walking experience, beta-band signatures are evident in the two emerging synergies. The cortico-synergy coherence and these two synergies may ensure that toddlers can successfully bring their feet in contact with the ground and walk. Toddlers are able to control and lower their foot to get it in contact with the ground (Yang & Gorassini, 2006), while this is absent in the immature walking pattern of neonates (Yang et al., 2004). In the latter, the corresponding EMG patterns are characterised by two single support phase synergies (Dominici et al., 2011). In adult walking, several earlier reports suggested a profound role for the motor cortex in dorsiflexor muscles in the leg, since they are important for foot contact with the ground (Capaday et al., 1999; Petersen et al., 2001). Taken together, one may speculate that the emerging cortico-synergy coherence supports foot-ground contact.



I further investigated the differences in cortico-synergy coherence between toddlers and adults. The coherence sources at the cortex spatially shifted from sensorimotor and parietal areas in toddlers to premotor and primary motor areas in adults. This implies that the cortical synergy representations undergo reorganisations before being matured in adults. Possibly, the neural activity that interacts with the muscle synergies gets generated by different cortical regions. Moreover, the beta-band coherence burst at the double support

phases became more focal in time in adults. That is, the neural circuitries encompassing the cortico-spinal tract also develop further by means of structural and functional reorganisations (Eyre et al., 2000). Arguably because of that, individual muscle contributions to these patterns become more pronounced (Ivanenko et al., 2013), and the number of muscles that contribute gets sparser (Dominici et al., 2011).

Q3. How can we assess the functional connectivity across different frequencies?

By now it is evident that cortico-synergy coherence occurs at beta- and Piper-band frequencies in walking and in postural control, respectively. Does this mean that the 20-Hz oscillations during the double support phases interact with the 40-Hz oscillations involved in balance regulation? Conventional coherence estimates will fall short in answering this because they are limited to iso-frequency comparison between oscillating units. Therefore, I devoted one chapter to bicoherence and PAC and showed that bicoherence does not depend on further methodological choices (e.g., filter settings) that dramatically influence the results. The latter are essential for disentangling interactions in the aforementioned frequency bands. Given this promising finding, one may wonder why bicoherence did not enter my data analysis pipeline. After all, constraining two of the three frequencies in bicoherence to beta and Piper frequencies can be readily realised. However, further steps are needed to use it in the context of EEG-source localisation by means of DICS-beamforming. The bicoherence must be maximised at brain sources and one must construct sets of spatial filters, a step that went beyond the scope of this thesis but will certainly be addressed in future work. Ultimately, this methodological advance will help to clarify whether beta and Piper rhythms interact to maintain balance while walking independently.

Future experimental outlooks

While the cross-sectional comparison for toddlers and adults geared profound ideas about development-related changes of coherence between the motor cortex and locomotor synergies, further support for my conclusions will require assessments along a longitudinal design covering the early development of independent walking. As a matter of fact, in the course of my doctoral project we already generated preliminary results from 25 babies that were measured in a longitudinal study at a maximum of four timepoints: Babies visited the lab at five months of age, ten months of age, their first steps and six months after their first steps. First steps sessions were recorded within two weeks after a child was able to walk for four or more consecutive strides without the need of any physical support. As in Chapter 4, four muscle synergies were extracted at every timepoint, with two of them active during single support and resembling the ones during neonate stepping. Next to these *congenital* synergies the other two *supplementary* ones were active during double support and expectably emerged at later timepoints. General linear mixed-effects models evaluated over the mean responses of the corresponding cortico-synergy beamformers across synergy types and timepoints supported this. The *Primitive*Timepoint* interaction revealed a distinct development for the cortical representations of the two synergy sets (Figure 6.1A). Coherences with the congenital synergies remained constant over the course of the development. While the coherence of the supplementary synergies was comparable to the congenital ones for the first two timepoints before the first independent steps, it increased for the two later timepoints. The cortical source associated with the *Primitive*Timepoint* interaction appeared to be located at the sensorimotor cortex (Figure 6.1A). This suggests that coherence between the sensorimotor cortex and supplementary synergies increases when a toddler is able to make its first steps. The coherence increase found around the first steps was also reflected in the *Timepoint* main effect (Figure 6.1B). Also there, the cortical source was primarily located at the sensorimotor cortex (Figure 6.1B). Although these are preliminary source localisation results, they do indicate that the first independent steps are accompanied by an increase in beta-band coherence (Figure 6.1B) and specifically apply to the supplementary (emerging) synergies (Figure 6.1A).



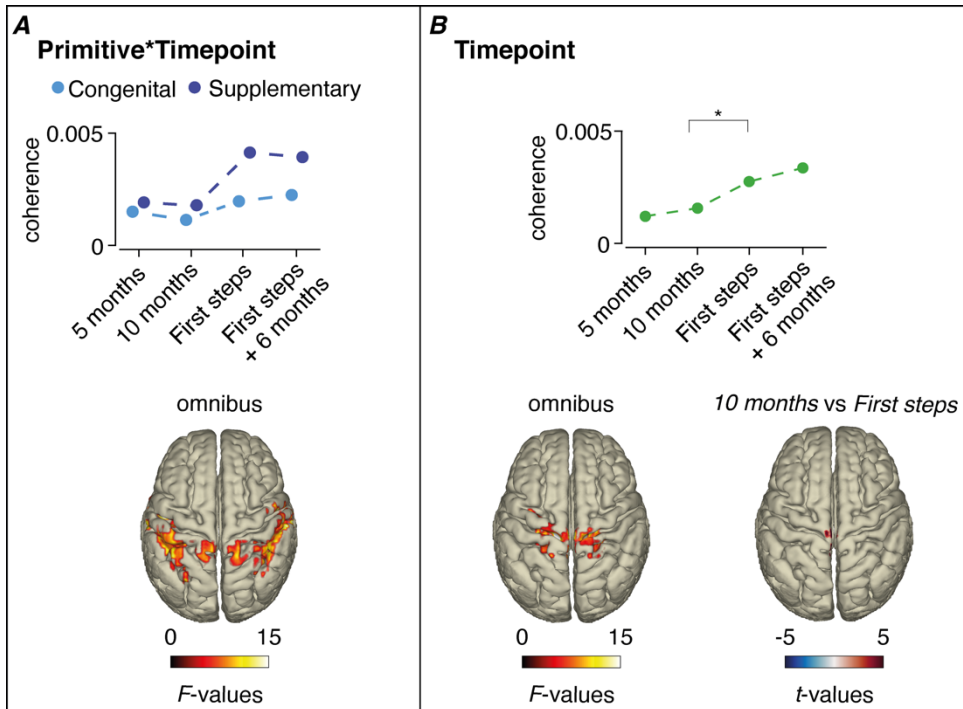


Figure 6.1 – The synergy-dependent development of the beta-band coherence-based beamformers. (A) Two-way interaction *Primitive*Timepoint* describing the development of the ‘Congenital’ and ‘Supplementary’ muscle synergy sets for the four timepoints (‘5 months’, ‘10 months’, ‘First steps’ and ‘First steps + 6 months’). Circles represent group averages and are averaged coherence of the voxels that yielded the significant effect. The test-statistic of the cortical source of the significant interaction is projected on the cortical surface. All statistical models are evaluated with an alpha-level of 0.01 corrected for false discovery rate. (B) Mean coherences for the main effect ‘Timepoint’ across the four age groups independent of synergy type. Mean differences were particularly apparent between the 10 months and First steps as identified by the post-hoc assessments. This figure is adapted and modified from a manuscript that will be submitted to a scientific journal.

Given advances in neuro-imaging technologies over the last ten years, one can also consider incorporating optically pumped magnetometers (OPM-MEG) and high-density electromyography (HD-EMG) to further improve the spatial accuracy of the cortical areas and spinal cord, respectively. Compared to EEG, OPM-MEG has the advantage that magnetic signals are not distorted by head tissues (Boto et al., 2018). Although still associated with high financial costs, recent studies identified its potential in the use of dynamical movement paradigms (Mellor et al., 2021; Seymour et al., 2021). At the spinal level, HD-EMG in combination with blind source separation methods allows for reconstruction of motoneuronal activity and may therefore improve the spatial resolution to identify functional modular networks at the spinal cord (Del Vecchio et al., 2020; Hug et al.,

2021). HD-EMG has been combined with the EEG-activity (Ibanez et al., 2021), yet, study designs have been limited to single muscle assessments so far. Taken together, the implementation of these experimental and methodological outlines and potential combinations of them will bring us one step closer to decipher how muscle synergies are organised within the cortex, and in the central nervous system in general.

Limitations

In this thesis, coherence served as a prime vehicle to infer cortico-synergy interaction. Coherence can be viewed as a correlation measure as a function of frequency. As such, it does not provide any information about the direction of coupling. There are several reports that cortical oscillations precede those at the peripheral muscles (Mima & Hallett, 1999a; Rosenberg et al., 1998). Yet, the estimation of directionality and verification of the corresponding time delays from macroscopic recordings is all but trivial, often leading to unrealistic values that could not be expected based on the system's neurophysiological properties. In two seminal papers, Baker and co-workers (2003, 2005) revealed that cortico-muscular coherence most likely intertwines efferent and afferent components. First, in a neuropharmacological study, local beta-band synchrony is enhanced at the motor cortex by diazepam – a drug increasing the size of inhibitory postsynaptic potentials (Baker & Baker, 2003). However, the modulation of the coherence spectra was not a mere scaling of the auto spectra, emphasising that neural oscillations are not unidirectionally transmitted along the cortico-spinal axis. Second, when cooling the forearm the time delay obtained from the phase of beta-band coherence is significantly larger than the time delay as measured with stimulation responses (Riddle & Baker, 2005). It is hence unlikely that the beta-band synchrony is just a reflection of efferent pathways.



Concluding remarks

How does the motor cortex interact with muscle synergies?

Muscle synergies can be viewed as muscle ensembles that are grouped based on spatiotemporal regularities (d'Avella et al., 2003). Experimental assessments of muscle synergies usually rely on multi-muscular recordings of EMG waveforms that are decomposed based on their co-activations. This approach helped the motor neuroscience community to gain insight into the modular organisation of the spinal cord during coordinated movements. This does not mean however that the unravelling of the neural basis of muscle synergies within the central nervous system has become easy (Cheung & Seki, 2021).

Using simultaneous EEG- and EMG-recordings and a combination of two main analysis techniques – muscle synergies and cortico-muscular coherence – I provided support that signatures of cortical activity are embedded in the muscle synergy patterns or vice versa. These signatures appear at beta- and Piper-band oscillations. Cortical areas communicate in the beta- and Piper-frequency band with interneuronal and motoneuronal populations at the spinal cord, and afferent pathways project back to the spinal cord and sensory cortex. The functional relevance was evident when generating and maintaining locomotion, balance, and posture.

The cortico-synergy coherence findings are the first steps into a theoretical framework of the disentanglement of neural processes governing muscle synergies. Looking forward, many novel research questions await answers including longitudinal assessments of the emergence of cortical-synergy coupling and applications of cross-frequency coupling methods. My findings on cortico-synergy coherence are merely a humble steppingstone towards deciphering the full neural basis of muscle synergies.



BIBLIOGRAPHY



- Allen, M., & Capute, A. (1986). The evolution of primitive reflexes in extremely premature infants. *Pediatric Research*, 20(12), 1284-1289
- Aru, J., Aru, J., Priesemann, V., Wibral, M., Lana, L., Pipa, G., Singer, W., & Vicente, R. (2015). Untangling cross-frequency coupling in neuroscience. *Current Opinion in Neurobiology*, 31, 51-61
- Ashburner, J., & Friston, K. J. (2005). Unified segmentation. *Neuroimage*, 26(3), 839-851
- Aumann, T. D., & Prut, Y. (2015). Do sensorimotor β -oscillations maintain muscle synergy representations in primary motor cortex? *Trends in Neurosciences*, 38(2), 77-85
- Baillet, S., Mosher, J. C., & Leahy, R. M. (2001). Electromagnetic brain mapping. *IEEE Signal Processing Magazine*, 18(6), 14-30
- Baker, M., & Baker, S. (2003). The effect of diazepam on motor cortical oscillations and corticomuscular coherence studied in man. *The Journal of Physiology*, 546(3), 931-942
- Baker, S. (2007). Oscillatory interactions between sensorimotor cortex and the periphery. *Current Opinion in Neurobiology*, 17(6), 649-655
- Baker, S., Kilner, J., Pinches, E., & Lemon, R. (1999). The role of synchrony and oscillations in the motor output. *Experimental Brain Research*, 128(1), 109-117
- Banks, C. L., Pai, M. M., McGuirk, T. E., Fregly, B. J., & Patten, C. (2017). Methodological choices in muscle synergy analysis impact differentiation of physiological characteristics following stroke. *Frontiers in Computational Neuroscience*, 11, 78
- Bartz, S., Avarvand, F. S., Leicht, G., & Nolte, G. (2019). Analyzing the waveshape of brain oscillations with bicoherence. *Neuroimage*, 188, 145-160
- Berger, D. J., Masciullo, M., Molinari, M., Lacquaniti, F., & d'Avella, A. (2020). Does the cerebellum shape the spatiotemporal organization of muscle patterns? Insights from subjects with cerebellar ataxias. *Journal of Neurophysiology*, 123(5), 1691-1710
- Berman, J. I., McDaniel, J., Liu, S., Cornew, L., Gaetz, W., Roberts, T. P., & Edgar, J. C. (2012). Variable bandwidth filtering for improved sensitivity of cross-frequency coupling metrics. *Brain Connectivity*, 2(3), 155-163
- Bernstein, N. (1967). *The co-ordination and regulation of movements*. Oxford: Pergamon Press.
- Berry, M. W., Browne, M., Langville, A. N., Pauca, V. P., & Plemmons, R. J. (2007). Algorithms and applications for approximate nonnegative matrix factorization. *Computational Statistics & Data Analysis*, 52(1), 155-173
- Biro, G., Spinelli, L., Vulli  moz, S., M  gevand, P., Brunet, D., Seeck, M., & Michel, C. M. (2014). Head model and electrical source imaging: a study of 38 epileptic patients. *NeuroImage: Clinical*, 5, 77-83
- Bizzi, E., & Cheung, V. C. (2013). The neural origin of muscle synergies. *Frontiers in Computational Neuroscience*, 7, 51
- Bizzi, E., Cheung, V. C., d'Avella, A., Saltiel, P., & Tresch, M. (2008). Combining modules for movement. *Brain Research Reviews*, 57(1), 125-133
- Boonstra, T. W., & Breakspear, M. (2012). Neural mechanisms of intermuscular coherence: implications for the rectification of surface electromyography. *Journal of Neurophysiology*, 107(3), 796-807
- Boonstra, T. W., van Wijk, B. C. M., Praamstra, P., & Daffertshofer, A. (2009). Corticomuscular and bilateral EMG coherence reflect distinct aspects of neural synchronization. *Neuroscience Letters*, 463(1), 17-21
- Boto, E., Holmes, N., Leggett, J., Roberts, G., Shah, V., Meyer, S. S., Mu  oz, L. D., Mullinger, K. J., Tierney, T. M., & Bestmann, S. (2018). Moving

- magnetoencephalography towards real-world applications with a wearable system. *Nature*, 555(7698), 657-661
- Brookes, M. J., Vrba, J., Robinson, S. E., Stevenson, C. M., Peters, A. M., Barnes, G. R., Hillebrand, A., & Morris, P. G. (2008). Optimising experimental design for MEG beamformer imaging. *Neuroimage*, 39(4), 1788-1802
- Brown, P. (2000). Cortical drives to human muscle: the Piper and related rhythms. *Progress in Neurobiology*, 60(1), 97-108
- Brown, P., Salenius, S., Rothwell, J. C., & Hari, R. (1998). Cortical correlate of the Piper rhythm in humans. *Journal of Neurophysiology*, 80(6), 2911-2917
- Brown, T. (1911). The intrinsic factors in the act of progression in the mammal. *Proceedings of the Royal Society of London. Series B, containing papers of a biological character*, 84(572), 308-319
- Brown, T. (1914). On the nature of the fundamental activity of the nervous centres; together with an analysis of the conditioning of rhythmic activity in progression, and a theory of the evolution of function in the nervous system. *The Journal of Physiology*, 48(1), 18-46
- Bruijn, S. M., & Van Dieën, J. H. (2018). Control of human gait stability through foot placement. *Journal of The Royal Society Interface*, 15(143), 20170816
- Bruijn, S. M., Van Dieën, J. H., & Daffertshofer, A. (2015). Beta activity in the premotor cortex is increased during stabilized as compared to normal walking. *Frontiers in Human Neuroscience*, 9, 593
- Bruns, A. (2004). Fourier-, Hilbert- and wavelet-based signal analysis: are they really different approaches? *Journal of Neuroscience Methods*, 137(2), 321-332
- Canolty, R. T., Edwards, E., Dalal, S. S., Soltani, M., Nagarajan, S. S., Kirsch, H. E., Berger, M. S., Barbaro, N. M., & Knight, R. T. (2006). High gamma power is phase-locked to theta oscillations in human neocortex. *Science*, 313(5793), 1626-1628
- Capaday, C. (2002). The special nature of human walking and its neural control. *Trends in Neurosciences*, 25(7), 370-376
- Capaday, C., Lavoie, B. A., Barbeau, H., Schneider, C., & Bonnard, M. (1999). Studies on the corticospinal control of human walking. I. Responses to focal transcranial magnetic stimulation of the motor cortex. *Journal of Neurophysiology*, 81(1), 129-139
- Cheney, P., & Fetz, E. (1984). Corticomotoneuronal cells contribute to long-latency stretch reflexes in the rhesus monkey. *The Journal of Physiology*, 349(1), 249-272
- Cheney, P., & Fetz, E. (1985). Comparable patterns of muscle facilitation evoked by individual corticomotoneuronal (CM) cells and by single intracortical microstimuli in primates: evidence for functional groups of CM cells. *Journal of Neurophysiology*, 53(3), 786-804
- Cheng, N., Li, Q., Xu, X., & Zhang, T. (2016). A precise annotation of phase-amplitude coupling intensity. *PLoS One*, 11(10), e0163940
- Cheng, R., Sui, Y., Sayenko, D., & Burdick, J. W. (2019). Motor control after human SCI through activation of muscle synergies under spinal cord stimulation. *IEEE Transactions on Neural Systems and Rehabilitation Engineering*, 27(6), 1331-1340
- Cheung, V. C., Cheung, B. M., Zhang, J. H., Chan, Z., Ha, S. C., Chen, C.-Y., & Cheung, R. T. (2020). Plasticity of muscle synergies through fractionation and merging during development and training of human runners. *Nature Communications*, 11(1), 1-15
- Cheung, V. C., & Seki, K. (2021). Approaches to revealing the neural basis of muscle synergies: a review and a critique. *Journal of Neurophysiology*, 125(5), 1580-1597



- Cheung, V. C., & Tresch, M. C. (2006). Non-negative matrix factorization algorithms modeling noise distributions within the exponential family. 2005 IEEE Engineering in Medicine and Biology 27th Annual Conference,
- Clark, D. J., Ting, L. H., Zajac, F. E., Neptune, R. R., & Kautz, S. A. (2009). Merging of healthy motor modules predicts reduced locomotor performance and muscle coordination complexity post-stroke. *Journal of Neurophysiology*, 103(2), 844-857
- Conway, B., Halliday, D., Farmer, S., Shahani, U., Maas, P., Weir, A., & Rosenberg, J. (1995). Synchronization between motor cortex and spinal motoneuronal pool during the performance of a maintained motor task in man. *The Journal of Physiology*, 489(3), 917-924
- d'Avella, A., Saltiel, P., & Bizzi, E. (2003). Combinations of muscle synergies in the construction of a natural motor behavior. *Nature Neuroscience*, 6(3), 300-308
- Danner, S. M., Hofstoetter, U. S., Freundl, B., Binder, H., Mayr, W., Rattay, F., & Minassian, K. (2015). Human spinal locomotor control is based on flexibly organized burst generators. *Brain*, 138(3), 577-588
- Dayan, E., & Cohen, L. G. (2011). Neuroplasticity subserving motor skill learning. *Neuron*, 72(3), 443-454
- de Vries, I. E., Daffertshofer, A., Stegeman, D. F., & Boonstra, T. W. (2016). Functional connectivity in the neuromuscular system underlying bimanual coordination. *Journal of Neurophysiology*, 116(6), 2576-2585
- Del Vecchio, A., Sylos-Labini, F., Mondì, V., Paolillo, P., Ivanenko, Y., Lacquaniti, F., & Farina, D. (2020). Spinal motoneurons of the human newborn are highly synchronized during leg movements. *Science Advances*, 6(47), eabc3916
- Desrochers, E., Harnie, J., Doelman, A., Hurteau, M. F., & Frigon, A. (2019). Spinal control of muscle synergies for adult mammalian locomotion. *The Journal of Physiology*, 597(1), 333-350
- Dimitrijevic, M. R., Gerasimenko, Y., & Pinter, M. M. (1998). Evidence for a spinal central pattern generator in humans. *Annals of the New York Academy of Sciences*, 860(1), 360-376
- Dominici, N., Ivanenko, Y. P., Cappellini, G., d'Avella, A., Mondì, V., Cicchese, M., Fabiano, A., Silei, T., Di Paolo, A., & Giannini, C. (2011). Locomotor primitives in newborn babies and their development. *Science*, 334(6058), 997-999
- Drew, T., Andujar, J.-E., Lajoie, K., & Yakovenko, S. (2008). Cortical mechanisms involved in visuomotor coordination during precision walking. *Brain Research Reviews*, 57(1), 199-211
- Engel, A. K., & Fries, P. (2010). Beta-band oscillations—signalling the status quo? *Current Opinion in Neurobiology*, 20(2), 156-165
- Eyre, J., Miller, S., Clowry, G., Conway, E., & Watts, C. (2000). Functional corticospinal projections are established prenatally in the human foetus permitting involvement in the development of spinal motor centres. *Brain*, 123(1), 51-64
- Eyre, J., Miller, S., & Ramesh, V. (1991). Constancy of central conduction delays during development in man: investigation of motor and somatosensory pathways. *The Journal of Physiology*, 434(1), 441-452
- Fell, J., & Axmacher, N. (2011). The role of phase synchronization in memory processes. *Nature Reviews Neuroscience*, 12(2), 105-118
- Fillmore, P. T., Phillips-Meek, M. C., & Richards, J. E. (2015). Age-specific MRI brain and head templates for healthy adults from 20 through 89 years of age. *Frontiers in Aging Neuroscience*, 7, 44

- Fillmore, P. T., Richards, J. E., Phillips-Meek, M. C., Cryer, A., & Stevens, M. (2015). Stereotaxic magnetic resonance imaging brain atlases for infants from 3 to 12 months. *Developmental Neuroscience*, 37(6), 515-532
- Florin, E., & Baillet, S. (2015). The brain's resting-state activity is shaped by synchronized cross-frequency coupling of neural oscillations. *Neuroimage*, 111, 26-35
- Floyer-Lea, A., & Matthews, P. M. (2005). Distinguishable brain activation networks for short-and long-term motor skill learning. *Journal of Neurophysiology*, 94(1), 512-518
- Forssberg, H. (1985). Ontogeny of human locomotor control I. Infant stepping, supported locomotion and transition to independent locomotion. *Experimental Brain Research*, 57(3), 480-493
- Forssberg, H. (1999). Neural control of human motor development. *Current Opinion in Neurobiology*, 9(6), 676-682
- Forssberg, H., Grillner, S., & Halbertsma, J. (1980). The locomotion of the low spinal cat I. Coordination within a hindlimb. *Acta Physiologica Scandinavica*, 108(3), 269-281
- Freusberg, A. (1874). Reflexbewegungen beim hunde. *Archiv für die gesamte Physiologie des Menschen und der Tiere*, 9(1), 358-391
- Freyer, F., Aquino, K., Robinson, P. A., Ritter, P., & Breakspear, M. (2009). Bistability and non-Gaussian fluctuations in spontaneous cortical activity. *Journal of Neuroscience*, 29(26), 8512-8524
- Fries, P. (2005). A mechanism for cognitive dynamics: neuronal communication through neuronal coherence. *Trends in Cognitive Sciences*, 9(10), 474-480
- Friston, K. J., Holmes, A. P., Worsley, K. J., Poline, J. P., Frith, C. D., & Frackowiak, R. S. (1994). Statistical parametric maps in functional imaging: a general linear approach. *Human Brain Mapping*, 2(4), 189-210
- Giszter, S. F. (2015). Motor primitives—new data and future questions. *Current Opinion in Neurobiology*, 33, 156-165
- Giszter, S. F., Mussa-Ivaldi, F. A., & Bizzi, E. (1993). Convergent force fields organized in the frog's spinal cord. *Journal of Neuroscience*, 13(2), 467-491
- Goltz, F. L. (1869). Beiträge zur Lehre von den Functionen der Nervencentren des Frosches. A. Hirschwald.
- Graziano, M. (2006). The organization of behavioral repertoire in motor cortex. *Annual Review of Neuroscience*, 29, 105-134
- Grillner, S. (1974). On the generation of locomotion in the spinal dogfish. *Experimental Brain Research*, 20(5), 459-470
- Grillner, S. (1985). Neurobiological bases of rhythmic motor acts in vertebrates. *Science*, 228(4696), 143-149
- Grillner, S. (2006). Biological pattern generation: the cellular and computational logic of networks in motion. *Neuron*, 52(5), 751-766
- Grillner, S. (2011). Control of locomotion in bipeds, tetrapods, and fish. *Comprehensive Physiology*, 1179-1236
- Grillner, S., & El Manira, A. (2020). Current principles of motor control, with special reference to vertebrate locomotion. *Physiological Reviews*, 100(1), 271-320
- Grillner, S., & Zangger, P. (1979). On the central generation of locomotion in the low spinal cat. *Experimental Brain Research*, 34(2), 241-261
- Gross, J., Kujala, J., Hämäläinen, M., Timmermann, L., Schnitzler, A., & Salmelin, R. (2001). Dynamic imaging of coherent sources: studying neural interactions in the human brain. *Proceedings of the National Academy of Sciences*, 98(2), 694-699



- Guertin, P. A. (2009). The mammalian central pattern generator for locomotion. *Brain Research Reviews*, 62(1), 45-56
- Hart, C. B., & Giszter, S. F. (2010). A neural basis for motor primitives in the spinal cord. *Journal of Neuroscience*, 30(4), 1322-1336
- Hayasaka, S., & Nichols, T. E. (2004). Combining voxel intensity and cluster extent with permutation test framework. *Neuroimage*, 23(1), 54-63
- Hermens, H. J., Freriks, B., Disselhorst-Klug, C., & Rau, G. (2000). Development of recommendations for SEMG sensors and sensor placement procedures. *Journal of Electromyography and Kinesiology*, 10(5), 361-374
- Hodgkin, A. L. (1951). The ionic basis of electrical activity in nerve and muscle. *Biological Reviews*, 26(4), 339-409
- Houweling, S., Daffertshofer, A., van Dijk, B. W., & Beek, P. J. (2008). Neural changes induced by learning a challenging perceptual-motor task. *Neuroimage*, 41(4), 1395-1407
- Hug, F., Avrillon, S., Sarcher, A., Del Vecchio, A., & Farina, D. (2021). Networks of common inputs to motor neurons of the lower limb reveal neural synergies that only partly overlap with muscle innervation. *bioRxiv*
- Huttenlocher, P. R. (1979). Synaptic density in human frontal cortex-developmental changes and effects of aging. *Brain Research*, 163(2), 195-205
- Hyafil, A. (2015). Misidentifications of specific forms of cross-frequency coupling: three warnings. *Frontiers in Neuroscience*, 9, 370
- Ibanez, J., Del Vecchio, A., Rothwell, J., Baker, S., & Farina, D. (2021). Only the Fastest Corticospinal Fibers Contribute to β Corticomuscular Coherence. *Journal of Neuroscience*, 41(22), 4867-4879
- Ivanenko, Y. P., Dominici, N., Cappellini, G., Di Paolo, A., Giannini, C., Poppele, R. E., & Lacquaniti, F. (2013). Changes in the spinal segmental motor output for stepping during development from infant to adult. *Journal of Neuroscience*, 33(7), 3025-3036
- Ivanenko, Y. P., Poppele, R. E., & Lacquaniti, F. (2004). Five basic muscle activation patterns account for muscle activity during human locomotion. *The Journal of Physiology*, 556(1), 267-282
- Ivanenko, Y. P., Poppele, R. E., & Lacquaniti, F. (2006). Spinal cord maps of spatiotemporal alpha-motoneuron activation in humans walking at different speeds. *Journal of Neurophysiology*, 95(2), 602-618
- Jankowska, E., Jukes, M., Lund, S., & Lundberg, A. (1967a). The Effect of DOPA on the Spinal Cord 5. Reciprocal organization of pathways transmitting excitatory action to alpha motoneurons of flexors and extensors. *Acta Physiologica Scandinavica*, 70(3-4), 369-388
- Jankowska, E., Jukes, M., Lund, S., & Lundberg, A. (1967b). The Effect of DOPA on the Spinal Cord 6. Half-centre organization of interneurons transmitting effects from the flexor reflex afferents. *Acta Physiologica Scandinavica*, 70(3-4), 389-402
- Jensen, O., & Colgin, L. L. (2007). Cross-frequency coupling between neuronal oscillations. *Trends in Cognitive Sciences*, 11(7), 267-269
- Kerkman, J. N., Daffertshofer, A., Gollo, L. L., Breakspear, M., & Boonstra, T. W. (2018). Network structure of the human musculoskeletal system shapes neural interactions on multiple time scales. *Science Advances*, 4(6), eaat0497
- Kerkman, J. N., Zandvoort, C. S., Daffertshofer, A., & Dominici, N. (2022). Body weight control is a key element of motor control for toddlers' walking. *Frontiers in Network Physiology*, 11

- Kiehn, O. (2006). Locomotor circuits in the mammalian spinal cord. *Annual Review of Neuroscience*, 29, 279-306
- Kilner, J. M., Baker, S. N., Salenius, S., Hari, R., & Lemon, R. N. (2000). Human cortical muscle coherence is directly related to specific motor parameters. *Journal of Neuroscience*, 20(23), 8838-8845
- Kinney, H. C., Brody, B. A., Kloban, A. S., & Gilles, F. H. (1988). Sequence of central nervous system myelination in human infancy: II. Patterns of myelination in autopsied infants. *Journal of Neuropathology & Experimental Neurology*, 47(3), 217-234
- Kovach, C. K., Oya, H., & Kawasaki, H. (2018). The bispectrum and its relationship to phase-amplitude coupling. *Neuroimage*, 173, 518-539
- Kristeva, R., Patino, L., & Omlor, W. (2007). Beta-range cortical motor spectral power and corticomuscular coherence as a mechanism for effective corticospinal interaction during steady-state motor output. *Neuroimage*, 36(3), 785-792
- Kutch, J. J., & Valero-Cuevas, F. J. (2012). Challenges and new approaches to proving the existence of muscle synergies of neural origin. *PLoS Computational Biology*, 8(5), e1002434
- Lacquaniti, F., Ivanenko, Y. P., & Zago, M. (2012). Development of human locomotion. *Current Opinion in Neurobiology*, 22(5), 822-828
- Larsen, L. H., Jensen, T., Christensen, M. S., Lundbye-Jensen, J., Langberg, H., & Nielsen, J. B. (2016). Changes in corticospinal drive to spinal motoneurons following tablet-based practice of manual dexterity. *Physiological Reports*, 4(2), e12684
- Lawrence, D. G., & Kuypers, H. G. (1968a). The functional organization of the motor system in the monkey: I. The effects of bilateral pyramidal lesions. *Brain*, 91(1), 1-14
- Lawrence, D. G., & Kuypers, H. G. (1968b). The functional organization of the motor system in the monkey: II. The effects of lesions of the descending brain-stem pathways. *Brain*, 91(1), 15-36
- Lee, D. D., & Seung, H. S. (1999). Learning the parts of objects by non-negative matrix factorization. *Nature*, 401(6755), 788-791
- Lee, D. D., & Seung, H. S. (2001). Algorithms for non-negative matrix factorization. *Advances in Neural Information Processing Systems*,
- Lemay, M. A., & Grill, W. M. (2004). Modularity of motor output evoked by intraspinal microstimulation in cats. *Journal of Neurophysiology*, 91(1), 502-514
- Lemon, R. N. (2008). Descending pathways in motor control. *Annual Review of Neuroscience*, 31, 195-218
- Lesinski, M., Hortobagyi, T., Muehlbauer, T., Gollhofer, A., & Granacher, U. (2015). Dose-response relationships of balance training in healthy young adults: a systematic review and meta-analysis. *Sports Medicine*, 45(4), 557-576
- Maris, E., & Oostenveld, R. (2007). Nonparametric statistical testing of EEG-and MEG-data. *Journal of Neuroscience Methods*, 164(1), 177-190
- Martínez-Cancino, R., Heng, J., Delorme, A., Kreutz-Delgado, K., Sotero, R. C., & Makeig, S. (2019). Measuring transient phase-amplitude coupling using local mutual information. *Neuroimage*, 185, 361-378
- McCrea, D. A., & Rybak, I. A. (2008). Organization of mammalian locomotor rhythm and pattern generation. *Brain Research Reviews*, 57(1), 134-146
- Mehrkanoon, S., Breakspear, M., & Boonstra, T. W. (2014). The reorganization of corticomuscular coherence during a transition between sensorimotor states. *Neuroimage*, 100, 692-702



- Mellor, S., Tierney, T. M., O'Neill, G. C., Alexander, N., Seymour, R. A., Holmes, N., López, J. D., Hill, R. M., Boto, E., Rea, M., Roberts, G., Leggett, J., Bowtell, R., Brookes, M. J., Maguire, E. A., Walker, M. C., & Barnes, G. R. (2021). Magnetic field mapping and correction for moving OP-MEG. *IEEE Transactions on Biomedical Engineering*, 69(2), 528-536.
- Mendez-Balbuena, I., Huethe, F., Schulte-Mönting, J., Leonhart, R., Manjarrez, E., & Kristeva, R. (2011). Corticomuscular coherence reflects interindividual differences in the state of the corticomuscular network during low-level static and dynamic forces. *Cerebral Cortex*, bhr147
- Mima, T., & Hallett, M. (1999a). Corticomuscular coherence: a review. *Journal of Clinical Neurophysiology*, 16(6), 501
- Mima, T., & Hallett, M. (1999b). Electroencephalographic analysis of cortico-muscular coherence: reference effect, volume conduction and generator mechanism. *Clinical Neurophysiology*, 110(11), 1892-1899
- Murta, T., Chaudhary, U. J., Tierney, T. M., Dias, A., Leite, M., Carmichael, D. W., Figueiredo, P., & Lemieux, L. (2017). Phase-amplitude coupling and the BOLD signal: a simultaneous intracranial EEG (icEEG)-fMRI study in humans performing a finger-tapping task. *Neuroimage*, 146, 438-451
- Mussa-Ivaldi, F. A., Giszter, S. F., & Bizzi, E. (1994). Linear combinations of primitives in vertebrate motor control. *Proceedings of the National Academy of Sciences*, 91(16), 7534-7538
- Nazarpour, K., Barnard, A., & Jackson, A. (2012). Flexible cortical control of task-specific muscle synergies. *Journal of Neuroscience*, 32(36), 12349-12360
- Nichols, T. E., & Holmes, A. P. (2002). Nonparametric permutation tests for functional neuroimaging: a primer with examples. *Human Brain Mapping*, 15(1), 1-25
- Nielsen, J. B. (2003). How we walk: central control of muscle activity during human walking. *The Neuroscientist*, 9(3), 195-204
- Nolte, G., Ziehe, A., Nikulin, V. V., Schlögl, A., Krämer, N., Brismar, T., & Müller, K.-R. (2008). Robustly estimating the flow direction of information in complex physical systems. *Physical Review Letters*, 100(23), 234101
- O'Reilly, C., Larson, E., Richards, J. E., & Elsabbagh, M. (2021). Structural templates for imaging EEG cortical sources in infants. *Neuroimage*, 227, 117682
- Ocaña, F. M., Suryanarayana, S. M., Saitoh, K., Kardamakis, A. A., Capantini, L., Robertson, B., & Grillner, S. (2015). The lamprey pallium provides a blueprint of the mammalian motor projections from cortex. *Current Biology*, 25(4), 413-423
- Omlor, W., Patino, L., Hepp-Reymond, M.-C., & Kristeva, R. (2007). Gamma-range corticomuscular coherence during dynamic force output. *Neuroimage*, 34(3), 1191-1198
- Oostenveld, R., Fries, P., Maris, E., & Schoffelen, J. M. (2011). FieldTrip: Open source software for advanced analysis of MEG, EEG, and invasive electrophysiological data. *Computational Intelligence and Neuroscience*, 2011, 156869
- Osipova, D., Hermes, D., & Jensen, O. (2008). Gamma power is phase-locked to posterior alpha activity. *PLoS One*, 3(12), e3990
- Oudega, M., & Perez, M. A. (2012). Corticospinal reorganization after spinal cord injury. *The Journal of Physiology*, 590(16), 3647-3663
- Overduin, S. A., d'Avella, A., Roh, J., Carmena, J. M., & Bizzi, E. (2015). Representation of muscle synergies in the primate brain. *Journal of Neuroscience*, 35(37), 12615-12624

- Overduin, S. A., d'Avella, A., Carmena, J. M., & Bizzi, E. (2012). Microstimulation activates a handful of muscle synergies. *Neuron*, 76(6), 1071-1077
- Patino, L., Omlor, W., Chakarov, V., Hepp-Reymond, M.-C., & Kristeva, R. (2008). Absence of gamma-range corticomuscular coherence during dynamic force in a deafferented patient. *Journal of Neurophysiology*, 99(4), 1906-1916
- Peiper, A. (1963). *Cerebral function in infancy and childhood*. Plenum Publishing Corporation.
- Perez, M. A., Lundbye-Jensen, J., & Nielsen, J. B. (2006). Changes in corticospinal drive to spinal motoneurons following visuo-motor skill learning in humans. *The Journal of Physiology*, 573(3), 843-855
- Petersen, N. T., Butler, J. E., Marchand-Pauvert, V., Fisher, R., Ledebt, A., Pyndt, H. S., Hansen, N. L., & Nielsen, J. B. (2001). Suppression of EMG activity by transcranial magnetic stimulation in human subjects during walking. *The Journal of Physiology*, 537(2), 651-656
- Petersen, T. H., Willerslev-Olsen, M., Conway, B. A., & Nielsen, J. B. (2012). The motor cortex drives the muscles during walking in human subjects. *The Journal of Physiology*, 590(10), 2443-2452
- Pfurtscheller, G., & Da Silva, F. L. (1999). Event-related EEG/MEG synchronization and desynchronization: basic principles. *Clinical Neurophysiology*, 110(11), 1842-1857
- Pinto, C., & Golubitsky, M. (2006). Central pattern generators for bipedal locomotion. *Journal of Mathematical Biology*, 53(3), 474-489
- Pirondini, E., Coscia, M., Minguillon, J., Millán, J. d. R., Van De Ville, D., & Micera, S. (2017). EEG topographies provide subject-specific correlates of motor control. *Scientific Reports*, 7(1), 1-16
- Reyes, A., Laine, C. M., Kutch, J. J., & Valero-Cuevas, F. J. (2017). Beta Band Corticomuscular Drive Reflects Muscle Coordination Strategies. *Frontiers in Computational Neuroscience*, 11
- Richards, J. E., Sanchez, C., Phillips-Meek, M., & Xie, W. (2016). A database of age-appropriate average MRI templates. *Neuroimage*, 124, 1254-1259
- Riddle, C. N., & Baker, S. N. (2005). Manipulation of peripheral neural feedback loops alters human corticomuscular coherence. *The Journal of Physiology*, 566(2), 625-639
- Roeder, L., Boonstra, T. W., Smith, S. S., & Kerr, G. K. (2018). Dynamics of corticospinal motor control during overground and treadmill walking in humans. *Journal of Neurophysiology*, 120(3), 1017-1031
- Roerdink, M., Lamoth, C. J., & Beek, P. J. (2008). Online gait event detection using a large force platform embedded in a treadmill. *Journal of Biomechanics*, 41(12), 2628-2632
- Rosenberg, J., Halliday, D., Breeze, P., & Conway, B. (1998). Identification of patterns of neuronal connectivity—partial spectra, partial coherence, and neuronal interactions. *Journal of Neuroscience Methods*, 83(1), 57-72
- Rossignol, S., Dubuc, R., & Gossard, J.-P. (2006). Dynamic sensorimotor interactions in locomotion. *Physiological Reviews*, 86(1), 89-154
- Rueda-Delgado, L. M., Solesio-Jofre, E., Serrien, D. J., Mantini, D., Daffertshofer, A., & Swinnen, S. P. (2014). Understanding bimanual coordination across small time scales from an electrophysiological perspective. *Neuroscience & Biobehavioral Reviews*, 47, 614-635
- Rybak, I. A., Shevtsova, N. A., Lafreniere-Roula, M., & McCrea, D. A. (2006). Modelling spinal circuitry involved in locomotor pattern generation: insights from deletions during fictive locomotion. *The Journal of Physiology*, 577(2), 617-639



- Saltiel, P., Wyler-Duda, K., D'Avella, A., Tresch, M. C., & Bizzi, E. (2001). Muscle synergies encoded within the spinal cord: evidence from focal intraspinal NMDA iontophoresis in the frog. *Journal of Neurophysiology*, 85(2), 605-619
- Sanchez, C. E., Richards, J. E., & Almli, C. R. (2012). Neurodevelopmental MRI brain templates for children from 2 weeks to 4 years of age. *Developmental Psychobiology*, 54(1), 77-91
- Scheffer-Teixeira, R., & Tort, A. B. (2016). On cross-frequency phase-phase coupling between theta and gamma oscillations in the hippocampus. *eLife*, 5, e20515
- Schieber, M. H. (2002). Training and synchrony in the motor system. *Journal of Neuroscience*, 22(13), 5277-5281
- Schoffelen, J.-M., Oostenveld, R., & Fries, P. (2005). Neuronal coherence as a mechanism of effective corticospinal interaction. *Science*, 308(5718), 111-113
- Scott, S. H. (2003). The role of primary motor cortex in goal-directed movements: insights from neurophysiological studies on non-human primates. *Current Opinion in Neurobiology*, 13(6), 671-677
- Seymour, R. A., Alexander, N., Mellor, S., O'Neill, G. C., Tierney, T. M., Barnes, G. R., & Maguire, E. A. (2021). Using OPMs to measure neural activity in standing, mobile participants. *Neuroimage*, 244, 118604
- Seymour, R. A., Rippon, G., & Kessler, K. (2017). The detection of phase amplitude coupling during sensory processing. *Frontiers in Neuroscience*, 11, 487
- Shahbazi, F., Ewald, A., & Nolte, G. (2014). Univariate normalization of bispectrum using Hölder's inequality. *Journal of Neuroscience Methods*, 233, 177-186
- Shahbazi, F., Bartz, S., Andreou, C., Samek, W., Leicht, G., Mulert, C., Engel, A. K., & Nolte, G. (2018). Localizing bicoherence from EEG and MEG. *Neuroimage*, 174, 352-363
- Sheremet, A., Burke, S. N., & Maurer, A. P. (2016). Movement enhances the nonlinearity of hippocampal theta. *Journal of Neuroscience*, 36(15), 4218-4230
- Sheremet, A., Kennedy, J., Qin, Y., Zhou, Y., Lovett, S. D., Burke, S. N., & Maurer, A. P. (2019). Theta-gamma cascades and running speed. *Journal of Neurophysiology*, 121(2), 444-458
- Sherrington, C. S. (1910). Flexion-reflex of the limb, crossed extension-reflex, and reflex stepping and standing. *The Journal of Physiology*, 40(1-2), 28-121
- Sherrington, C. S. (1952). *The integrative action of the nervous system*. CUP Archive.
- Stein, P. (2005). Neuronal control of turtle hindlimb motor rhythms. *Journal of Comparative Physiology A*, 191(3), 213-229
- Sylos-Labini, F., La Scaleia, V., Cappellini, G., Fabiano, A., Picone, S., Keshishian, E. S., Zhvansky, D. S., Paolillo, P., Solopova, I. A., & d'Avella, A. (2020). Distinct locomotor precursors in newborn babies. *Proceedings of the National Academy of Sciences*, 117(17), 9604-9612
- Takei, T., Confais, J., Tomatsu, S., Oya, T., & Seki, K. (2017). Neural basis for hand muscle synergies in the primate spinal cord. *Proceedings of the National Academy of Sciences*, 114(32), 8643-8648
- Takei, T., & Seki, K. (2010). Spinal interneurons facilitate coactivation of hand muscles during a precision grip task in monkeys. *Journal of Neuroscience*, 30(50), 17041-17050
- Thelen, E., & Cooke, D. W. (1987). Relationship between newborn stepping and later walking: a new interpretation. *Developmental Medicine & Child Neurology*, 29(3), 380-393

- Ting, L. H. (2007). Dimensional reduction in sensorimotor systems: a framework for understanding muscle coordination of posture. *Progress in Brain Research*, 165, 299-321
- Tort, A. B., Komorowski, R., Eichenbaum, H., & Kopell, N. (2010). Measuring phase-amplitude coupling between neuronal oscillations of different frequencies. *Journal of Neurophysiology*, 104(2), 1195-1210
- Tort, A. B., Rotstein, H. G., Dugladze, T., Gloveli, T., & Kopell, N. J. (2007). On the formation of gamma-coherent cell assemblies by oriens lacunosum-moleculare interneurons in the hippocampus. *Proceedings of the National Academy of Sciences*, 104(33), 13490-13495
- Tresch, M. C., & Jarc, A. (2009). The case for and against muscle synergies. *Current Opinion in Neurobiology*, 19(6), 601-607
- Tresch, M. C., Saltiel, P., & Bizzi, E. (1999). The construction of movement by the spinal cord. *Nature Neuroscience*, 2(2), 162-167
- Tzourio-Mazoyer, N., Landeau, B., Papathanassiou, D., Crivello, F., Etard, O., Delcroix, N., Mazoyer, B., & Joliot, M. (2002). Automated anatomical labeling of activations in SPM using a macroscopic anatomical parcellation of the MNI MRI single-subject brain. *Neuroimage*, 15(1), 273-289
- van Dieën, J. H., van Leeuwen, M., & Faber, G. S. (2015). Learning to balance on one leg: motor strategy and sensory weighting. *Journal of Neurophysiology*, 114(5), 2967-2982
- Van Wijk, B. C. M., Beek, P. J., & Daffertshofer, A. (2012a). Differential modulations of ipsilateral and contralateral beta (de) synchronization during unimanual force production. *European Journal of Neuroscience*, 36(1), 2088-2097
- van Wijk, B. C. M., Beek, P. J., & Daffertshofer, A. (2012b). Neural synchrony within the motor system: what have we learned so far? *Frontiers in Human Neuroscience*, 6, 252
- Vorwerk, J., Cho, J.-H., Rampp, S., Hamer, H., Knösche, T. R., & Wolters, C. H. (2014). A guideline for head volume conductor modeling in EEG and MEG. *Neuroimage*, 100, 590-607
- Vorwerk, J., Oostenveld, R., Piastra, M. C., Magyari, L., & Wolters, C. H. (2018). The FieldTrip-SimBio pipeline for EEG forward solutions. *BioMedical Engineering OnLine*, 17(1), 1-17
- Wagner, F. B., Mignardot, J.-B., Le Goff-Mignardot, C. G., Demesmaeker, R., Komi, S., Capogrosso, M., Rowald, A., Seáñez, I., Caban, M., & Pirondini, E. (2018). Targeted neurotechnology restores walking in humans with spinal cord injury. *Nature*, 563(7729), 65-71
- Westner, B. U., Dalal, S. S., Gramfort, A., Litvak, V., Mosher, J. C., Oostenveld, R., & Schoffelen, J.-M. (2022). A unified view on beamformers for M/EEG source reconstruction. *Neuroimage*, 246, 118789
- Wilson, D., & Wyman, R. (1965). Motor output patterns during random and rhythmic stimulation of locust thoracic ganglia. *Biophysical Journal*, 5(2), 121-143
- Witham, C. L., Riddle, C. N., Baker, M. R., & Baker, S. N. (2011). Contributions of descending and ascending pathways to corticomuscular coherence in humans. *The Journal of Physiology*, 589(15), 3789-3800
- Woolrich, M., Hunt, L., Groves, A., & Barnes, G. (2011). MEG beamforming using Bayesian PCA for adaptive data covariance matrix regularization. *Neuroimage*, 57(4), 1466-1479



- Yang, J. F., & Gorassini, M. (2006). Spinal and brain control of human walking: implications for retraining of walking. *The Neuroscientist*, 12(5), 379-389
- Yang, J. F., Lam, T., Pang, M. Y., Lamont, E., Musselman, K., & Seinen, E. (2004). Infant stepping: a window to the behaviour of the human pattern generator for walking. *Canadian Journal of Physiology and Pharmacology*, 82(8-9), 662-674
- Yang, Q., Logan, D., & Giszter, S. F. (2019). Motor primitives are determined in early development and are then robustly conserved into adulthood. *Proceedings of the National Academy of Sciences*, 116(24), 12025-12034
- Yokoyama, H., Kaneko, N., Ogawa, T., Kawashima, N., Watanabe, K., & Nakazawa, K. (2019). Cortical correlates of locomotor muscle synergy activation in humans: An electroencephalographic decoding study. *iScience*, 15, 623-639
- Zandvoort, C. S., Daffertshofer, A., & Dominici, N. (2021). Differential sets of cortical muscle synergy signatures during adult locomotion 2021 10th International IEEE/EMBS Conference on Neural Engineering (NER),
- Zandvoort, C. S., van Dieën, J. H., Dominici, N., & Daffertshofer, A. (2019). The human sensorimotor cortex fosters muscle synergies through cortico-synergy coherence. *Neuroimage*, 199, 30-37



SUMMARY



The central nervous system intrigues us. Despite its complexity it guarantees the control of balance and walking with seemingly little effort. Unravelling how the central nervous system accomplishes this is a challenging task. Over the last two centuries, a large body of literature has established that motor control relies on the recruitment of a low-dimensional organisation in the spinal cord. **Chapter 1** provides a brief overview of how modular functional units at the spinal cord steer groups of muscles. It covers both historical and contemporary views of this spinal modularity and highlights the concept of muscle synergies. Anticipating the experimental assessments compiled in the thesis, this introductory chapter also emphasised the significant role of the motor cortex in establishing motor coordination and provides a glance of the central analysis method, namely cortico-synergy coherence.

Chapter 2 entails an experimental assessment on balance control. It is the first study that combines the analyses of cortico-muscular coherence and muscle synergies. It revealed prominent coherence between the cortex and muscle synergies for motor-related beta-band oscillations (13-30 Hz) and oscillations in the Piper band (~40 Hz). This coherence was visible in the cortical motor network, but most pronounced in the paracentral lobule – a medial part of the sensorimotor cortex.

In **Chapter 3**, the experimental focus shifts to walking. In this study, beta-band cortico-synergy coherence turned out significant for two muscle synergies that are predominantly active during the double support phases. Two muscle synergies with temporal patterns timed to the single support phases did not yield such significant beta-band coherence. The maximal coherences of the double support synergies were spatially resembled at the sensorimotor areas. The two muscle synergy patterns that did interact with the motor cortex resembled those that emerge in toddlers when they start walking independently. By contrast, the two muscle synergy patterns without significant cortico-synergy coherence were very similar to those observed during neonatal stepping. Put differently, there may be strong associations between the motor cortex and the two later-emerging muscle synergies during early walking development.

In the study underlying **Chapter 4** I therefore addressed the functional cortico-synergy organisation during walking by contrasting independently walking toddlers with adults. As expected, this study revealed a clear separation of muscle synergies. In line with

Chapter 3, two muscle synergies were coherent to activity in the motor network and two had no significant representation in the cortex.

Given the bipartite frequency cortico-synergy entrainment, in the beta band and Piper rhythm, in **Chapter 5** I discard conventional coherence as a measure and focused instead on relationships across frequencies. In this methodological study, I approached connectivity by higher-order statistical moments – bicoherence and phase-amplitude coupling – and investigated their pros and cons in simulated and empirical neural data. This first assessment paves the way to employ cross-frequency coupling measures in the study of walking and postural control. Future studies will incorporate this technique to investigate the possible interplay between cortico-synergy coherence in the beta band and in the Piper rhythm, which expectably clarifies how *independent* walking is realised with all its balance demands.

In **Chapter 6**, I reflect on the applications of cortico-synergy coherence to electrophysiological data acquired during motor control tasks. It sketches some experimental and methodological outlooks that may shed even more light on the functional relationship between the motor cortex and muscle synergies than the earlier chapters do. It also includes preliminary findings on a longitudinal study comprising the early walking development of muscle synergy representations in the cortex. In line with the preceding studies, a two-by-two grouping of muscle synergies was found, with the synergies that are coherent with cortical activity being those that emerge around the first independent steps. This is clearly a promising result but to achieve an encompassing view on how independent walking is accomplished, the analysis will need to be extended towards cortico-synergy bicoherence.

Taken together, this thesis revealed that motor-related brain rhythms manifest in the muscle synergies during both postural and locomotor control. It provides support that some of the spinally organised muscle synergies do strongly interact with the sensorimotor cortex. The corresponding spinal circuitries are hence not regulated locally, at least not to all extent.



SAMENVATTING



Het centrale zenuwstelsel intrigeert ons. Ondanks zijn complexiteit garandeert het de controle over balans en lopen met ogenschijnlijk weinig inspanning. Ontrafelen hoe het centrale zenuwstelsel dit doet is een uitdagende taak. In de afgelopen twee eeuwen heeft een grote hoeveelheid wetenschappelijke literatuur vastgesteld dat motorische controle berust op de rekrutering van een laag-dimensionale organisatie in het ruggenmerg. **Hoofdstuk 1** geeft een kort overzicht van hoe laag-dimensionale functionele eenheden in het ruggenmerg spiergroepen aansturen. Het behandelt zowel historische als hedendaagse opvattingen over deze laag-dimensionale organisatie en introduceert het concept van spiersynergieën. Vooruitlopend op de experimentele toetsingen die in dit proefschrift zijn beschreven, benadrukt dit inleidende hoofdstuk ook de belangrijke rol van de motorische cortex bij het ondersteunen van bewegingscoördinatie en biedt het een blik op de analysemethode die centraal staat in dit proefschrift, namelijk cortico-synergie coherentie.

Hoofdstuk 2 beschrijft bevindingen van een experiment over balanscontrole. Dit is de eerste studie die de analysetechnieken van cortico-musculaire coherentie en spiersynergieën combineert. Het onthult een prominente samenhang tussen de cortex en spiersynergieën voor motorische bèta-band oscillaties (13-30 Hz) en oscillaties in de Piper-band (~40 Hz). Deze samenhang is zichtbaar in het corticale motorische netwerk, maar het meest duidelijk in de paracentrale lobule - een mediaal deel van de sensomotorische cortex.

In **Hoofdstuk 3** verschuift de focus naar lopen. Uit deze studie blijkt dat bèta-band cortico-synergie coherentie alleen significant is voor de twee spiersynergieën die voornamelijk actief zijn tijdens de fasen wanneer beide benen in contact zijn met de grond. De andere twee spiersynergieën met activatiepatronen tijdens de eenbenige contacten leverden niet zo'n significante bèta-band coherentie op. De maximale coherenties van de synergieën tijdens de dubbele ondersteuningsfase werden gelokaliseerd in de sensomotorische gebieden van de cortex. Deze twee spiersynergiepatronen lijken op diegene die bij peuters ontstaan wanneer ze zelfstandig gaan lopen. Daarentegen zijn de twee spiersynergiepatronen zonder significante cortico-synergie coherentie erg vergelijkbaar met die tijdens neonatale stappen. Anders gezegd, er lijken sterke associaties te zijn tussen de motorische cortex en de twee spiersynergieën die verschijnen tijdens de vroege loopontwikkeling.

In de studie die ten grondslag ligt aan **Hoofdstuk 4** heb ik daarom de functionele cortico-synergie organisatie tijdens het lopen onderzocht van onafhankelijk lopende peuters en deze vergeleken met die van volwassenen. Zoals verwacht onthult deze studie een duidelijke scheiding van spiersynergieën. In overeenstemming met Hoofdstuk 3 zijn twee spiersynergieën coherent met de activiteit in het motorische netwerk en twee hebben geen significante representatie in de cortex.

Omdat cortico-synergie coherentie alleen fasekoppeling kwantificeert voor eenzelfde frequentie, focus ik in **Hoofdstuk 5** op maten die patronen kunnen identificeren tussen verschillende frequenties. In deze methodologische studie benader ik connectiviteit met statistische momenten van hogere orde - bicoherentie en fase-amplitudekoppeling - en hun voor- en nadelen onderzocht in gesimuleerde en empirische neurale data. Deze eerste beoordeling maakt de weg vrij om koppelingsmaten tussen verschillende frequenties toe te passen in studies naar lopen en balansregulatie. Toekomstige studies kunnen dergelijke technieken gebruiken om de mogelijke wisselwerking tussen cortico-synergie coherentie in de bèta-band en in het Piper-ritme te onderzoeken, wat naar verwachting duidelijk maakt hoe *onafhankelijk* lopen wordt gerealiseerd met alle balansvereisten.

In **Hoofdstuk 6** reflecteer ik op de toepassingen van cortico-synergie coherentie op elektrofysiologische data die zijn verkregen tijdens motorische controletaken. Het schetst enkele experimentele en methodologische visies die nog meer licht kunnen werpen op de functionele relaties tussen de motorische cortex en spiersynergieën dan beschreven in de eerdere hoofdstukken. Zo beschrijft het hoofdstuk voorlopige resultaten van een longitudinaal onderzoek dat de vroege ontwikkeling van spiersynergieën bestudeert in relatie tot de cortex. In overeenstemming met de voorgaande studies is een twee-op-twee groepering van spiersynergieën gevonden, waarbij de synergieën die samenhangen met corticale activiteit degene zijn die ontstaan rond de eerste onafhankelijke stappen. Dit is duidelijk een veelbelovend resultaat, maar om een nog uitgebreider beeld te krijgen van hoe onafhankelijk lopen wordt bereikt, moeten de focus worden verlegd naar cortico-synergie bicoherentie.



Samengevat onthult dit proefschrift dat motorische hersenritmes zich manifesteren in de spiersynergieën tijdens zowel balans- als loopcontrole. Het beschrijft dat sommige van de spinale georganiseerde spiersynergieën sterk interageren met de sensomotorische cortex. De corresponderende spinale circuits worden dus niet volledig lokaal gereguleerd.

ACKNOWLEDGEMENTS



My time at the VU is coming to an end after having been here for a decade. It has been an amazing journey during which I've met many incredible people that have contributed to this thesis in one way or another. On the next couple of pages I would like to attempt to thank them. As many of you know most findings in this thesis rely on analyses in MATLAB: a numerical programming software that I spent quite a lot of time working with throughout my PhD. It therefore feels somewhat appropriate to thank everybody involved in this thesis by assigning them a MATLAB function that captures their contributions best.

I would like to start by thanking the two people who were most involved in the process of realising this doctoral thesis, Nadia Dominici and Andreas Daffertshofer. Nadia, you helped me with my first steps in the academic world as my daily PhD supervisor and the PI of the Learn2Walk-project. We ran most of the longitudinal project on TD-children together and I would therefore like to dedicate the `run` function to you; we were a great team. Thank you very much for your confidence in me and your effort in getting the very best out of the project and me. Andreas, thank you very much for your unwavering confidence in my thesis and for all the opportunities you have given me. I think that your role in realising this thesis can be best described by the `keyboard` function. Meetings with you often gave me a moment to pause before running further, allowing me to reflect on what I had been doing and what the next steps should be. This steering has been invaluable for the project and me, and is one of the reasons why this thesis has turned out the way it has. You were always there for me with some good advice and help at times when I needed it the most.

Jaap van Dieën, you were the one who hired me as a research assistant in the former Neuromechanics section to run my first EEG and EMG-recordings back in 2016. These were the first steps into the field of electrophysiology and was the foundation of my research internship and PhD-project. I therefore decided that the `tic` function best describes your contributions as it marks the start of the “elapsed time” of my PhD journey. Thank you for this opportunity and I am happy that this resulted in Chapter 2 of this thesis.

Guido Nolte, thank you for the opportunity to visit the Universitätsklinikum Hamburg-Eppendorf and the warm welcome to the MEG group in Hamburg. I very much enjoyed the month I spent there. You showed me the advantages of simulating data and I don't think that

I have used `randn` so much ever since. I learnt lots about time series analysis and am very grateful that my stay resulted in a collaboration leading to Chapter 5 of this thesis.

Thank you to the members of my reading committee, Tjeerd Boonstra, Matthew Brookes, Natasha Maurits, Jeroen Smeets, and Vivian Weerdesteyn for your time and effort to read my thesis. The discussions during my defence may remind me of the functions `try` and `catch` because you, the members of my reading committee, will check if everything flows well in my thesis by using the command `try`. If this is not the case, you will continue to `catch` and ask a question about it.

I am happy to be accompanied by two paranimphs, Margit and Niels. Margit, I have got to know you during the Research Master Human Movement Sciences. We have grown into research master and PhD buddies as we always have been at similar stages of our academic life. Thank you for always being there, both during the ups and downs. The progress has been like a raw signal with low and high frequencies, but if you wish to apply a low-pass filter using `filtfilt` you will see a gradual but steady incline. I am very happy to have you by my side during my defence. Niels, the function `ode113` is without a doubt the most appropriate pick. This was our most frequently used function during the minor BWSB as part of the bachelor curriculum when we properly got to know each other. Back then I didn't realise that BWSB was just the steppingstone towards an awesome friendship. I am very grateful for all the nice times we had (and are having) together including our trip to Canada, sporting activities, listening to music, weekends away, dinners, and drinks, and I am very happy to have you on my other side during my defence.

Thanks to the (other) members of the BabyGaitLab for the nice (non-)scientific conversations about everything and nothing. The function `pause` marks the moments of all the nice chats. Annike, setting up the CP-measurements at the VUmc together turned into a finely tuned machine. Thanks for the nice moments during our trips to Edinburgh and Maastricht and the dinners at Pizzabakkers and Spaghetteria after our late measurements. Jennifer, thanks for the collaboration during the TD-measurements, where we sometimes turned into children ourselves. Marzieh and Ruud, a.k.a. EEG buddies, thanks for all the fruitful discussions and the nice moments outside work as part of the PhutsalDoctors. Bert



and Marije, my buddies during our trips to Rome. Thanks a lot for your company during our long days of experiments, pilot testing including melons, craft beer tours, and the extensive midnight conversations whilst waiting for busses that didn't show up.

I have spent most of my PhD in A613 and A621 and therefore would like to thank my former roomies. Sabrina, running buddy from A613. Thanks for the nice runs during work, improvised covid-marathons, Dam tot Damloops, and Batavierenraces. I remember we had the idea to convince as many colleagues as possible to join our runs so probably the function `sum` will help to keep track of this. Dirk, your down-to-earth view always helped to put things in perspective. Outside work, I much enjoyed our mutual love for techno music that we celebrated at many parties. I therefore think that the function `play` applies well to this so that we can listen to it again. Puck, I very much appreciate the nice sporting activities and weekends away with the four of us and hope that many more will follow in the Netherlands, UK, France, and Switzerland. This is not the `end`. Thank you to the other (former) PhDs and postdocs of the Department of Human Movement Sciences. I very much enjoyed the PhD/ECR weekends and other social activities (such as the coffee breaks): Ali, Andrea, Anna, Anne, Anouk, Axel, Bart, Bart, Bastian, Ben, Dan, Daniel, Daniëlle, Daphne, Edwin, Encarna, Erik, Faezeh, Fang, Guido, Guido, Ilse, Jacob, Jeanine, Jens, Jian, Koen, Laure, Lisa, Leila, Lotte, Lotte, Luke, Maaïke, Marit, Mireille, Mohammad, Moira, Mojtaba, Nick, Nicola, Nicolas, Nina, Nini, Pieter, Roel, Stephan, Stephanie, Sauvik, Tammie, Tom, Ton, and Twan.

To the other staff members of the department, Bernadette, Brenda, David, Dinant, Eli, Geert, Henk, Huub, John, Kirsten, Lieke, Maarten, Marjan, Mirjam, Melvyn, Rob, Sjoerd, thank you for the scientific discussions at the coffee machine. Sometimes these conversations were serious, whilst others were about the fact that one could play minesweeper (`xpbombs`) in MATLAB. Also, thanks for the nice moments during the Batavierenraces, social activities, and conference trips.

TO3 and ABC'ers – Franz-Jozef, Hans, Lennaert, Leon, Vincent – I think that I can rightfully assign the `help` function to you. I usually came to you when some of our measurement equipment was broken (again) or I needed something else, and always tried to pretend it was

not a semi-crisis moment. I very much appreciated that I could always knock on your door and received the best help, so thank you very much for that!

Parents and participants, thank you for taking part in our longitudinal study on the development of walking. Our intense study would not have been possible without you. Typically, more stickers, markers, and electrodes appeared every time you arrived for our next measurement, but you gave the study your full support. It has always been nice to see your children growing up and therefore the function `cdf` (cumulative distribution function) applies to this.

Luckily, there has also been a life of family and friends besides MATLAB and I will therefore stop to refer to MATLAB-functions for the personal acknowledgments. They have always provided me a safe place to go back to.

Douwe, tijdens de minor BWSB en de Research Master hebben we elkaar leren kennen en zijn we goede vrienden geworden. Gelukkig hebben we onze vriendschap doorgezet met onze “Bakkie pleuah” groep samen met Niels en zien we elkaar vaak voor koffie. Onze gesprekken tijdens de koffie gaan vaak nergens over en dat maakt het zo mooi.

Mum, Dad, & Bobby, thank you very much for the warm welcome into the Crowe family. I very much look forward to having you ‘around the corner’ when living in the UK.

Lieve oma & oma, helaas heeft het niet zo mogen zijn dat jullie bij m’n verdediging aanwezig zijn, en dat vind ik heel jammer, maar ik weet dat jullie hoe dan ook trots zijn.

Lieve Baba, Mama, & Maarten, bedankt voor al jullie steun. Jullie warme nest is altijd iets dat me ontzettend geholpen heeft en dat waardeer ik enorm. Het heeft absoluut bijgedragen aan de totstandkoming van dit proefschrift.

Emily, thank you for being my biggest supporter! You have contributed so much to this thesis and really helped me by always being there. I am really happy we will be taking our next step together and move to England. We have already gone on so many adventures and I very much look forward to all the beautiful things ahead of us.



Coen, July 2022

LIST OF PUBLICATIONS

Zandvoort C.S., Van Dieën J.H., Dominici N., Daffertshofer A. (2019). *The human sensorimotor cortex fosters muscle synergies by manifesting through cortico-synergy coherence*. Neuroimage. **199C**: 30-37.

Zandvoort C.S., Daffertshofer A., Dominici N. (2021). *Differential sets of cortical muscle synergy signatures during adult locomotion*. 10th International IEEE Engineering in Medicine and Biology Society Conference on Neural Engineering (NER), EMBS NER 2021 – Proceedings (pp. 1070-1073). [9441206] Institute of Electrical and Electronics Engineers, Inc.

Zandvoort C.S., Nolte G. (2021). *Defining the filter parameters for phase-amplitude coupling from a bi-spectral point of view*. Journal of Neuroscience Methods. **350**: 109032.

Zandvoort C.S., Daffertshofer A., Dominici N. (in press). *Cortical contributions to locomotor primitives in toddlers and adults*. iScience.

Not part of this thesis

Bekius A., Zandvoort C.S., Kerkman J.N., Van der Pol L.A., Vermeulen R.J., Harlaar J., Daffertshofer A., Buizer A.I., Dominici A. (2021). *Neuromuscular control before and after independent walking onset in children with early brain lesions*. Sensors, **21**(8): 2714.

De Bartolo D., Zandvoort C.S., Goudriaan, M., Kerkman, J.N., Iosa, M., Dominici, N. (2022). *The role of walking experience in the emergence of gait harmony in typically developing toddlers*. Brain Sciences, **12**(2): 155.

Kerkman J.N., Zandvoort C.S., Daffertshofer A., Dominici N. (2022). *Body weight control is a key element of motor control for toddlers' walking*. Frontiers in Network Physiology, **2**: 844607.



